Supersonic Film Cooling in Generic Rocket Nozzles

Supersonische Filmkühlung in generischen Raketendüsen

Von der Fakultät für Maschinenwesen der Rheinisch-Westfälischen Technischen Hochschule Aachen zur Erlangung des akademischen Grades einer Doktorin der Ingenieurwissenschaften genehmigte Dissertation

vorgelegt von

Sandra Christine Ludescher geb. Haase

Berichter: Univ.-Prof. Dr.-Ing. Herbert Olivier

Hon.-Prof. Dr.-Ing. Ali Gülhan

Tag der mündlichen Prüfung: 26.06.2020

Diese Dissertation ist auf den Internetseiten der Universitätsbibliothek online verfügbar.

Preamble

The presented work was conducted during my time at the Shock Wave Laboratory (SWL) of the RWTH Aachen University and was settled within the third funding period of the Collaborative Research Center-SFB TRR 40, which was financed by the Deutsche Forschungsgesellschaft (DFG).

First of all, I would like to thank my supervisor and head of the SWL Prof. Dr.-Ing. Herbert Olivier for his support and scientific input to this project.

I would also like to thank Prof. Dr.-Ing. Ali Gülhan, who was willing to be the 2nd reviewer of this dissertation and Prof. Dr.-Ing. Dieter Moormann for charing the examination board.

Furthermore, my thanks go to all colleagues at the Shock Wave Laboratory, especially the workshop team formed by Markus Eichler, Aron Heibges, Hans Peter Michel and Yilmaz Seker. A trouble-free operation of the test facility wouldn't have been possible without them.

I would also like to thank my students Felix Wrede, Felix Rottmann, Nourossalam Ziay-Nikpour and Mustafa Cavdir for their input and support in the numerical part of this work.

Additionally, I would like to thank my dear colleagues within the SFB TRR 40 for fruitful discussions and exciting cooperations, as well as for the pleasant atmosphere during the annual graduate seminars.

Last but not least I would like to thank my husband Thomas, my parents and friends for their continuous support during the last sometimes stressful years.

Sandra Ludescher Aachen, 26.06.2020

Abstract

Rocket engines have to withstand high thermal loads. For guaranteeing a safe operation of the engine, these loads on the structure have to be minimized by applying cooling. However, the mass and costs of the cooling system are critical design parameters, since they affect the total cost-value ratio of the engine. In addition, reusability of the engine and the cooling system becomes more and more important. A possible cooling technique with low additional mass and high reusability is film cooling. It is based on a coolant film, which flows parallel to the wall and builds a protective layer between hot gas and structure. This technique is already applied in some rocket engines for the thermally less stressed components. By combining film cooling with other cooling methods, it is also used in regions of higher thermal loads. However, until now this technique bears a lot of uncertainties regarding its efficiency, which limits its application in the engine.

The aim of this work is to reduce these uncertainties by providing a better understanding of the film cooling behavior under rocket-engine-like conditions. Therefore, supersonic, tangential film cooling in the expansion part of a conical nozzle is investigated and the most important influencing parameters on film cooling behavior are detected and explained. Supported by numerical simulations the similarity of the experimental hot gas conditions and the hot gas conditions in a real rocket engine is shown.

For a theoretical investigation of the gained data the cooling efficiencies of each experiment are determined. Therefore, a model for calculating the heat transfer coefficients of the local hot gas-coolant mixture is developed. Additionally, the influence of several characteristic numbers on the cooling efficiency is investigated and correlation models for the experimental data are found. Based on this, a simple model for a rough design of a supersonic film cooling application in a nozzle is proposed and used for giving a first approximation of the coolant gas mass fluxes in a realistic engine.

Furthermore, film cooling experiments in a dual-bell nozzle are conducted. The parameter of interest here is the influence of the contour inflection geometry on film cooling efficiency in the bell extension when the nozzle operates in altitude mode. These results can help in future design processes for this type of nozzles.

Kurzzusammenfassung

Raketentriebwerke müssen hohen thermischen Belastungen standhalten. Um einen sicheren Betrieb des Motors zu gewährleisten, müssen diese Belastungen des Aufbaus durch Kühlung minimiert werden. Die Masse und die Kosten des Kühlsystems sind jedoch kritische Konstruktionsparameter, da sie das Gesamtkosten-Nutzen-Verhältnis des Motors beeinflussen. Auch die Wiederverwendbarkeit des Motors und des Kühlsystems wird immer wichtiger. Eine mögliche Kühltechnik mit geringer Zusatzmasse und hoher Wiederverwendbarkeit ist die Filmkühlung. Sie basiert auf einem Kühlfilm, der parallel zur Wand fließt und dort eine Schutzschicht zwischen Heißgas und Struktur aufbaut Diese Technik wird bereits bei einigen Raketentriebwerken für die thermisch weniger beanspruchten Bauteile angewandt. In Kombination mit anderen Kühlmethoden wird es auch in Regionen mit hoher thermischer Belastung eingesetzt. Diese Technik birgt jedoch bis jetzt viele Unsicherheiten in Bezug auf ihren Wirkungsgrad, was ihre Anwendung im Motor einschränkt.

Ziel dieser Arbeit ist es, diese Unsicherheiten durch ein besseres Verständnis des Filmkühlverhaltens unter raketentriebwerksähnlichen Bedingungen zu verringern. Daher wird die supersonische, tangentiale Filmkühlung im Expansionsteil einer konischen Düse untersucht und die wichtigsten Einflussgrößen auf das Filmkühlverhalten ermittelt und erklärt. Unterstützt durch numerische Simulationen wird die Ähnlichkeit der experimentellen Heißgasbedingungen mit denjenigen in einem realen Raketentriebwerk gezeigt. Für eine theoretische Untersuchung der gewonnenen Daten werden die Kühleffizienzen jedes Experiments bestimmt. Dafür wird ein Modell zur Berechnung der Wärmeübergangskoeffizienten des lokalen Heißgas-Kühlgas-Gemisches entwickelt. Zusätzlich wird der Einfluss verschiedener Kennzahlen auf die Kühleffizienz untersucht und Korrelationen für die experimentell gewonnenen Daten entwickelt. Auf dieser Grundlage wird ein einfaches Modell für eine grobe Auslegung einer supersonischen Filmkühlungsanwendung in einer Düse vorgeschlagen und verwendet, um eine erste Näherung für die Massenströme des Kühlgases in einem realen Triebwerk zu erhalten. Ferner werden Filmkühlexperimente in einer Dual-Bell Düse durchgeführt. Der hier interessierende Parameter ist der Einfluss der Konturknickgeometrie auf die Filmkühlungseffizienz in der Düsenerweiterung, wenn die Düse im Höhenmodus arbeitet. Diese Ergebnisse können bei zukünftigen Konstruktionsprozessen dieser Düsenart hilfreich sein.

Table of Contents

1 Introduction 1
2 State of the Art 4
3 Theoretical Background 8
3.1 Nozzle Flow 8
3.1.1 Chemical State 8
3.1.2 Boundary Layer 10
3.1.3 Heat Transfer 15
3.2 Supersonic Film Cooling 19
3.2.1 General Model 19
3.2.2 Compressible, Turbulent Shear Layer 20
3.2.3 Boundary Layer Region 21
3.2.4 Enhanced Goldstein Model for Axisymmetric Flow 24
3.2.5 Film Cooling Efficiency 26
3.2.6 Model for the Heat Transfer Coefficient of the Gas Mixture 27
3.3 Dual-Bell Nozzle 32
3.3.1 General Working Principle 32
3.3.2 Transition 33
3.3.3 Film Cooling in Dual-Bell Nozzles 35
4 Experimental Setup 37
4.1 Test Facility 37
4.2 Conical Nozzle 39
4.2.1 Coolant Supply 41
4.3 Measurement Technique 43
4.3.1 Static Pressure 43
4.3.2 Heat Flux 44
4.3.3 Detonation Velocity 45
4.3.4 Signal Recording 46
4.4 Stagnation Conditions 47
4.4.1 Experimental Conditions 47

4.4.2 Reproducibility 48
5 Influence and Prevention of Condensation in the Nozzle 50
5.1 Detection of Condensation 50
5.2 Theoretical Influence of Condensation 52
5.3 Heating System 55
5.4 Experiments with Heating System 56
5.4.1 Heating the Attached Nozzle 56
5.4.2 Heating the Detonation Tube and Nozzle Stagnation Chamber 59
5.4.3 Heater Settings for Different Hot Gas Conditions 60
6 Reference Flow 62
6.1 Testing Time 62
6.2 Boundary Layer 66
6.3 Numerical Approach 68
6.3.1 Dummy Gas 75
7 Film Cooling in the Conical Nozzle 77
7.1 General Flow Conditions 77
7.2 Coolant Conditions 80
7.3 Parametric Study 82
7.3.1 Blowing Ratio 82
7.3.2 Slot Height 84
7.3.3 Hot Gas Condition 85
7.3.4 Coolant Gas 86
7.4 Evaluation of Influencing Parameters 89
7.4.1 Characteristic Numbers of Film Cooling 92
7.5 Numerical Investigations 96
7.5.1 Hot Gas-Coolant Flow Field at Injection Position 96
7.5.2 Influence of Heat Transfer Coefficient on Cooling Efficiency 98
7.6 Correlation 101
7.7 Estimation of Coolant Mass Flux in a Real Rocket Engine 105
8 Film Cooling in a Dual-Bell Nozzle 109
8.1 Motivation 109

8.2 General Design 110
8.2.1 Contour Inflection Geometry 113
8.3 Numerical Flow Investigations 115
8.3.1 Nozzle Flow 115
8.4 Experimental Studies 117
8.4.1 Instrumentation 117
8.4.2 Reference Flow 119
8.4.3 Film Cooling 120
8.4.4 Evaluation of the Influence of the Contour Inflection Geometry 121
9 Conclusion 128
10 References 131
Appendix 142
A. NIST Data for Thermocouples Type E 142
B. Dummy Gas for Condition 2 and 3 143
C. Dual-Bell Nozzle 145
D. Publications and Student Theses Created in the Scope of this Work 147

List of Figures

Fig. 1.1 Ariane 5 ES-ATV carrying ATV-001 (Jules Verne). Photo: ESA- S. Corvaja 2008 [1] 1
Fig. 3.1 Scheme of a velocity boundary layer profile 11
Fig. 3.2 Influence of pressure gradient on boundary layer profile for the same u_∞ of the freestream 12
Fig. 3.3 Influence of Mach number on the velocity profile of a laminar boundary layer flow over an insulated flat plate [49] 12
Fig. 3.4 Comparison of different boundary layer models (left) and Mach and unit Reynolds number of the same flow (right) over running length 14
Fig. 3.5 Temperature boundary layer profile for different wall temperatures (flow direction left to right) 16
Fig. 3.6 Schematic flow field at the injection point for overexpanded coolant flow, adapted from Bowersox and Schetz [62] 19
Fig. 3.7 Mixing of hot gas and coolant gas flow [16] 20
Fig. 3.8 Shear layer of hot gas (upper flow) and coolant (lower flow) under the assumption of equal static pressures [64] 21
Fig. 3.9 Scheme of hot gas and coolant mixing in the boundary layer region with a control volume for the energy balance [7] 22
Fig. 3.10 Development of the artificial boundary layer in the nozzle starting at the injection point 25
Fig. 3.11 Mixing model of hot gas and coolant with control volume (red dashed line) 28
Fig. 3.12 Dual-Bell nozzle in sea-level mode adapted from [83] 32
Fig. 3.13 Dual-Bell nozzle in altitude mode adapted from [83] 33
Fig. 3.14 Static pressure distribution along the nozzle wall with a sharp-edge contour inflection and inviscid expansion 34
Fig. 4.1 Test facility 37
Fig. 4.2 Schema of the test facility 37
Fig. 4.3 Ideal wave diagram as calculated with KASIMIR 38
Fig. 4.4 Conical nozzle 39
Fig. 4.5 Section view of the conical nozzle (for Detail A see Fig. 4.9) 40
Fig. 4.6 Reference insert 40
Fig. 4.7 Sensor ports 41
Fig. 4.8 Coolant insert s1 41
Fig. 4.9 Detail A 42
Fig. 4.10 Simplified scheme of the coolant supply line 42
Fig. 4.11 Plate in front of the Kulite sensor used for measuring the stagnation pressure. 44
Fig. 4.12 Signal of the two thermocouples used for measuring the detonation velocity ... 46
Fig. 4.13 Comparison of stagnation pressure calculated with KASIMIR to measured stagnation pressure for Condition 1 48
Fig. 5.1 Wall heat flux $\dot{q}$ and static pressure p over time measured about 120 mm downstream of the nozzle throat 50
Fig. 5.2 Washed out paint at the nozzle wall 51
Fig. 5.3 Vapor-pressure curve of water [106] 52
Fig. 5.4 Simplified temperature profile and energy balance for condensation of superheated steam on a cold surface 53

Fig. 5.5 Nozzle, stagnation chamber and tube with installed heating wires 55
Fig. 5.6 Thermocouple for the control of the outer wall temperature (left) and rock wool isolation (right) 56
Fig. 5.7 Comparison of heat fluxes near the throat (x= 123 mm)) and far downstream (x= 235 mm), (Condition 1) 56
Fig. 5.8 Time averaged heat fluxes along nozzle wall for different wall temperatures, (Condition 1) 59
Fig. 5.9 Static pressure distribution for the heated and unheated nozzle (Condition 2) 59
Fig. 6.1 Stagnation pressures over time for all three conditions 62
Fig. 6.2 Static pressure over time at different A/A* for condition 1 63
Fig. 6.3 Wall heat fluxes over time for condition 1, pressure in the vacuum tank lower than in Fig. 6.2 63
Fig. 6.4 Time averaged static pressures over distance from nozzle throat for all three conditions 64
Fig. 6.5 Time averaged wall heat fluxes over distance from nozzle throat for all three conditions, for defect thermocouple T2 for condition 2 and 3 the heat flux value was approximated by a polynomial derived from the measured values 65
Fig. 6.6 Reproducibility of wall heat fluxes for condition 1 65
Fig. 6.7 Calculated displacement thickness from experimental data and theoretical displacement thickness as given by Eq. (6.2) plotted along the wall 66
Fig. 6.8 Gradient of the radial velocity in the conical nozzle, condition 1, (ANSYS Fluent) 69
Fig. 6.9 Ratio of static to stagnation pressure over distance from nozzle throat for laminar flow simulation and experiment (condition 1) 69
Fig. 6.10 Wall heat fluxes over distance from nozzle throat for laminar flow simulation and experiment (condition 1) 70
Fig. 6.11 Ratio of static to stagnation pressure over distance from nozzle throat for turbulent flow simulation and experiment (condition 1) 70
Fig. 6.12 Wall heat fluxes over distance from nozzle throat for turbulent flow simulation and experiment (condition 1) 71
Fig. 6.13 Mass fractions of different species simulated for turbulent, non- equilibrium flow over nozzle center line, zero represents nozzle throat, condition 1 71
Fig. 6.14 Comparison of experimental and simulated static pressures over distance from nozzle throat (along the wall) for all three conditions (turbulent, non-equilibrium flow) 72
Fig. 6.15 Comparison of experimental and simulated wall heat fluxes over distance from nozzle throat (along the wall) for all three conditions (turbulent, non-equilibrium flow) 72
Fig. 6.16 Mach number over distance from nozzle throat (along the wall) exemplary for condition 1 73
Fig. 6.17 Reynolds number of all three conditions. Running length along the nozzle wall starting in the nozzle throat 73
Fig. 6.18 Pressure gradient over axial distance from nozzle throat for conditions 1 and 374
Fig. 6.19 Comparison of the simulated boundary layer thicknesses for condition 1 and 3, distance measured along the nozzle wall 75
Fig. 7.1 Wall heat fluxes over distance from injection position for argon injection, condition 1 78
Fig. 7.2 Static pressure for the reference flow and with injection of two different coolant mass fluxes, condition 1 79

Fig. 7.3 Coolant pressure in distributor ring, red dashed-line marks the start of the hot gas flow in the nozzle 80
Fig. 7.4 Velocity (left) and Mach number (right) profile over slot width (s1) gained from simulations and quasi-1d, isentropic calculations 81
Fig. 7.5 Wall heat flux with and without helium injection ($p_{0,c}$=0.52-2.8 bar) and different blowing ratios (condition 1, s1) 83
Fig. 7.6 Wall heat flux with and without helium injection for different slot heights (condition 1), Ma_c(s= 0.41 mm)= 1.57 and Ma_c(s= 0.56 mm)= 1.73) 84
Fig. 7.7 Cooling efficiency of helium with the same coolant mass flux and injection in different hot gas conditions (s2) 85
Fig. 7.8 Cooling efficiency of helium with the same blowing ratio and injection in different hot gas conditions (s2) 86
Fig. 7.9 Wall heat flux for injection of different coolant gases in comparison to the wall heat flux without injection (condition 1, Ma_c= 1.57- 1.63 and s2) 87
Fig. 7.10 Total cooling efficiency of different experiments with helium injection over convective Mach number for different hot gas conditions and injection slots 93
Fig. 7.11 Total cooling efficiency over blowing ratio for injection of different coolant gases through different slots in different hot gas conditions 94
Fig. 7.12 Total cooling efficiency over momentum flux ratio for injection of different coolant gases through different slots in different hot gas conditions 95
Fig. 7.13 Comparison of simulated and measured wall heat fluxes with and without helium injection, condition 1, s1 96
Fig. 7.14 Pressure and streamline distributions of hot gas and coolant (helium, p_0= 1.5 bar) at the injection position from ANSYS Fluent simulations, condition 1, s1 97
Fig. 7.15 Cooling efficiency for helium injection in hot gas C1, s1 98
Fig. 7.16 Simplified cooling efficiency for injection of different coolants in hot gas C1, s1 99
Fig. 7.17 Cooling efficiency taking into account the heat transfer coefficients for injection of different coolants in hot gas condition 1, s1 99
Fig. 7.18 Ratio of heat transfer coefficients (see Eq. (3.53)) for different coolant gases 100
Fig. 7.19 Correlation of the experimental data using the simplified calculation of the film cooling efficiency (Eq. (3.52) with $\alpha_{nc}/\alpha_c = 1$) and the correlation factor by Goldstein (Eq. (3.35)) enhanced by the ratio of the heat capacities 101
Fig. 7.20 Correlation of the experimental data using Eq. (3.52) for the film cooling efficiency together with the model for the heat transfer coefficients (see Eq. (3.53)) and the correlation factor by Goldstein (Eq. (3.35)) enhanced by the ratio of the heat capacities 102
Fig. 7.21 Correlation of the experimental data using Eq. (3.52) for the film cooling efficiency together with the model for the heat transfer coefficients (see Eq. (3.53)) and the correlation factor for axisymmetric flow (Eq. (3.48)) enhanced by the ratio of the heat capacities 102
Fig. 7.22 Correlation of the experimental data using Eq. (3.52) for the film cooling efficiency together with the model for the heat transfer coefficients (see Eq. (3.53)) and a simple correlation factor. The dashed box marks the range of cooling efficiencies, which are of technical relevance 103
Fig. 7.23 Correlation of the experimental data as in Fig. 7.21 with a curve fit for all data. The dashed box marks the range of cooling efficiencies, which are of technical relevance 104

Fig. 7.24 Adiabatic wall temperatures for different injection mass fluxes of hydrogen, the red dashed line represents the critical wall temperature of 1400 K 106
Fig. 7.25 Adiabatic wall temperatures for different injection mass fluxes of methane, the red dashed line represents the critical wall temperature of 1400 K 107
Fig. 8.1 Scheme of boundary layer separation and reattachment at a sharp-edged contour inflection 110
Fig. 8.2 Geometry of the dual-bell nozzle 111
Fig. 8.3 Design of the dual-bell nozzle and section view of the nozzle 112
Fig. 8.4 Section view of the different inflection geometries. Sharp-edge upper, rounded lower adapter 114
Fig. 8.5 Gradient of the radial velocity in the dual-bell nozzle with sharp-edged contour inflection, condition 1 (ANSYS Fluent) 116
Fig. 8.6 Mach number along the nozzle axis and wall pressure, the red dashed line marks the inflection point, the grey dotted line the position of the injection slot 116
Fig. 8.7 Instrumented dual-bell nozzle with installed heating system at the test facility .. 117
Fig. 8.8 Section view of base nozzle and coolant insert (left) and installed thermocouples (TC) in the base nozzle (right) 118
Fig. 8.9 Static pressures in the sharp-edge dual-bell nozzle without coolant injection, p_0= 30 bar, red dashed line represents inflection point 119
Fig. 8.10 Heat fluxes in the sharp-edge dual-bell nozzle without coolant injection, p_0= 30 bar, red dashed line represents inflection point 119
Fig. 8.11 Wall heat fluxes in the sharp-edge dual-bell nozzle with and without helium injection, s= 0.46 mm, p_0= 30 bar, red dashed line represents inflection point 120
Fig. 8.12 Enlargement of the wall heat flux distribution downstream of the contour inflection, red dashed line represents inflection point 121
Fig. 8.13 Comparison of static pressures in the sharp-edge and rounded adapter nozzle for reference condition, the red dashed lines represent start and end of the contour inflection 122
Fig. 8.14 Comparison of wall heat fluxes in the sharp-edge and rounded adapter nozzle for reference condition, the red dashed lines represent start and end of the contour inflection 123
Fig. 8.15 Wall heat fluxes in the rounded adapter dual-bell nozzle with and without helium injection, s= 0.46 mm, p_0= 30 bar, the red dashed lines represent start and end of the contour inflection 124
Fig. 8.16 Wall heat fluxes for the rounded adapter dual-bell nozzle downstream the contour inflection with and without helium injection, s= 0.46 mm, p_0= 30 bar, the red dashed lines represent start and end of the contour inflection 124
Fig. 8.17 Simplified cooling efficiencies for the sharp-edge and rounded dual-bell nozzle with helium as coolant and blowing ratio F= 1.37, the red dashed lines represent start and end of the contour inflection 125
Fig. 8.18 Simplified cooling efficiencies for the sharp-edge and rounded dual-bell nozzle with helium as coolant and blowing ratio F= 1.03, the red dashed lines represent start and end of the contour inflection 125
Fig. 8.19 Simplified cooling efficiencies for the sharp-edge and rounded dual-bell nozzle with helium as coolant and blowing ratio F= 0.72 (rounded) and F= 0.73 (sharp-edge), the red dashed lines represent start and end of the contour inflection 126

List of Tables

Table 2.1 Film cooling data of Vulcain 2 [8,9,2] 4
Table 3.1 Mechanism of hydrogen-oxygen reaction [44], elementary reactions chosen from [45], the component M represents here a reaction with a third body. 9
Table 3.2 μ_0, T_0 and S for different coolant gases [73] 29
Table 3.3 Parameter for calculating the thermal conductivity [73] 31
Table 4.1 Geometrical data of the conical nozzle ([94] and CAD data) 40
Table 4.2 Geometrical data of the coolant slots (from [94] and CAD data) 42
Table 4.3 Experimental conditions (initial pressures and mixture ratios chosen from [92]) 47
Table 4.4 Deviations in the filling pressure of H_2 for Condition 1 49
Table 5.1 Ratio of heat transfer coefficients for liquid water and condensing steam to that of superheated steam (which behaves like a gas [111]) [112] 54
Table 5.2 Heat fluxes and temperature differences at the x= 123 mm position in the nozzle extension 57
Table 5.3 Nozzle wall temperatures needed for condensation free experiments 61
Table 6.1 Comparison of unit Reynolds numbers in the nozzle throat for all conditions of the conical nozzle and data from CALO nozzle tests and Vulcain 2 [115] 67
Table 6.2 Components considered for the dummy gas of condition 1 and mass weighted molar mass of the dummy gas 76
Table 6.3 Coefficients for Eq. (6.3) for the condition 1 dummy gas. Data is valid for a temperature range of 200 K to 6000 K (c_p) and 300 K to 5000 K (μ and λ) 76
Table 7.1 Comparison of film cooling parameters in the conical nozzle for conditions 1-3 and those of a typical full-scale system [122] 77
Table 7.2 Injection conditions of the coolants for all slot heights 81
Table 7.3 Gas properties at the injection position in the coolant gas core flow for condition 1 and slot s2, coolant gas properties from [127], coolant velocity, density, temperature and hot gas data from simulation. Coolant stagnation pressures (top-down) 2.67 bar, 2.2 bar, 1.67 bar, 1.6 bar, coolant stagnation temperature for all gases T_0= 330 K 87
Table 7.4 Influence of different parameters on film cooling efficiency when each parameter increases 89
Table 7.5 Engine data of the SFB TRR 40 TCD2 [135] 105
Table 7.6 Coolant conditions for the investigated setup [127,135] 105
Table 7.7 Hot gas and nozzle conditions the correlation is based on 108
Table 7.8 Coolant conditions the correlation is based on 108
Table 8.1 Parameter of the final dual-bell nozzle based on the design of Dr. Chloé Génin 111
Table 8.2 Positions of the sensors closest to the contour inflection (CI) and injection slot (IS), distance measured along the wall 118

Nomenclature

Latin letters

A	area
C*	Chapman-Rubesin factor
c_f	friction coefficient
c_p	heat capacity
D	diameter
Da	Damköhler number
F	blowing ratio
h	enthalpy
I	momentum flux ratio
K	acceleration parameter
$\dot{m}$	mass flux
M	molar mass
Ma	Mach number
NPR	nozzle pressure ratio
Nu	Nusselt number
p	static pressure
Pr	Prandtl number
$\dot{q}$	heat flux
r	radius
R	universal gas constant
Re	Reynolds number
ROF	ratio oxidizer to fuel
s	slot height
S	Sutherland constant
St	Stanton number
T	temperature
t	time
u	velocity in x-direction
v	velocity in y-direction
x	continuous variable in streamwise
y	continuous variable perpendicular to streamwise direction

Greek letters

α	heat transfer coefficient
γ	isentropic exponent
δ	boundary layer thickness
η	cooling efficiency
θ	displacement thickness
λ	thermal conductivity
μ	viscosity
ξ	correlation parameter
ρ	density

Subscripts

a	ambient
aw	adiabatic wall
b	base nozzle
c	coolant
conv.	convective
e	nozzle extension
hg	hot gas
initial	state before detonation
l	liquid
m	mixture hot gas-coolant
nc	without coolant injection
r	recovery
w	wall
0	stagnation condition
∞	free stream

1 Introduction

For bringing satellites, space probes or manned missions in orbit or even out of the solar system, they have to be accelerated to very high speed. Space transport systems need therefore powerful launcher rockets able to carry tons of payload. Due to global demand and competition, the efficiency regarding the cost-value ratio of these launchers is subject to continuous improvements. The most important component to look at when increasing the launcher's performance is the rocket engine.



Fig. 1.1 Ariane 5 ES-ATV carrying ATV-001 (Jules Verne). Photo: ESA- S. Corvaja 2008 [1]

Nowadays, the most efficient main stage rocket engines are based on liquid propulsion systems with cryogenic propellants. Therefore, most current launcher rockets use this type of engine. These engines have to endure huge heat fluxes of up to $80\ MW/m^2$ and more in the nozzle throat [2]. The heat loads result from the high stagnation pressures of about 100 bar and the high stagnation temperatures of the flow of a several thousand Kelvin. Since future rocket engines should provide even more thrust and will therefore fly with even higher stagnation pressures the correlation $\dot{q} \sim p_0^{0,8}$ easily shows that the heat loads will increase even more. By now, there is

no material, which is able to withstand such thermal loads. Therefore, cooling methods are needed to protect the structure and ensure a safe operation of the engine.

Several cooling techniques exist and are separated in active and passive techniques. A passive cooling technique is for example ablative cooling, where an ablative material is placed at the nozzle walls and isolates it from the heat. In contact with the hot gas flow the material pyrolyzes. The resulting heat dissipation due to the phase change of the material and the developing gas protect the wall from the incoming heat flux [3]. Since this process is not reversible, this cooling technique is not reusable. A reusable and active cooling technique is regenerative cooling. It is used in most liquid main stage engines. The cryogenic fuel, for example hydrogen, is used as coolant and flows through cooling channels in the nozzle wall. After cooling the wall, the fuel is then injected into the combustion chamber. This technique can handle huge heat loads and is almost without losses in the engine's thrust. However, this technique requires a complex combustion chamber and nozzle design and due to the high thermal and pressure gradient in the wall failures like the doghouse effect can occur. A much simpler active cooling technique is film cooling. It is often used in combustion chambers and nozzle extensions, but also for cooling blades of gas turbines [4,5]. The gaseous or liquid coolant is injected through holes or slots close to the nozzle wall and builds an insulating and heat absorbing film [6]. This film flows then parallel to the hot gas flow in the nozzle. Accordingly the cooling effect is not restricted to the place of injection, but spreads also to a downstream region [7]. Film cooling is reusable and allows a much simpler manufacturing process than regenerative cooling. However, the total cooling performance reached is less than for regenerative cooling. Therefore, film cooling is often used for cooling the nozzle extension, where the heat loads are less than in the throat area or in combination with regenerative cooling in the areas of higher heat fluxes.

In the current work, the focus is set on the exclusive use of gaseous, supersonic film cooling in the nozzle extension. By performing experimental and theoretical studies in a conical nozzle, the influencing parameters on film cooling behavior are investigated. The hot gas conditions used are similar to the conditions in a real engine. Additionally, studies with a dual-bell nozzle are performed focusing on the influence of the contour inflection geometry on film cooling efficiency in the bell extension.

This work has been performed within the collaborative research center SFB TRR 40 “Technological foundations for the design of thermally and mechanically highly loaded components of future space transportation systems” founded by the German Research Foundation DFG, which is gratefully acknowledged.

2 State of the Art

Film cooling in the nozzle extension is often used in engines with a gas generator cycle, since here the turbine exhaust gas (TEG) can be used as coolant. This is for example done in the F1 engine of the Saturn 5 rocket, the J-2X engine of the SLS (Space Launch System) or the Vulcain 2 engine of the Ariane 5 launcher. For the latter the film cooling application in the nozzle extension will now be further discussed. However, the working principle is very similar in every engine.

Vulcain 2 has a thrust optimized parabolic (TOP) nozzle made of different high-temperature resistant metal alloys. Nevertheless, to keep the nozzle structure stable a wall temperature of approximately 1400 K may not be exceeded. Due to the very high stagnation conditions of the hot gas, (see Table 2.1) this can only be realized with cooling.

Table 2.1 Film cooling data of Vulcain 2 [8,9,2]

stagnation temperature hot gas	3600 K
stagnation pressure hot gas	115 bar
oxidizer and fuel	LOX and LH_2
ROF	6.1
temperature TEG	~ 800 K
expansion ratio at injection	~ 32
TEG, $\dot{m}_{TEG}/\dot{m}_{\infty}$	~ 3.1 %
hydrogen cooling gas, $\dot{m}_{H_2}/\dot{m}_{\infty}$	~1 %

Therefore, in the nozzle extension a small amount of hydrogen and the TEG is injected at almost the same position through a circumferential slot of a few millimeters height with supersonic speed. Thus, a sufficient cooling of the nozzle wall is reached over a certain length. Since the coolant gas is injected far downstream of the throat it is not participating in the combustion process and only partly participating in the main flow expansion. This causes the major disadvantages of film cooling, which are losses in specific impulse and thrust of the engine [3]. Because of that, most current developments of highly efficient rocket engines neglect film cooling. However, due to its reusability, simple design and good compatibility with the gas generator cycle, film cooling is still a promising technique. For a more efficient and with that a more economical design of film cooling in the

future the coolant mass flux has to be minimized without reducing the cooling efficiency. To do that, a better understanding of the overall film cooling behavior is needed.
Once injected the effect of the coolant film starts to decrease with increasing distance from the injection slot. This decrease depends on various parameters, which have to be detected and understood. Until now, many experimental and numerical film cooling studies have been conducted [10,11,7]. Between 1950 and 1970 a lot of film cooling correlations for subsonic film cooling on a flat plate were developed [12–16]. They showed the influence of the coolant mass flux, distance from the injection point, injection slot height and boundary layer thickness of the hot gas on film cooling efficiency. Also the influence of the injection angle was often discussed and a tangential injection of the coolant film was found to be the most efficient method [17,18]. Additionally, the cooling efficiency rises when the coolant is injected at supersonic speed [19,4]. Not only the way of coolant injection, but also the type of hot gas flow the coolant is injected to has an influence on the stability of the coolant film, since several studies showed that film cooling is less efficient in a turbulent flow than in a laminar one [20–23].
For film cooling in the expansion part of a nozzle, as subject in the current work, the main characteristics of the hot gas flow are high Mach numbers, compressibility and a favorable pressure gradient.

An increasing hot gas Mach number and with that increasing compressibility of the flow was found to have a positive influence on film cooling efficiency [24,25]. Dellimore et al. [26] developed a model to qualify the compressible effects of the flow more deeply by using the convective Mach number [27] and the temperature ratio of coolant stream and main stream. He found that the cooling efficiency increases with increasing convective Mach number and decreasing temperature ratio.

In addition, various studies investigated the influence of a main stream favorable pressure gradient on the film cooling efficiency. However, the results on this are very inconsistent. Hay et al. [28] found in their experimental studies that film cooling under the influence of a strong favorable pressure gradient yields a decrease in the heat transfer coefficient compared to injection in a zero pressure gradient flow. This was particularly seen for low blowing ratios. As reason a reduction of turbulence in the boundary layer caused by the acceleration of the flow was found. Several

other experimental studies showed a similar effect [29–31]. Numerically these results were confirmed by studies by Konopka et al. [32].

In contrast to that Zakkay et al. [33] found in their experiments just the opposite and recommend an adverse pressure gradient for increasing film cooling efficiency. The negative influence of a favorable main stream pressure gradient was also found by several other authors [34,20] and is explained with an increased shear layer spreading which comes with an increase in the coolant hot gas mixing.
For evaluating these contradictions Dellimore et al. [35] developed a film cooling model with consideration of the stream wise pressure gradients based on a jet model by Simon [21] and found that the effect of a pressure gradient depends on the velocity ratio of main stream and coolant flow. Following this model, a favorable pressure gradient increases film cooling efficiency if the velocity of the coolant is higher than the velocity of the hot gas. If the coolant velocity is lower than that of the hot gas this pressure gradient leads to a reduction of the efficiency.

As last option for the film cooling behavior under the influence of a pressure gradient Keller and Kloker [36] found in their numerical studies in a planar nozzle with different half-opening angles no proof for an influence of an altering favorable pressure gradient on film cooling.

Finally, it should be mentioned that with a change in the pressure gradient a lot of other main flow parameters like boundary layer height, Reynolds number etc. change too, which makes a final evaluation of this very difficult. This assertion is also valid for most of the other influencing parameters. Therefore, an investigation of the influence of one single parameter is nearly impossible and film cooling behavior should be studied in the setup of the individual application.
Film cooling in the extension part of a nozzle was already investigated by some authors [8,37–39]. To the best of this author's knowledge the most realistic investigations of a film cooling application in the extension part of a rocket nozzle were conducted by Suslov et al. [40]. They used a Vulcain-2-like subscale model to test film cooling at different hot gas conditions and coolant mass fluxes and showed that film cooling is an efficient cooling technique in the nozzle extension.

However, this literature review shows that a lot of influencing parameters on film cooling exist and most of them are not yet fully understood. Future work

will be to identify the most relevant parameters and finding reliable correlations for film cooling behavior in rocket nozzles.

3 Theoretical Background

3.1 Nozzle Flow

The flow of a rocket nozzle is axisymmetric and characterized by high stagnation temperatures and pressures, as well as a strong acceleration of the flow due to a favorable pressure gradient. In the following, the focus is set on the supersonic flow in the nozzle expansion part. Here, the boundary layer is normally in a turbulent state [41,42]. Also, the strong acceleration of the flow in this part of the nozzle can lead to a freezing of the dissociated hot gas molecules, such that the local gas properties and gas temperatures differ from the ones of the equilibrium state [43].

3.1.1 Chemical State

The chemical state of the hot gas flow can be described by the Damköhler number Da.

$$Da = \frac{t_f}{t_r}, \tag{3.1}$$

where t_f is the flow time scale of the hot gas and t_r the reaction time scale. For $Da \gg 1$ the flow is in an equilibrium state, for $Da \approx 1$ the flow is in a chemical non-equilibrium state and for $Da \ll 1$ the flow is in a chemical frozen state. Due to the strong expansion of the hot gas in the nozzle expansion part, non-equilibrium and frozen state are typical for rocket engine flows [44].

For calculating the chemical non-equilibrium, the chemical reactions of hydrogen and oxygen have to be considered. In general, chemical reactions can be described by the following equation [44].

$$\sum_{i=1}^{N} v'_{i,j} B_i \leftrightarrow \sum_{i=1}^{N} v''_{i,j} B_i\,, \qquad j = 1, \dots, N \tag{3.2}$$

N is the number of components taking part in the reaction. $v'_{i,j}$ and $v''_{i,j}$ represent the stoichiometric coefficients of the component B_i. The reaction velocity of a component *i* $\dot{w}_{i,j}$ can be calculated by [44]

$$\dot{w}_{i,j} = k_f \prod_{i=1}^{N} \left(\frac{\rho X_i}{M_i}\right)^{v'_{i,j}} - k_b \prod_{i=1}^{N} \left(\frac{\rho X_i}{M_i}\right)^{v''_{i,j}}. \tag{3.3}$$

Here, X_i represents the mass fraction of component *i* and M_i its molar mass. The reaction rate *k* for the forward reaction (*f*) and reverse reaction (*b*) can be calculated using the Arrhenius equation.

$$k = A_r \cdot T^{\beta_r} \cdot e^{\frac{-E_r}{RT}}, \tag{3.4}$$

with A_r as a constant pre-exponential factor for each reaction, β_r providing the temperature dependency of A_r and E_r the activation energy. By this, the reaction rate of every elementary reaction can be determined. For a gaseous hydrogen-oxygen reaction 37 elementary reactions are possible [45]. However, for calculations usually a simplified reaction mechanism with only 14 elementary reactions is used (see Table 3.1), since the reactions containing H_2O_2 and HO_2 can be neglected [46].

Table 3.1 Mechanism of hydrogen-oxygen reaction [45], elementary reactions chosen from [46], the component M represents here a reaction with a third body.

Elementary reaction	A_r	β_r	E_r [kJ/mol]
$H + H + M \rightarrow H_2 + M$	1.8×10^{18}	-1.00	0.00
$H_2 + M \rightarrow H + H + M$	6.99×10^{18}	-1.00	436.08
$H + OH + M \rightarrow H_2O + M$	2.20×10^{22}	-2.00	0.00
$H_2O + M \rightarrow H + OH + M$	3.80×10^{23}	-2.00	499.41
$O + O + M \rightarrow O_2 + M$	2.90×10^{17}	-1.00	0.00
$O_2 + M \rightarrow O + O + M$	6.81×10^{18}	-1.00	496.41
$O_2 + H \rightarrow O + OH$	2.00×10^{14}	0.00	70.30
$O + OH \rightarrow O_2 + H$	1.46×10^{13}	0.00	2.08
$H_2 + O \rightarrow H + OH$	5.06×10^{4}	2.67	26.30
$H + OH \rightarrow H_2 + O$	2.24×10^{4}	2.67	18.40
$H_2 + OH \rightarrow H_2O + H$	1.00×10^{8}	1.60	13.80
$H_2O + H \rightarrow H_2 + OH$	4.45×10^{8}	1.60	77.13
$OH + OH \rightarrow H_2O + O$	1.50×10^{9}	1.14	0.42
$H_2O + O \rightarrow OH + OH$	1.51×10^{10}	1.14	71.64

From this the net species production rate of a component can be calculated from [46]

$$w_i = M_i \sum_{j=1}^{N} \left(v''_{i,j} - v'_{i,j}\right) \dot{w}_{i,j}. \tag{3.5}$$

Considering Eqs. (3.3)-(3.5) the dependency of the production rate on temperature and density can clearly be seen. Since both of these flow parameters change rapidly during the acceleration of the flow, chemical reactions are of importance when investigating the nozzle's hot gas flow properties.

3.1.2 Boundary Layer

For a two-dimensional, stationary flow the boundary layer equations can be derived from the Navier-Stokes equations [47] and consist of the equations for conservation of mass (Eq. (3.6)), momentum (Eq. (3.7)) and energy (Eq. (3.8)).

$$\frac{\partial(\rho u)}{\partial x} + \frac{\partial(\rho v)}{\partial y} = 0 \tag{3.6}$$

$$\rho u \frac{\partial u}{\partial x} + \rho v \frac{\partial u}{\partial y} = -\frac{\partial p}{\partial x} + \mu \frac{\partial^2 u}{\partial y^2}$$
$$\frac{\partial p}{\partial y} = 0 \tag{3.7}$$

$$\rho u \frac{\partial h}{\partial x} + \rho v \frac{\partial h}{\partial y} = \lambda \frac{\partial^2 T}{\partial y^2} + u \frac{\partial p}{\partial x} + \mu \left(\frac{\partial u}{\partial y}\right)^2 \tag{3.8}$$

For the special case of a flow with $\rho = const.$ and $\frac{\partial p}{\partial x} = 0$ over a flat plate the thickness of a turbulent boundary layer can be calculated using Eq. (3.9) [48].

$$\delta = 0.376 x Re_{\infty}^{-0.2}, \tag{3.9}$$

with the Reynolds number as given in Eq. (3.10), which represents the ratio of inertial forces to viscous forces

$$Re_\infty = \frac{\rho_\infty u_\infty x}{\mu_\infty}. \tag{3.10}$$

The thickness of the boundary layer represents the distance from the wall at which the flow velocity reaches 99% of the freestream velocity. A scheme of a velocity profile in the boundary layer is shown in Fig. 3.1.

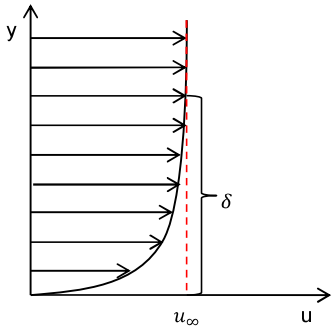


Fig. 3.1 Scheme of a velocity boundary layer profile

For the case of a turbulent boundary layer the velocity profile can be described by a 1/7 power law

$$u(y) = u_\infty \left(\frac{y}{\delta}\right)^{1/7}. \tag{3.11}$$

Eq. (3.11) is not only valid for flat plates, but can also be used for nozzle flows [49].

As mentioned before Eq. (3.9) neglects compressibility and a pressure gradient of the flow. However, these parameters are of importance when it comes to the boundary layer of a supersonic nozzle flow. The influence of these parameters on the boundary layer and the velocity profile is now further discussed. Therefore, Fig. 3.2 displays the velocity profile for a flow with adverse, zero and favorable pressure gradient. It can be seen that the shape of the velocity profile and its gradient at the wall depends strongly on the pressure gradient.

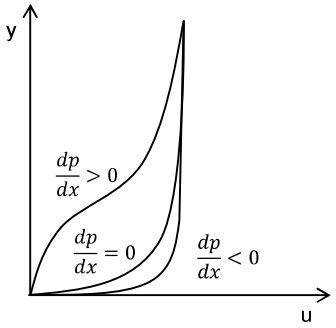


Fig. 3.2 Influence of pressure gradient on boundary layer profile for the same u_∞ of the freestream

For an adverse pressure gradient, the velocity profile gets concave, which can result in a flow separation at the wall, whereas for a favorable pressure gradient the profile gets more bulky so the flow velocity near the wall increases. Additionally to the shape of the velocity profile, also the boundary layer thickness will change when the pressure gradient also affects the local freestream velocity. Following Eqs. (3.9) and (3.10), a higher freestream velocity leads to a decrease in the boundary layer thickness.

The influence of compressibility due to an increase in the Mach number on the boundary layer is shown in Fig. 3.3.

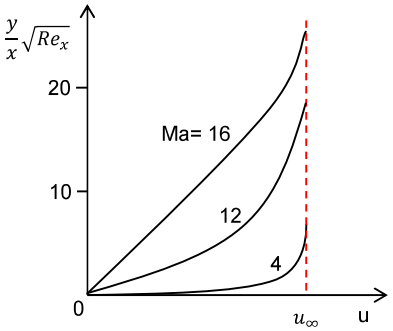


Fig. 3.3 Influence of Mach number on the velocity profile of a laminar boundary layer flow over an insulated flat plate [50]

It can be seen that the boundary layer thickness increases with increasing Mach number [51], since for constant free stream density and temperature

an increase in the Mach number results in more friction and heat production in the boundary layer. This causes changes in the gas temperature, density and viscosity near the wall. Thus, for a compressible boundary layer the conservation equations of momentum and energy are coupled and other than for the incompressible case for a compressible flow also a temperature boundary layer exists (see Sec. 3.1.3).

This discussion shows that the use of Eq. (3.9) for calculating the boundary layer thickness in a nozzle leads unpreventable to deviations from the real thickness. However, the simplicity of this equation makes it attractive to use especially for the film cooling model (see Sec. 3.2). Therefore, a method is needed to include compressibility and pressure gradient effects in Eq. (3.9).

One possible method for calculating a compressible, turbulent boundary layer of a thermally insulated flat plate under the influence of a moderate pressure gradient was suggested by Stratford and Beavers and is shown by Eqs. (3.12)-(3.13) [52].

$$\delta(X) = 0.376 X Re_X^{-0,2}, \tag{3.12}$$

$$X = P(x)^{-1} \int_0^x P(x)dx, \tag{3.13}$$

$$P(x) = \left[\frac{Ma(x)}{1 + \frac{\gamma - 1}{2} Ma(x)^2} \right]^4, \tag{3.14}$$

Eq. (3.14) was formulated by Stollery and El-Ehwany [16]. By replacing the general isentropic exponent with the isentropic exponent of air (γ=1.4) the original formulation of P as given by Stratford and Beavers is achieved. In this model, the flat plate boundary layer thickness is corrected by the introduction of a new running length *X*. This new running length is defined such that the boundary layer of a flow with a constant Mach number, which is equal to the local Mach number, would grow over *X* to the same height as the actual boundary layer would grow over the real length.

Especially for nozzles, many semi-empirical models for calculating the laminar or turbulent boundary layer valid for different ranges of Reynolds numbers and Mach numbers are available. Focusing here on the turbulent

boundary layer of a high Mach numbers nozzle flow the correlation by Edenfield (see Eq. (3.15)) is one possible solution [53]

$$\delta = 0.195 x Ma^{0.375} Re^{-0.166}. \tag{3.15}$$

It is valid for Reynolds numbers in the range of 10^6 to 10^8 and Mach numbers in the range of 7 to 22 [54].

Fig. 3.4 shows a comparison of the different, presented boundary layer models for the hot gas flow in the expansion part of a conical nozzle with 15° half-opening angle. The running length starts with x= 0 at the throat.

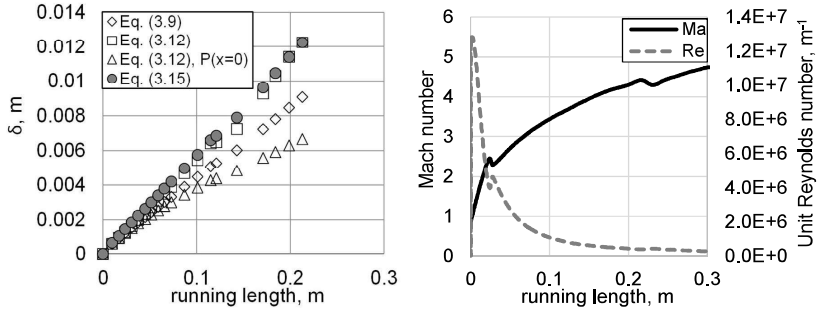


Fig. 3.4 Comparison of different boundary layer models (left) and Mach and unit Reynolds number of the same flow (right) over running length

Due to uncertainties in literature whether P^{-1} in Eq. (3.13) is a local value or determined at the starting point of the boundary layer ($P^{-1}(x = 0)$) both variations of this model are presented in the figure above. Additionally, the Edenfield and flat pate solution for the same flow are given. Comparing these last two models it can be seen that the boundary layer thickness calculated with the Edenfield model is much thicker than the one calculated with the flat plate model. This results i.a. from the compressibility of the flow, which is covered by Eq. (3.15), but neglected by the flat plate model. An increase in the boundary layer height due to compressibility was already shown in Fig. 3.3. This effect seems to overweight the decreasing of the boundary layer height due to the favorable pressure gradient. Comparing now the two possible solutions of Eq. (3.12) with the other models it can be seen, that only the solution with the local value of P^{-1} leads to a boundary layer higher than that of the incompressible flat plate and is in good agreement with Eq. (3.15). Therefore, in this work the local value of P^{-1} is used to solve Eq. (3.13).

It should be mentioned that none of the models given above represents an overall valid solution of the boundary layer in a nozzle, nor takes into account even all influencing parameter on the boundary layer. For example influences like the axisymmetric character of the nozzle flow or the strong temperature gradient between flow and wall have not explicitly been included in the mentioned models given in Eqs. (3.9) and (3.12). In general, it can be said that a well-fitting analysis of boundary layers in rocket nozzles has not yet been developed [43]. More complex calculations of the boundary layer flow need CFD.

3.1.3 Heat Transfer

In a compressible flow not only a velocity layer, but also a temperature layer exists. The height of the temperature layer relative to the velocity boundary layer depends on the Prandtl number. This number represents the ratio of heat production in the flow due to friction to the amount of heat loss by thermal conductivity

$$Pr = \frac{\mu c_p}{\lambda}. \tag{3.16}$$

For $Pr < 1$, the temperature layer is larger and for $Pr > 1$ the temperature layer is smaller than the velocity boundary layer. For $Pr \approx 1$ both layers are of equal height [55]. In case of gaseous flows, the Prandtl number is usually lower than one.

Depending on the wall temperature T_w, the temperature profile at the wall can take different shapes as displayed by Fig. 3.5.

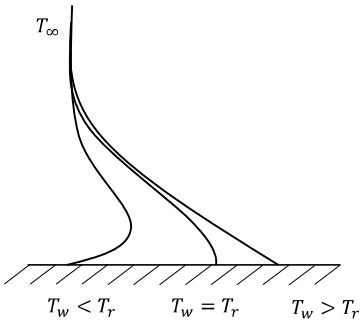


Fig. 3.5 Temperature boundary layer profile for different wall temperatures (flow direction left to right)

Due to viscous dissipation in the compressible boundary layer the temperature reached at the wall for $u = 0$ is not equal to the stagnation temperature of the flow, but can be calculated by

$$T_r = T_\infty \left(1 + \frac{\gamma - 1}{2} r Ma_\infty^2\right), \tag{3.17}$$

$$r = Pr^{1/3}.$$

This temperature is called the recovery temperature T_r and r is the recovery factor, which is here given for a turbulent free boundary layer [3]. As mentioned before gaseous flows mostly have a Prandtl number smaller than one, so following Eq. (3.17) the recovery temperature will always be less than the stagnation temperature of the flow.

The most dominant heat transfer mechanism in a rocket nozzle is forced convection and the heat flux in the wall is given by

$$\dot{q} = \alpha(T_r - T_w). \tag{3.18}$$

It can be seen that the wall heat flux is not only a function of the temperature difference between hot gas and wall, but also of the heat transfer coefficient α. This coefficient depends on the geometry, flow conditions and gas properties of the flow [56]

$$\alpha = St \rho_\infty u_\infty c_p, \tag{3.19}$$

$$St = f(Nu, Re, Pr, Ma),$$

with the Nusselt number *Nu* representing the ratio of convective heat transfer to conductive heat transfer

$$Nu = \frac{\alpha x}{\lambda}. \tag{3.20}$$

For determining the heat transfer coefficient from Eq. (3.19) the local density, velocity, heat capacity and Stanton number *St* of the flow must be known. In the case of a compressible, turbulent flow over a flat plate the Stanton number can be calculated with Eq. (3.21) [57].

$$St = 0.0296 \left(\frac{\rho_\infty u_\infty x}{\mu_\infty}\right)^{-0.2} \left(\frac{T_\infty}{T^*}\right)^{0.6} C^{*0.2} \tag{3.21}$$

C^* is the Chapman-Rubesin factor, which takes into account the changes in density and viscosity due to changes in the temperature. The right hand side of Eq. (3.22) is gained when applying Sutherland's viscosity law and the ideal gas law

$$C^* = \frac{T_\infty \mu^*}{T^* \mu_\infty} = \sqrt{\frac{T^*}{T_\infty}} \left(\frac{T_\infty + S}{T^* + S}\right) = \frac{\rho^* \mu^*}{\rho_\infty \mu_\infty}. \tag{3.22}$$

The constant *S* represents the Sutherland constant, which is for water vapor S= 890 K [58]. All flow properties marked with a star are determined at the reference temperature *T**. It is assumed that this reference temperature is constant over the whole height of the thermal boundary layer at a certain stream wise position. For the calculation of T^* the model by Rasmussen is used [59], which is valid for all gases

$$\begin{aligned} T^* = {} & 0.566 Pr^{1/3} T_\infty + (1 - 0.566 Pr^{1/3}) T_w \\ & + (0.566 Pr^{5/6} - 0.421 Pr) \frac{\gamma - 1}{2} {Ma_\infty}^2 T_\infty. \end{aligned} \tag{3.23}$$

Using Eqs. (3.22) and (3.23) the Stanton number in Eq. (3.21) and with that, the heat transfer coefficient in Eq. (3.19) can be calculated. Comparing Eq. (3.9) and Eq. (3.21) it can also be seen that the Stanton number increases if at a constant position x the boundary layer thickness increases.

For a turbulent nozzle flow, also models for a direct determination of the heat transfer coefficient exist. The most popular model is the Bartz model [60]

$$\alpha = \left[\frac{0.026}{D_*^{0.2}}\left(\frac{\mu^{0.2}C_p}{Pr^{0.6}}\right)_0\left(\frac{\dot{m}}{A_*}\right)^{0.8}\left(\frac{D_*}{r_c}\right)^{0.1}\right]\left(\frac{A_*}{A}\right)^{0.9}\sigma. \tag{3.24}$$

Here, the heat transfer coefficient depends on the nozzle throat geometry (D_* and r_c (radius of curvature at nozzle throat)), the mass flux of the nozzle flow, the gas properties in the stagnation chamber (subscript 0), the local area ratio of the nozzle and σ. This last factor takes into account the variation of the gas properties across the boundary layer

$$\sigma = \frac{1}{\left[0.5\frac{T_w}{T_0}\left(1+\frac{\gamma-1}{2}M^2\right)+0.5\right]^{0.8-(\omega/5)}\left[1+\frac{\gamma-1}{2}M^2\right]^{\omega/5}}$$

$$\mu \sim T^{\omega} \tag{3.25}$$

The exponent ω results from the viscosity-temperature equation and has for air the value 0.6 [61]. For water vapor this exponent can be determined using the high temperature viscosity data by Bonilla [62]

$$\mu = \frac{39.37T^{1.5}}{3315 - T + 0.001158T^2}, [\mu P] \tag{3.26}$$

valid for a temperature range of about $T \approx 650 - 1550\,K$, which results in $\omega \approx 0.95$.

Eq. (3.24) was developed for nozzles with $\frac{D_*}{r_c} \approx 1$ and contraction and expansion half-opening angles of 30° and 15°, respectively. Nevertheless, it is assumed that this equation is also valid for small deviations from these parameters [60].

However, as for the velocity boundary layer also for the heat transfer in a nozzle no analytical model exists and the prediction of heat fluxes in a nozzle is subjected to huge uncertainties [3]. So far the best solutions of the heat transfer problem in nozzles taking into account turbulence and rapidly changing gas properties are provided by numerical approaches like the often used two-dimensional kinetic reference computer program (TDK) [46].

3.2 Supersonic Film Cooling

In this work, only supersonic film cooling with coolant injection tangential to the nozzle wall is discussed. In addition, the Mach number and velocity of the coolant are lower than of the hot gas. The considered experimental conditions should ideally result in equal static pressures, but due to experimental uncertainties, the coolant pressure at injection will be either higher or lower than the local hot gas pressure. The flow field in the vicinity of the injection slot for an overexpanded coolant injection is illustrated in Fig. 3.6.

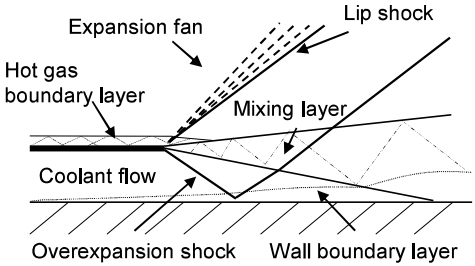


Fig. 3.6 Schematic flow field at the injection point for overexpanded coolant flow, adapted from Bowersox and Schetz [63]

As the hot gas reaches the injection point, an expansion fan forms at the sonic line of the boundary layer at the upper tip of the splitter plate. This leads to a deflection of the hot gas boundary layer towards the wall. On the lower side of the splitter plate, the overexpanded coolant flow adjusts to the local hot gas pressure by an overexpansion shock. Further downstream, this shock is reflected at the wall. Depending on the operation mode of the coolant flow different shocks and expansion waves can occur. For an underexpanded coolant flow an expansion fan followed by a recompression shock appears instead of the overexpansion shock in Fig. 3.6 at the lower side of the splitter plate [32].

3.2.1 General Model

A simplified model describing the mixing process of coolant and hot gas behavior at and downstream the injection point is displayed by Fig. 3.7.

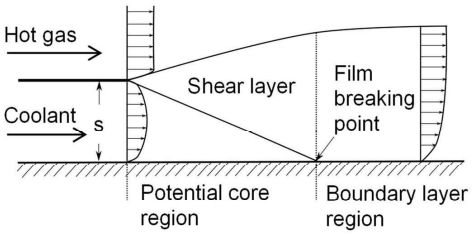


Fig. 3.7 Mixing of hot gas and coolant gas flow [16]

Above and at the wall directly behind the injection point is the potential core region, which consists only of pure coolant. Within this region, the cooling efficiency is at a maximum since the wall is completely protected from the hot gas influence such that consequently the wall temperature is close to the coolant stagnation temperature. Above this region, a shear layer starts to grow at the contact surface of coolant and hot gas. This shear layer spreads while propagating further downstream and reaches the wall after a certain distance from the injection point. With the arrival of the shear layer at the wall, the pure coolant film breaks up and the heat transfer at the wall is influenced by the local mixture of hot gas and coolant. With that, also the cooling efficiency starts to decrease from that point on. The film breaking point also marks the beginning of the boundary layer region, where hot gas and coolant are mixing further with growing distance from the injection point [20]. Thus with increasing distance from the injection point the hot gas flow will once again dominate the heat transfer at the wall resulting in zero cooling efficiency.
Models for the individual regions will now be further discussed.

3.2.2 Compressible, Turbulent Shear Layer

As the hot gas and coolant flows come in contact, the friction and certain instability mechanism at the contact surface initiate the growth of eddy structures. In the case of supersonic film cooling the resulting shear layer is compressible and due to the high Reynolds numbers of $Re > 1 \cdot 10^5$ this shear layer can also be assumed to be turbulent [64]. Starting at the tip of the splitter plate, this layer grows in downstream direction (see Fig. 3.8).

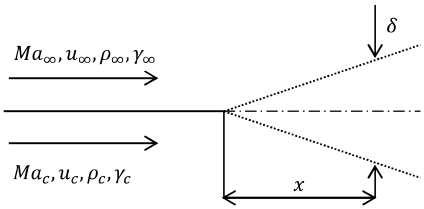


Fig. 3.8 Shear layer of hot gas (upper flow) and coolant (lower flow) under the assumption of equal static pressures [65]

Its thickness at a certain downstream position depends on the growing rate of the shear layer. For the growing rate of a compressible, turbulent shear layer Papamoschou and Roshko [66] found

$$\delta' = \frac{d\delta}{dx} = f\left(\frac{u_c}{u_\infty}, \frac{\rho_c}{\rho_\infty}, \frac{\gamma_c}{\gamma_\infty}, Ma_{conv.}\right). \tag{3.27}$$

The growing rate is a function of the ratios of velocity, density and isentropic exponent of the parallel flows and of the convective Mach number $Ma_{conv.}$. The convective Mach number characterizes the compressibility effects on the shear layer growing and is derived as [27]

$$Ma_{conv.} = \frac{Ma_\infty\left(1 - \frac{u_c}{u_\infty}\right)}{\left(1 + \frac{\rho_c}{\rho_\infty}^{-0.5}\right)\frac{\gamma_c}{\gamma_\infty}^{0.25}}. \tag{3.28}$$

Different studies have shown that with increasing convective Mach number the shear layer growth rate decreases [27,67]. A good overview of experimental studies investigating this correlation is given in [64].

3.2.3 Boundary Layer Region

In the boundary layer region hot gas and coolant are mixing at the wall. The hot gas mass flux, which is mixing up with the coolant is assumed to be equal to the mass flux of a fictitious boundary layer starting at the injection point. A very common boundary layer model for film cooling is the Goldstein model [7]. This model neglects the potential core region and the shear layer development, so mixing of hot gas and coolant starts directly at the injection point as displayed in Fig. 3.9.

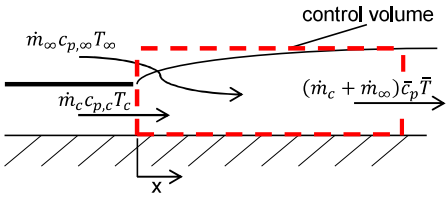


Fig. 3.9 Scheme of hot gas and coolant mixing in the boundary layer region with a control volume for the energy balance [7]

$\bar{T}$ and $\bar{c}_p$ represent the average temperature and mass weighted specific heat in the boundary layer. For a steady flow without any difference in flow velocity over an adiabatic wall an energy balance (see Fig. 3.9) leads to

$$(\dot{m}_c + \dot{m}_\infty)\bar{c}_p \bar{T} = \dot{m}_c c_{p,c} T_c + \dot{m}_\infty c_{p,\infty} T_\infty. \tag{3.29}$$

From this the cooling efficiency is derived as

$$\frac{\bar{T} - T_\infty}{T_c - T_\infty} = \left(1 + \frac{\dot{m}_\infty c_{p,\infty}}{\dot{m}_c c_{p,c}}\right)^{-1} = \eta. \tag{3.30}$$

For calculating the cooling efficiency, the heat capacities and mass fluxes of coolant and hot gas must be known. As mentioned before the mass flux is assumed to be the same as the mass flux in a boundary layer starting at the injection point. Using Eq. (3.11) for the velocity profile the hot gas mass flux for a plane flow per unit width can be calculated with

$$\dot{m}_\infty = \rho_\infty \int_0^\delta u_\infty \left(\frac{y}{\delta}\right)^{1/7} dy = \frac{7}{8}\rho_\infty u_\infty \delta. \tag{3.31}$$

The boundary layer thickness δ follows from Eq. (3.9). The coolant mass flux is defined as

$$\dot{m}_c = \rho_c u_c s, \tag{3.32}$$

with the height of the injection slot *s*. By introducing the correlation factor ξ as defined by Tribus and Klein [12]

$$\xi = \frac{x}{Fs}\left(\frac{\mu_c}{\mu_\infty} Re_c\right)^{-0,25} \tag{3.33}$$

and the dimensionless parameter *F*, which represents the blowing ratio of hot gas and coolant

$$F = \frac{\rho_c u_c}{\rho_\infty u_\infty}, \tag{3.34}$$

the cooling efficiency can be written as [7]

$$\eta = \frac{1}{1 + 0.329 \frac{c_{p,\infty}}{c_{p,c}} \xi^{0.8}}. \tag{3.35}$$

For adapting the boundary layer model to flows with pressure gradient and compressibility Stollery and El-Ehwany [16] suggested the use of the Stratford and Beavers method (see Eqs. (3.12)-(3.14)) in Eq. (3.31). However, in case of a compressible flow without pressure gradient Goldstein et al. [68] also presented an approach for the calculation of the hot gas mass flux, which will now be discussed.

For the compressible case the density is not constant, but changes over the boundary layer height. To consider this a reference density ρ' is defined. The velocity profile is again calculated using Eq. (3.11)

$$\dot{m}_\infty = \int_0^\delta \rho u dy = \rho' \int_0^\delta u dy = \frac{7}{8} \rho' u_\infty \delta. \tag{3.36}$$

It can be seen that there are two unknowns in Eq. (3.36), which are the reference density and the boundary layer height. As next step, it is assumed that this reference density is equal to the reference density of the momentum thickness. Using this and Eq. (3.11) for the velocity profile the momentum thickness can be written as

$$\theta = \frac{\rho'}{\rho_\infty} \int_0^\delta \frac{u}{u_\infty} \left(1 - \frac{u}{u_\infty}\right) dy = \frac{7}{72} \frac{\rho'}{\rho_\infty} \delta. \tag{3.37}$$

For a compressible, non-accelerated boundary layer a solution for the integrated momentum equation is given by [47]

$$\frac{d\theta}{dx} = \frac{\tau_w}{\rho_\infty {u_\infty}^2}. \tag{3.38}$$

According to the reference temperature method (see Eq. (3.23)) this equation can be written as

$$\frac{d\theta}{dx} = \frac{c_f^* \rho^*}{2\rho_\infty}. \tag{3.39}$$

Using the friction relation of an incompressible flat plate [57] and adjusting it for the compressible case by determining the gas properties in the Reynolds number at reference temperature (see Eq. (3.23))

$$c_f^* = 0.0592 Re_*^{-0.2}, \tag{3.40}$$

the momentum thickness can also be written as

$$\theta = 0.037 \frac{\rho^*}{\rho_\infty} Re_*^{-0.2} x. \tag{3.41}$$

By combining Eq. (3.37) and Eq.(3.41) the hot gas mass flux for the compressible case can be calculated with [68]

$$\dot{m}_\infty = 0.333 \rho_\infty u_\infty \left(\frac{\rho^*}{\rho_\infty}\right) Re_*^{-0.2} x. \tag{3.42}$$

The coolant mass flux is unaffected by the compressible boundary layer, so following Eq. (3.30) the cooling efficiency of the compressible case is given by [68]

$$\eta_{compressible} = \frac{1}{1 + 0.333 \frac{c_{p,\infty}}{c_{p,c}} \left[\frac{x}{Fs} \frac{1}{Re_\infty^{0.2}} \left(\frac{\rho_*}{\rho_\infty}\right)^{0.6} C^{*0.2}\right]}. \tag{3.43}$$

For the sake of completeness it should be mentioned that a lot of other boundary layer models and film cooling correlations exist [20,16], but since none of them will be used in this work no further model will be introduced.

3.2.4 Enhanced Goldstein Model for Axisymmetric Flow[1]

The Goldstein model was developed for a flow over a flat plate. In this case, the amount of hot gas mixing with the coolant depends only on the growing of the artificial boundary layer in stream wise direction. However, in an axisymmetric nozzle flow, as in the experiments presented later on, the mixing hot gas mass flux depends also on the local flow diameter of the nozzle. Due to the increasing circumference of the nozzle with increasing downstream distance from the injection point in the divergent nozzle section, the hot gas mass flux in the artificial boundary layer grows faster than for the flat plate case. To take this effect into account the Goldstein model was enhanced for axisymmetric flow. Therefore, Goldstein's

[1] This model is based on an idea of Prof. Olivier and was already published in [69]

fundamental ideas covert by Eqs. (3.29)-(3.30) are reused and the changes are made where it comes to the calculation of the mass fluxes. In Fig. 3.10 the general idea of the artificial boundary layer growing in the conical nozzle is shown. The boundary layer starts to grow at the injection point, where the local nozzle radius is r_c. It builds an annulus, which grows with increasing nozzle radius $r(x)$ and boundary layer thickness $\delta(x)$.

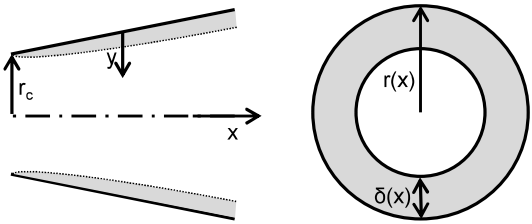


Fig. 3.10 Development of the artificial boundary layer in the nozzle starting at the injection point

Using Eq. (3.11) for the turbulent velocity profile the hot gas mass flux can be written as

$$\begin{aligned}\dot{m}_\infty &= 2\pi\rho_\infty \int_0^\delta u(y)(r-y)dy \\ &= \frac{7}{4}\pi\rho_\infty u_\infty \delta(x)\left(r(x) - \frac{8}{15}\delta(x)\right).\end{aligned} \tag{3.44}$$

For calculating the boundary layer thickness in Eq. (3.44) the method by Stratford and Beavers (see Eqs. (3.12)-(3.14)) is used. The local nozzle radius $r(x)$ for the conical nozzle with a half-opening angle of 15° is

$$r(x) = r_c + tan(15°)\, x. \tag{3.45}$$

The coolant mass flux spreads also over an annulus area and can be calculated with

$$\dot{m}_c = \rho_c u_c \pi((r_c + s)^2 - (r_c)^2) \approx 2\pi\rho_c u_c r_c s. \tag{3.46}$$

The right hand side of Eq. (3.46) shows a simplification for the case that $r_c \gg s$, which is valid for the experimental setup in this work. Combining Eq. (3.30) with Eq. (3.44) and Eq. (3.46) the cooling efficiency for the axisymmetric case follows as

$$\eta = \left[1 + \frac{c_{p,\infty}}{c_{p,c}}\left[\frac{7\delta(X)\big(r(x) - 8/15\,\delta(X)\big)}{4F((r_c+s)^2 - (r_c)^2)}\right]\right]^{-1} \approx \left[1 + \frac{7c_{p,\infty}\delta(X)}{8c_{p,c}Fs}\frac{r(x)}{r_c}\right]^{-1}. \tag{3.47}$$

Generally $8/15\ \delta(X)$ will be much smaller than the local nozzle radius, which leads to the simplification on the right. The only difference between Eq. (3.47) and the flat plate solution in Eq. (3.35) is the introduction of the ratio of the local radius to the radius at the injection point. It can be seen that for the same flow and injection conditions the cooling efficiency is less for an axisymmetric flow than for planar flow.

For correlating the film cooling experiments later on, a correlation factor is defined as

$$\xi = \frac{7\delta(X)r(x)}{8Fsr_c}. \tag{3.48}$$

When calculating this correlation factor the boundary layer thickness and nozzle radius are calculated for the local *x* position, whereas the blowing ratio, as a characteristic number of the individual film cooling setup (see Sec. 7.4.1.2), is calculated at the injection point and is kept constant from this point on.

3.2.5 Film Cooling Efficiency

The cooling efficiency η for a compressible flow is defined as [7]

$$\eta = \frac{T_r - T_{aw,c}}{T_r - T_{0,c}}. \tag{3.49}$$

Where $T_{aw,c}$ is the adiabatic wall temperature in case of coolant injection and $T_{0,c}$ is the stagnation temperature of the coolant. For the experiments presented later on, this equation cannot be used for calculating the cooling efficiency, since the adiabatic wall temperature will not be reached during the short testing time. Therefore, Eq. (3.49) is rewritten using the wall heat fluxes for the case with coolant injection *c* and without coolant injection *nc* [22]. Following Eq. (3.18) the wall heat fluxes can be written as

$$\dot{q}_c = \alpha_c\big(T_{aw,c} - T_w\big), \tag{3.50}$$

and

$$\dot{q}_{nc} = \alpha_{nc}(T_r - T_w). \tag{3.51}$$

Due to the very short testing time the nozzle walls can be assumed to be isothermal, such that the wall temperature T_w is constant. Furthermore, $T_{0,c} = T_w$ is valid for the experiments in this work. Combining this with Eqs. (3.49)-(3.51) yields

$$\eta = 1 - \frac{\alpha_{nc}}{\alpha_c}\frac{\dot{q}_c}{\dot{q}_{nc}} \approx 1 - \frac{\dot{q}_c}{\dot{q}_{nc}}. \tag{3.52}$$

The simplification on the right hand side is often used in literature and is based on the assumption that the influence of coolant injection on the heat transfer coefficient is negligible, at least for low blowing ratios $F < 0.5$ [22]. However, it will be shown later on that even for low blowing ratios this is not valid when it comes to comparing different coolant gases.

3.2.6 Model for the Heat Transfer Coefficient of the Gas Mixture [2]

To avoid problems with the simplified cooling efficiency, the ratio of the heat transfer coefficients must be determined. Since experimentally that is not possible in the current setup, a model for a simple estimation of the local heat transfer coefficients of the hot gas –coolant mixture was developed. Following Eq. (3.19) the ratio of the heat transfer coefficients from Eq. (3.52) can be written as

$$\frac{\alpha_{nc}}{\alpha_c} = \frac{\alpha_\infty}{\alpha_m} = \frac{St_\infty \rho_\infty u_\infty c_{p,\infty}}{St_m \rho_m u_m c_{p,m}}. \tag{3.53}$$

All hot gas properties can be determined from simulations or estimated from simple one-dimensional, isentropic equations. For the Stanton number Eq. (3.21) is used. The subscript m marks the properties of the hot gas - coolant mixture. To determine the properties of the gas mixture the mixing process of hot gas and coolant must be further described. For the following mixing model it is assumed that coolant and main flow are different gases, the splitter thickness is negligible, the mixing of hot gas and coolant starts at the injection point and there are no net pressure forces acting on the control volume of the mixing process. The resulting model is displayed by Fig. 3.11.

[2] Parts of this subchapter were already published in [69]

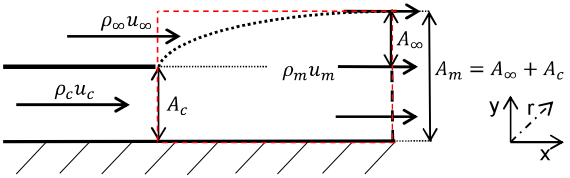


Fig. 3.11 Mixing model of hot gas and coolant with control volume (red dashed line)

For this mixing model the simplified conservation equations can be written as [70]

$$\dot{m}_\infty + \dot{m}_c = \rho_m u_m A_m = \dot{m}_m, \tag{3.54}$$

$$\dot{m}_\infty u_\infty + \dot{m}_c u_c = \rho_m {u_m}^2 A_m, \tag{3.55}$$

$$\dot{m}_\infty \left(c_{p\infty} T_\infty + \frac{{u_\infty}^2}{2} \right) + \dot{m}_c \left(c_{pc} T_c + \frac{{u_c}^2}{2} \right) = \rho_m u_m A_m \left(c_{pm} T_m + \frac{{u_m}^2}{2} \right). \tag{3.56}$$

The hot gas mass flux is calculated using Eq. (3.44) and increases with increasing distance from the injection point. The coolant mass flux is calculated by Eq. (3.46) and stays constant downstream of the injection point. As in Sec. 3.2.4 the areas of hot gas and coolant are annuli. Using these assumptions, the properties of the gas mixture needed in Eq. (3.53) can be determined. Following Eq. (3.54) the mixture density is

$$\rho_m = \frac{\dot{m}_m}{u_m A_m}. \tag{3.57}$$

From Eq. (3.55) follows for the mixture velocity

$$u_m = \frac{u_\infty \dot{m}_\infty + u_c \dot{m}_c}{\dot{m}_m} \tag{3.58}$$

The heat capacity of the mixture can be calculated using the local mass fractions of hot gas and coolant [71]

$$c_{p,m} = \sum_i w_i c_{p,i}, \tag{3.59}$$

$$\text{with } w_i = \frac{x_i M_i}{M},$$

$$x_i = \frac{n_i}{n_{total}},$$

$$\text{and } n_i = \frac{m_i}{M_i}.$$

For determining the Stanton number of the mixture, the mixing temperature, the reference temperature of the mixture and the density and viscosity of the mixture for both temperatures must be known. The mixing temperature of hot gas and coolant can be calculated by [72]

$$T_m = \frac{\dot{m}_\infty c_{p,\infty} T_\infty + \dot{m}_c c_{p,c} T_c}{\dot{m}_\infty c_{p,\infty} + \dot{m}_c c_{p,c}}. \tag{3.60}$$

Further, the viscosities of hot gas and coolant at this temperature are determined. For the hot gas viscosity Eq. (3.26) is used. The coolant viscosity is calculated using Sutherland's model [73]

$$\mu_c(T) = \mu_0 \frac{T_0 + S}{T + S} \left(\frac{T}{T_0}\right)^{3/2}. \tag{3.61}$$

The parameters μ_0, T_0 and S depend on the coolant gas [74] and are given in Table 3.2.

Table 3.2 μ_0, T_0 and S for different coolant gases [74]

	μ_0	T_0	S
Helium	0.000019	273	79.4
Nitrogen	0.00001781	300.55	111
Argon	0.000021	273.15	165
Carbon dioxide	0.0000148	293.15	240

As next step, the viscosity of the gas mixture at mixing temperature is calculated using the viscosities of hot gas and coolant as calculated before. For the viscosity of the mixture the mixing model by Wilke [75] is used [76]

$$\mu_m(T) = \sum_i \frac{x_i \mu_i(T)}{\sum_j x_j \varphi_{ij}(T)}, \tag{3.62}$$

with the correction factor

$$\varphi_{ij}(T) = \frac{1}{2\sqrt{2}}\left(1+\frac{M_i}{M_j}\right)^{-0.5}\left[1+\left(\frac{\mu_i(T)}{\mu_j(T)}\right)^{0.5}\left(\frac{M_j}{M_i}\right)^{0.25}\right]^2. \tag{3.63}$$

For calculating the Stanton number (Eq. (3.21)) also the mixing gas properties at reference temperature (see Eq. (3.23)) are needed. To determine the reference temperature at a certain distance from the injection point the Prandtl number, isentropic exponent and Mach number of the mixture at this point must be known. The Prandtl number is given by

$$Pr_m = \frac{\mu_m c_{p,m}}{\lambda_m}. \tag{3.64}$$

Viscosity and heat capacity of the mixture were already given in Eqs. (3.59) and (3.62). The thermal conductivity of the mixture is given by the mixing model of Wassiljeva, Mason and Saxena [77,76]

$$\lambda_m(T) = \sum_i \frac{x_i\lambda_i(T)}{\sum_j x_j\varphi_{ij}(T)}. \tag{3.65}$$

As analogon to the viscosity, the correction factor $\varphi_{ij}(T)$ can again be determined using Eq. (3.63). The thermal conductivity of the hot gas (water vapor) as function of the local temperature can be calculated by [74]

$$\lambda_\infty(T) = \frac{1.5466\sqrt{T}\cdot 10^{-5}}{1+\frac{1737.3}{T}\cdot 10^{-12/T}} + 1.097\cdot 10^{-4}\left(10^{0.934\cdot 10^9\left(p/T^4\right)-1}\right)4.184\cdot 10^2, \tag{3.66}$$

where λ is in $\left[\frac{W}{mK}\right]$ and p is in $[atm]$.

For the coolant gases used in this work the thermal conductivity can be calculated using [74]

$$\lambda_c(T) = \frac{a\sqrt{T}}{1+\frac{b\cdot 10^{-c/T}}{T}}4.184\cdot 10^{-8}, \left[\frac{W}{mK}\right]. \tag{3.67}$$

The parameter a, b, c are different for every gas and are given in Table 3.3.

Table 3.3 Parameter for calculating the thermal conductivity [74]

	a	b	c
Helium	234700	43.54	10
Nitrogen	60400	224	12
Argon	37900	179.59	10
Carbon dioxide	460800	6212	10

The isentropic exponent of the mixture follows from Eq. (3.59) and the general definition of the isentropic exponent,

$$\gamma_m = \frac{\sum_i \frac{x_i \gamma_i}{\gamma_i - 1}}{\sum_i \frac{x_i}{\gamma_i - 1}}. \tag{3.68}$$

Using this and the mixture velocity and temperature as calculated before, the mixture Mach number is given by

$$Ma_m = \frac{u_m}{\sqrt{\gamma_m T_m R_m}} = \frac{u_m}{\sqrt{\gamma_m T_m \frac{R}{\left(\sum_i \frac{w_i}{M_i}\right)^{-1}}}}, \tag{3.69}$$

with $R = 8.314\ \frac{J}{mol\,K}$ the universal gas constant [78]. Based on the results from Eqs. (3.60), (3.64) and (3.68)-(3.69) the local reference temperature of the mixture can be determined. As last step, the viscosity and density of the mixture at this reference temperature must be known. The viscosity of the mixture at reference temperature can be calculated using the same approach as discussed before. The densities of hot gas and coolant at reference temperature are calculated by

$$\rho_i^* = \frac{p}{R_i T^*}, \tag{3.70}$$

where p is the constant pressure in the boundary layer. With that, the density of the gas mixture at reference temperature follows from the law of Amagat [79]

$$\rho_m^* = \left(\sum_i \frac{w_i}{\rho_i^*}\right)^{-1}. \tag{3.71}$$

Finally, all parameters for Eq. (3.53) are determined and the ratio of the heat transfer coefficients can be calculated.

3.3 Dual-Bell Nozzle

During the ascent of a rocket, the ambient pressure changes rapidly. Thus most of the time the nozzle flow is either over- or underexpanded, which leads to a reduced performance and dangerous side-load effects due to flow separation. Therefore, several concepts of altitude adapting nozzles were developed [80]. Foster and Cowles [81] presented the idea of controlling the flow separation in the nozzle by using a contour inflection. Based on this idea Fischer [82] developed a nozzle with a single contour inflection- the dual- bell nozzle. In the following, the general working principle and the application of film cooling in such a nozzle is discussed.

3.3.1 General Working Principle

The dual-bell nozzle is a one-step altitude adapting nozzle, which means it has two design modes each mode optimized for a certain flow regime. Therefore, it consists of a base nozzle, which is usually a RAO-type bell nozzle [83] and a nozzle extension with a larger half-opening angle than the base nozzle. The transition between the nozzles occurs at the contour inflection.

For high ambient pressure the dual-bell nozzle works at the sea-level mode as displayed by Fig. 3.12.

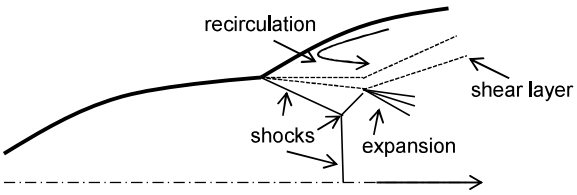


Fig. 3.12 Dual-Bell nozzle in sea-level mode adapted from [84]

In sea-level mode, a controlled and symmetrical flow separation occurs at the contour inflection. For a stable flow separation the inflection angle from base nozzle to nozzle extension is calculated such that the wall pressure predicted by Schmucker's or Summerfield's separation criterion [85,86] is reached behind the contour inflection [83].

For low ambient pressures the flow field changes and the dual-bell nozzle works at altitude mode (see Fig. 3.13).

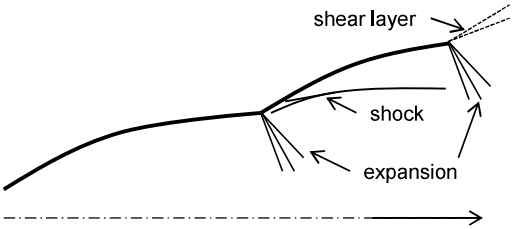


Fig. 3.13 Dual-Bell nozzle in altitude mode adapted from [84]

In altitude mode, the flow is fully attached to the walls of the nozzle extension. At the contour inflection the flow is accelerated by a Prandtl-Meyer expansion followed by a recompression shock in the nozzle extension redirecting the flow parallel to the wall. The contour inflection is usually designed as a sharp-edge. The shape of nozzle extension is designed by the method of characteristics for the desired wall pressure gradient (see Sec. 3.3.2).

3.3.2 Transition

At which altitude i.e. ambient pressure the flow in the dual-bell nozzle changes from sea-level mode to altitude mode is defined by the nozzle pressure ratio

$$NPR = \frac{p_0}{p_a}. \tag{3.72}$$

This ratio is defined for each nozzle in the design process. When the value of the NPR is equal or higher than the defined value transition to the altitude mode occurs.

The transition from the sea-level mode to the altitude mode is the most critical design criterion of a dual-bell nozzle. If the transition takes too much

time or results in an unsymmetrical flow separation, side load effects can occur, which are dangerous for the structural integrity of the nozzle. Therefore, a sudden transition between the flow modes is desired. The design criterion to face this problem is the wall pressure gradient of the nozzle extension [83]. Fig. 3.14 shows the static pressure distribution at the wall of a dual-bell nozzle.

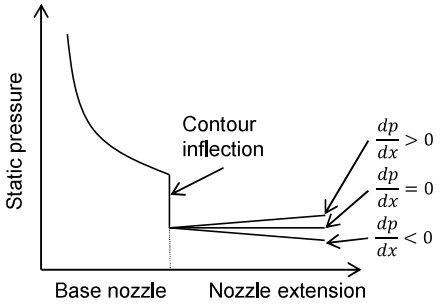


Fig. 3.14 Static pressure distribution along the nozzle wall with a sharp-edge contour inflection and inviscid expansion

In the base nozzle, the favorable pressure gradient causes a decrease of the static pressure over the running length. At the contour inflection the pressure drops (for inviscid flow) instantly to a lower level. For a viscous flow, the pressure drops not at one point but over a finite length. This is called the inflection region. The length of this region increases with increasing boundary layer thickness at the end of the base nozzle. Due to the negative pressure gradient in this region the separation point can then move to different positions, which can induce critical side load effects [87]. Therefore, a small inflection region is desirable.

In the nozzle extension three different wall pressure gradients are possible. Each of them results in a different position of the lowest static pressure reached in the nozzle extension.

For a favorable pressure gradient in the nozzle extension, the position of the lowest pressure is at the nozzle's exit. This leads to an uncontrolled flow separation during transition for a wide range of ambient pressures until the ambient pressure finally matches the exit pressure of the nozzle [84].

For an adverse pressure gradient, the position of the lowest pressure is at the beginning of the nozzle extension. This leads to a quick transition, since

the lowest pressure reached in the nozzle extension is at the contour inflection, so if the flow starts to attach to the walls of the nozzle extension the wall pressures there will always be higher than the ambient pressure and with that prevent the flow from separating again [83].

The third, theoretically possible pressure gradient is the constant wall pressure gradient. It also leads to a quick transition, since the pressure needed for a reattachment of the flow is reached homogenously in the whole nozzle extension [84]. However, this wall pressure gradient is technically hard to realize and can for even small fluctuations in the ambient pressure easily result in an unstable transition, where the flow jumps from sea-level to altitude mode and back inducing strong side loads in the structure.

Thus inflection angle, wall pressure gradient in the nozzle extension and boundary layer thickness at the end of the base nozzle are the most critical design parameters for the flow transition [88]. However, other studies showed also an influence of the inflection point geometry on the transition behavior (see [89]). Additionally, it has to be mentioned that even though the concept of this nozzle is several decades old so far no real engine with a dual-bell nozzle exists, since some problems like the side load effects during flow transition are still unsolved.

3.3.3 Film Cooling in Dual-Bell Nozzles

For film cooling in dual-bell nozzles usually a supersonic coolant film is injected upstream of the contour inflection. The coolant film expands at the inflection point into the nozzle extension. The influence of this coolant film on the transition behavior of the nozzle was investigated by several authors [90–92].

The injection of a coolant flow influences the local thermophysical properties of the boundary layer flow at the end of the base nozzle. This results in changes of the boundary layer height and the Prandtl-Meyer expansion at the inflection point. Film cooling can therefore lead to an increased inflection length and side loads. This effect was found to intensify with increasing blowing ratio [88]. Therefore, the coolant injection conditions must be well adjusted to the nozzle's flow behavior. Proshchanka et al. [90] found that with the right injection conditions flow transition can be shifted to higher values of NPR and the movement of the separation point in the inflection

region is slower, which results in lower side loads. Also a more recent study by Schneider et al. [92] showed that film cooling can be used for active transition control by adjusting the coolant mass flow.

Additionally, several studies showed a good cooling effect in the nozzle extension for a supersonic film injected at the end of the base nozzle [90,91]. Martelli et al. [91] found for their numerical data a simple correlation, which can be used for a rough prediction of the cooling efficiencies in the dual-bell nozzle

$$\eta = 4.768 \left(\frac{c_{p,\infty}}{c_{p,c}} \frac{x_s}{Fs} \right)^{-0.38} . \tag{3.73}$$

However, this correlation does not work well at the contour inflection [91].

4 Experimental Setup

4.1 Test Facility

The experiments have been conducted in a detonation based short-duration rocket nozzle flow simulation facility (see Fig. 4.1), which was designed and built by Yahiaoui and Olivier [93].

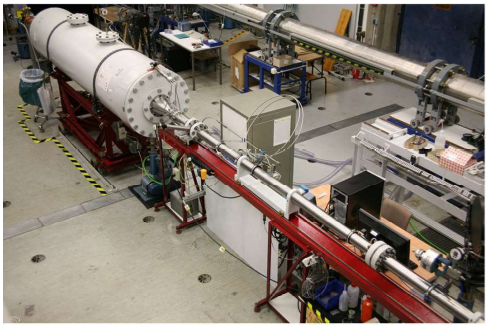


Fig. 4.1 Test facility

Short-duration detonation-based facilities can provide high pressures and temperatures and are therefore often used for the investigation of high enthalpy flows, like rocket-engine-like flows [94]. The main advantage of using these facilities is that due to the very short testing times of a few milliseconds, cooling of the facility walls and models is not needed since the temperature rise is negligibly small and isothermal wall conditions can be assumed. The facility is based on the detonation-tube technique. As shown in Fig. 4.2 it consists of a vacuum tank, a conical nozzle, a detonation tube of 10 m length and a 3 m long damping section. The inner diameter of the tube amounts to 60 mm [39].

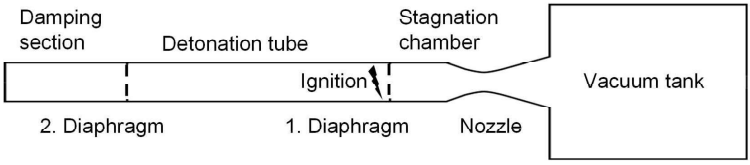


Fig. 4.2 Schema of the test facility

For an experiment the evacuated detonation tube is filled with hydrogen and oxygen gas with a ratio of oxidizer to fuel (ROF) of 8, which is a stoichiometric mixture. After filling, the gas mixture is given about 15 min for final mixing and adjusting to the temperature of the facility. Then the gas is ignited with a 1.3 kV electric spark close to a 1 mm thick steel diaphragm (1. diaphragm) separating the tube and the nozzle. Deflagration-to-detonation transition occurs closely to the diaphragm [39], such that a fully developed planar detonation wave starts propagating through the reactive gas towards the damping section. The pressure jump across the detonation wave causes a fast rupture of the diaphragm. Behind the detonation wave a Taylor expansion occurs and slows the burnt gas down to very low velocities in the nozzle stagnation chamber. A quasi-steady nozzle flow establishes after a short starting transient. The vacuum tank guarantees a low pressure at the nozzle exit, which is required to establish a supersonic nozzle flow. When the detonation wave ruptures the second diaphragm, it runs into a damping section operated at near vacuum. There the detonation wave extinguishes and propagates as shock wave into the vacuum and reflects at the end of the tube. By using this damping section the tubes end can be protected from high thermal loads and the testing time is increased [95,93]. The useful steady-flow testing time ends by the arrival of the expansion wave, which is generated by the bursting of the damping section diaphragm, in the nozzle stagnation chamber. The useful testing time in the experiment amounts to several milliseconds and varies with the initial conditions of the detonation. This procedure can also be seen in Fig. 4.3, which represents the ideal wave diagram calculated with KASIMIR [96].

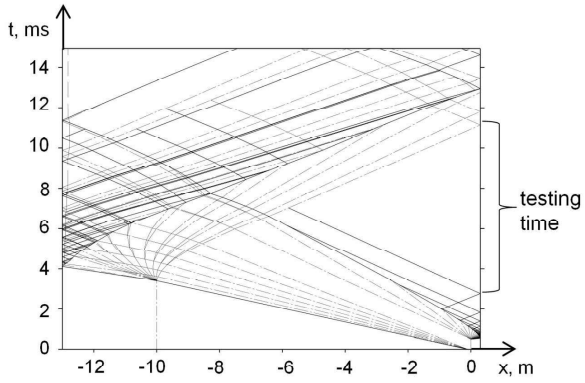


Fig. 4.3 Ideal wave diagram as calculated with KASIMIR

The detonation wave and the reflected shock waves are represented as solid thick lines, whereas the expansion fans are shown as dashed–dotted lines. In the presented case, the initial conditions of the calculation assumed vacuum in the nozzle and in the damping section and a stoichiometric mixture of hydrogen and oxygen in the detonation tube. There is a delay in the rupture of the first diaphragm, because for the calculation a time delay of 0.5 ms was set. It can be seen that after a short starting time there are no disturbances left in the nozzle reservoir section, such that quasi-steady test conditions can be assumed until the expansion fan from the damping section arrives.

4.2 Conical Nozzle[3]

The test section of the facility is the conical nozzle, which is attached to the detonation tube (see Fig. 4.4). The most important geometrical data of this nozzle are listed in Table 4.1.

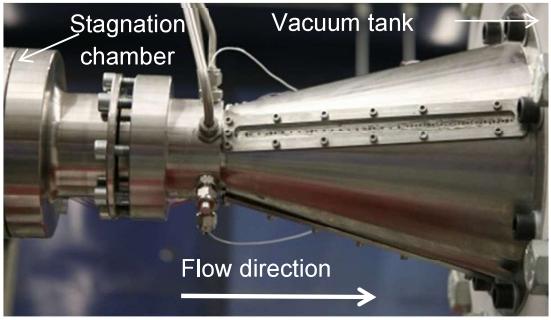


Fig. 4.4 Conical nozzle

[3] The experimental setup of the conical nozzle, the film cooling inlets and coolant supply were designed by Yahiaoui and presented in [39]. Also his CAD data of the conical nozzle was used for this chapter. The setup used in this work differs from the original setup in the following points: pressure sensor in the stagnation chamber, detonation velocity measurement method, measuring amplifiers, data acquisition for experiments without coolant injection, data evaluation program. In addition, the test procedure and facility control was changed to guarantee a safe operation of the facility.

Table 4.1 Geometrical data of the conical nozzle ([39] and CAD data)

Length of expansion part, mm	340
Throat diameter, mm	15.96
Half opening angle, °	15
Throat radius of curvature, mm	12
Expansion ratio (A_{exit}/A^*)	157

A section view of the nozzle is displayed by Fig. 4.5.

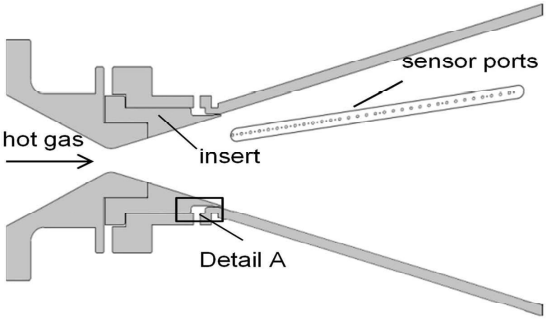


Fig. 4.5 Section view of the conical nozzle (for Detail A see Fig. 4.9)

It can be seen that the nozzle consists of three different parts. The converging nozzle part, an exchangeable insert and the nozzle expansion part. The exchangeable insert allows the configuration of the nozzle for experiments with and without coolant injection [39]. For experiments without coolant injection, the reference insert (see Fig. 4.6) is used. It provides a smooth transition without any steps or gaps from the insert to the nozzle expansion part.



Fig. 4.6 Reference insert

Also visible in Fig. 4.5 are the sensor ports for the thermocouples and Kulite pressure transducers. A picture of the inner nozzle wall with the installed sensors can be seen in Fig. 4.7. The thermocouples are flush-mounted and the Kulites are mounted at the end of an approx. 1.5 mm long pressure tap with a diameter of 0.8 mm. The distance between a thermocouple and a Kulite sensor amounts to 3.5 mm.

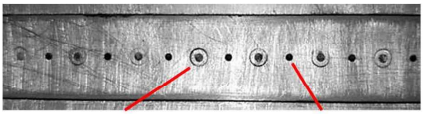


Fig. 4.7 Sensor ports

For the nozzle configuration with the reference insert the first thermocouple position is 98.5 mm and the first Kulite position is 101.9 mm downstream of the throat (measured along nozzle axis).

4.2.1 Coolant Supply

For experiments with coolant injection three different inserts are available. One of these inserts is shown by Fig. 4.8.

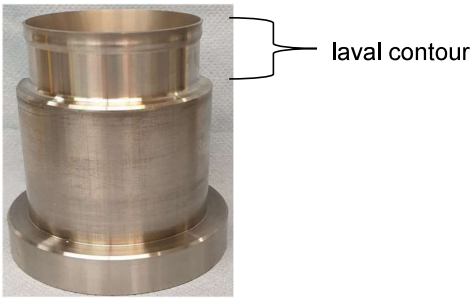


Fig. 4.8 Coolant insert s1

It is visible that, other than the reference insert, this insert is not smooth but contoured at the top. When installed, the insert provides a coolant injection slot with a laval-nozzle-like contour as displayed in Fig. 4.9.

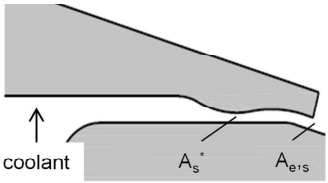


Fig. 4.9 Detail A

A_s^* represents the throat area of the slot and $A_{e,s}$ the exit area. Further geometrical data of the three different injection slots are given in Table 4.2.

Table 4.2 Geometrical data of the coolant slots (from [39] and CAD data)

Slot heights (s1/s2/s3), mm	0.46/0.41/0.56
Throat height of injection slot (s1&s2/s3), mm	0.3/0.36
Splitter thickness, mm	1
$A_{e,s}/A_s^*$, (s1/s2/s3)	1.55/1.38/1.57
Position of injection slot behind throat (along wall)	87 mm
A/A* of conical nozzle at injection position	14
Distance injection position to first thermocouple, (s1/s2/s3)	9.38 mm/ 9.59 mm/ 9.03 mm

The supply line of the coolant gas from the gas bottle to the nozzle can be seen in Fig. 4.10.

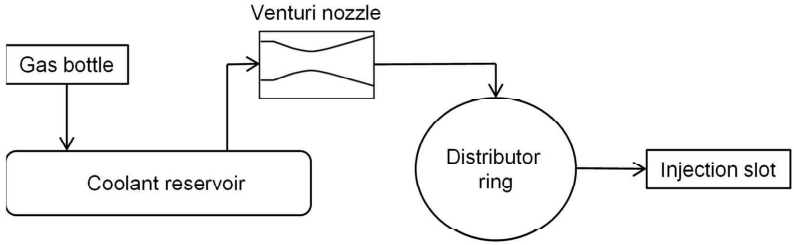


Fig. 4.10 Simplified scheme of the coolant supply line

The coolant gas is filled in a coolant reservoir until a certain coolant stagnation pressure in the reservoir is reached. For measuring this pressure a LEO 3 Keller manometer is used. From the reservoir the coolant flows through a venturi nozzle. By altering the throat area of the venturi nozzle

and the coolant stagnation pressure and temperature the coolant mass flux can be adjusted as can be seen from Eq. (4.1) [51]

$$\dot{m}_{coolant} = p_{0,c} A^*_{venturi} \sqrt{\frac{\gamma}{RT_{0,c}} \left(\frac{2}{\gamma+1}\right)^{\frac{\gamma+1}{\gamma-1}}}. \tag{4.1}$$

Downstream of the venturi nozzle, the coolant flows in the distributor ring, which provides a homogeneous distribution of the coolant gas before it is entering the injection slot. The coolant pressure in this ring is measured by two Kulite sensors. If the measured pressure is constant, also the coolant mass flux through the injection slot is constant. To guarantee a steady coolant flow during the testing time, the coolant injection has to start prior to the ignition [39]. For the presented experiments a time delay of 35 ms was sufficient.

As the coolant gas flows through the injection slot, its stagnation temperature is assumed to adapt to the nozzle wall temperature, due to the very small slot heights.

4.3 Measurement Technique

4.3.1 Static Pressure

The pressures in the nozzle stagnation chamber and the expansion part of the nozzle are measured by Kulite pressure transducers. These sensors are piezoresistive, which means a change in the pressure results in a change of the electrical resistance. For measuring the static pressure in the nozzle extension Kulite XCL-100 sensors with 3.5 bar and 7 bar absolute pressures were used. This type of sensor was chosen because of its ability to withstand conductive liquids and gases, which is important for the current application since the hot gas flow inside the facility consists of water vapor [39]. The compensated temperature range of these sensors is 25- 80°C.

The pressure transducer in the stagnation chamber has not only to endure the water vapor, but also a high thermal shock at the beginning of the measurement. Therefore, a Kulite HKS-11HP-375M sensor was used, which was specially designed for shock pressure applications. Its membrane has a

silicone based protective coating to protect it from liquids and thermal influence. For further thermal protection of the sensor a 4 mm thick steel plate (see Fig. 4.11) with Ø 0.8 mm holes was placed in front of the membrane, such that the hot gas is cooled before it hits the sensor's surface.

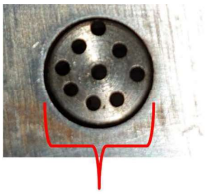


Fig. 4.11 Plate in front of the Kulite sensor used for measuring the stagnation pressure

Due to the low velocities of the subsonic flow in the nozzle stagnation chamber, the measured wall pressure is assumed to be equal to the stagnation pressure of the flow.

The measured voltage signal of all Kulites is converted to mbar using a sensor specific calibration factor. For the Kulites in the nozzle extension, this factor was determined by an in-situ calibration in the facility. The calibration factor of the Kulite in the stagnation chamber was taken from the calibration data provided by the sensor manufacturer.

4.3.2 Heat Flux

For the determination of the wall heat fluxes flush-mounted, coaxial thermocouples type E with a response time of 10 µs are used. These thermocouples consist of an inner Constantan core surrounded by an outer layer of Nickel-Chromium and provide with 63 µV/K a high sensitivity compared to other types of thermocouples. Due to the similar heat conductivities of the thermocouple material and the material of the nozzle wall (steel) the thermocouples were installed without any thermal isolation.

The temperature T as function of time is calculated from the measured thermocouple signal E^i in µV using the polynomial for type E thermocouples as given by DIN EN 60584-1 [97] (see Eq. (4.2)).

$$T = \sum_{i=1}^{n} d_i E^i \tag{4.2}$$

The coefficients d_i are listed in Appendix A. The heat flux is determined from the measured surface temperature T by the use of the Eq. (4.3).

$$\dot{q} = \frac{2\sqrt{\rho c k}}{\sqrt{\pi}} \sum_{i=1}^{m} \frac{T(0,t_i) - T(0,t_{i-1})}{\sqrt{t_m - t_i} - \sqrt{t_m - t_{i-1}}}, \tag{4.3}$$

with t the time and m the number of time intervals. This method was developed by Cook-Felderman [98]. The $\sqrt{\rho c k}$ value represents the product of the density, specific heat and thermal conductivity of the thermocouple. This value is determined by calibration for each thermocouple. The mean value of $\sqrt{\rho c k}$ for the used thermocouples is 8600 $\left[\frac{\mathrm{W}\sqrt{\mathrm{s}}}{\mathrm{m^2K}}\right]$ with an uncertainty of ± 300 $\left[\frac{\mathrm{W}\sqrt{\mathrm{s}}}{\mathrm{m^2K}}\right]$ [99]. This results for the calculation of the heat fluxes in Eq. (4.3) in an uncertainty of about ± 3.5%.

4.3.3 Detonation Velocity

The detonation velocity is determined by the signal of two coaxial thermocouples type E in the detonation tube. Thermocouples were used instead of pressure sensors due to their robustness. The wave velocity was determined by the successive initial jump in the signal of the two thermocouples. The thermocouples are placed at a distance of 3.5 m with an uncertainty of ±0.1 cm. Fig. 4.12 shows the signal of the two thermocouples over time.

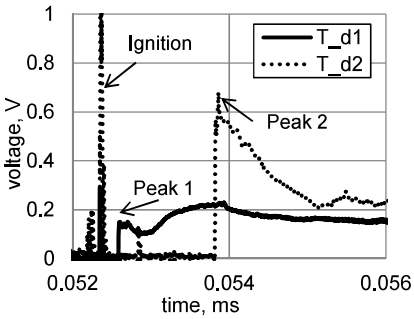


Fig. 4.12 Signal of the two thermocouples used for measuring the detonation velocity

Behind the very high peak caused by the voltage release during ignition two smaller peaks in the signal of each thermocouple are visible. By determining the time difference between these peaks and using the distance between the thermocouples, the velocity of the detonation wave can be calculated. The total uncertainty in the determination of the detonation velocity was about 3.4%.

4.3.4 Signal Recording

The sensor signals were amplified and filtered using an A2 Signal Conditioning Amplifier System by Micro Measurements. The amplification factor for the thermocouple signal was set to 1000, for the pressure transducers in the nozzle to 250 and for the pressure transducer in the stagnation chamber to 125. The low-pass filter was for all channels set to a cutoff frequency of 10 kHz. All sensor signals were sampled at 500 kHz. For experiments without coolant injection no trigger sensor was needed since the recording started with the ignition command send by the data acquisition software (LabVIEW). For experiments with coolant injection the Kulite sensor in the coolant distributor ring acted as trigger sensor [39]. The data acquisition system itself consists of a NI PXIe-1073 chassis, which contains a NI PXIe-6358, a NI PXIe-6356 and two NI PXIe-6133 multifunction data acquisition devices [39]. For the data evaluation a MATLAB program was written and used.

4.4 Stagnation Conditions

4.4.1 Experimental Conditions

By changing the initial conditions of the detonation, the stagnation temperature and pressure of the hot gas nozzle flow can be adjusted [39]. The presented experiments in this work were conducted with three different initial i.e. hot gas conditions (see Table 4.3).

Table 4.3 Experimental conditions (initial pressures and mixture ratios chosen from [93])

	Condition 1, C1	**Condition 2, C2**	**Condition 3, C3**
$T_{initial}$	373 K	293 K	373 K
$p_{initial}$	6 bar	6 bar	9 bar
u_{deto}	2904.5 m/s	2926.6 m/s	2926.1 m/s
T_0	3660 K	3685 K	3730 K
P_0	30 bar	40 bar	50 bar
ROF	8	8	8
Score depth of diaphragm	0.8 mm	0.8 mm	0.7 mm

T_{inital} represents the temperature of the gas mixture before detonation (see also Sec. 5.3). Due to the long resting time of the gas mixture in the tube between filling and ignition, it is assumed that the gas temperature is equal to the wall temperature of the detonation tube.
The initial pressure $p_{initial}$ of the gas mixture is adjusted during the filling process of the detonation tube.
Since the stagnation temperature cannot be measured in the presented experimental setup, it needs to be calculated. For determining the stagnation temperature from experimental values the Cantera software [100], which can be implemented in MATLAB was used [39]. This program needs the initial conditions of the gas mixture and the detonation velocity as input parameter for calculating the conditions of the gas behind the detonation wave. The velocity of the detonation wave u_{deto} is measured for each experiment (see Sec. 4.3.3) and was checked by comparing it to the values calculated with the code Chemical Equilibrium with Applications

(CEA) [101]. Since Cantera is very sensitive to the detonation velocity and small changes here can result in a diverging of the solution, also another approach for calculating the stagnation conditions of the burnt gas was used, which is the KASIMIR software tool. This code simulates a one-dimensional flow in the detonation tube and uses an exact Riemann solver for calculating the changes in the flow conditions caused by interactions of shocks and/or expansion waves [96]. The calculated stagnation conditions resulting from KASIMIR were very similar to the converged Cantera solution. However, the resulting values are valid for ideal conditions, which results in a slight overestimation of the real values. This can be seen when comparing the calculated stagnation pressure with the stagnation pressure measured in the experiment (see Fig. 4.13).

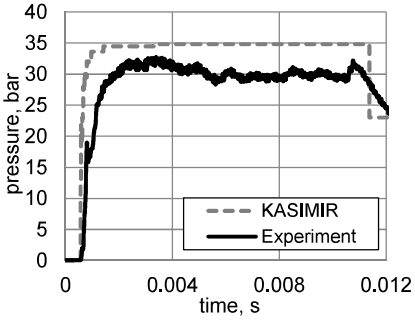


Fig. 4.13 Comparison of stagnation pressure calculated with KASIMIR to measured stagnation pressure for Condition 1

Due to the ideal conditions in the simulation, the calculated stagnation pressure is higher than the measured pressure. Therefore, for the definition of each condition in Table 4.3 the measured pressure values instead of the calculated ones were used. However, for the stagnation temperature of each condition the results of KASIMIR were assumed to be valid, since deviations of several Kelvin in the stagnation temperature have almost no effect on the nozzle flow conditions.

4.4.2 Reproducibility

For reliable and comparable experimental data it is crucial to match the stagnation conditions of the defined hot gas conditions as precise as possible. However, due to the manual filling process and other effects small

deviations between the experiments are inevitable. The deviations in the initial pressure of the mixture were in every experiment less than 1% of $p_{initial}$. Simulations using the CEA code showed that these deviations have no effect on the detonation and therefore on the stagnation conditions of the burnt gas. Additional to the deviations in the initial pressure are small deviations regarding the composition of the mixture. This results in an excess or shortage of hydrogen in the mixture. The maximum uncertainty for hydrogen in the mixture in all experiments is ±0.15 bar. This deviation has the biggest impact on the condition with the lowest initial pressure. Therefore, Table 4.4 shows the influence of this on the mixing ratio and detonation velocity of Condition 1.

Table 4.4 Deviations in the filling pressure of H_2 for Condition 1

	+0.15 bar H_2	**-0.15 bar H_2**
ROF	7.73	8.3
u_{deto}	2934 m/s	2873 m/s

The detonation velocities were calculated with the CEA code and differ by 61 m/s. Using these velocities and the mixture compositions, the differences in the stagnation temperatures and pressures of the burnt gas were determined with the Cantera program. It was found that the maximum difference in the stagnation temperature is 3.1 K with a difference in the stagnation pressure of 0.35 bar. These deviations are negligible. This means the observed uncertainties in the initial conditions of the experiments are small enough to guarantee a good reproducibility of the hot gas stagnation conditions. However, for each experiment additional to the initial conditions, the measured detonation velocity and stagnation pressure were checked to make sure that the experiment matches the desired hot gas stagnation conditions.

5 Influence and Prevention of Condensation in the Nozzle [4]

5.1 Detection of Condensation

Former experiments performed in the facility described in Sec. 4 showed an unexpected behavior for the heat flux measurements in the attached nozzle. As plotted in Fig. 5.1 the heat flux shows a strong decrease over time whereas the static pressure measured at nearly the same position shows an almost constant behavior. As a possible reason for this, condensation of the hot gas flow on the inner walls of the facility was assumed. This assumption was also supported by the fact that the inner walls of the facility were found to be wet after the experiments [39][5].

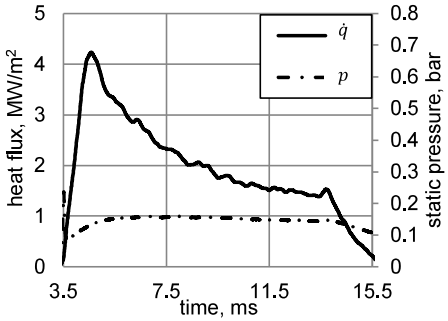


Fig. 5.1 Wall heat flux $\dot{q}$ and static pressure p over time measured about 120 mm downstream of the nozzle throat

That a low wall temperature of the facility can cause condensation of the hot test gas at the walls was already described by Owens and Hanson [103]. However, until now there was no evidence whether the unexpected heat flux behavior results from condensation. To investigate this, it was crucial to determine if there is condensation at the wall and at what time during the experiment condensation occurs. Since there is no optical access to the nozzle wall during the experiment another way of proofing condensation at

[4] The content of this chapter was already published in [102]

[5] Experiments (with and without film cooling) in the conical nozzle without heating system were first conducted by Yahiaoui [39]. The heat flux measurements were strongly affected by the condensation phenomena described in this chapter.

the wall was needed. Therefore, the inner nozzle wall was partly painted with a water-based paint, because the existence of liquid water was assumed to leave traces in the paint. Since condensation at the beginning of the test procedure (see Sec. 4.1) is not possible due to the lack of water vapor, condensation can only occur during the testing time, after the breakdown of the nozzle flow and during the venting of the facility. To prevent condensation of the water vapor in the facility after the breakdown of the nozzle flow and before venting, the nozzle walls were heated up prior to the experiment. The adjusted wall temperature was 300 K, which was determined by using the vapor-pressure data of water for a pressure of 40 mbar. This is the average pressure in the whole facility after breakdown of the nozzle flow. By this, not only condensation before venting was prevented, but also the liquid water which has formed during the testing time is evaporated and its traces in the paint are fixed. To assure also that the paint is not affected by condensing water forming during venting, i.e. when the pressure in the nozzle rises, the nozzle wall's temperature was increased to 350 K before starting the venting process. The traces in the paint after the experiment can be seen in Fig. 5.2 and can only result from liquid water, which was formed during the testing time. An analysis of the paint showed that it is locally washed out and there are tracks of water droplets parallel to the hot gas flow direction. Thus, there seems to be liquid water at the nozzle wall during the testing time.



Fig. 5.2 Washed out paint at the nozzle wall

5.2 Theoretical Influence of Condensation

Many effects can cause a condensation of hot gas in a nozzle. However, for the presented case the superheated water vapor has very high stagnation temperatures, such that condensation is not expected in the nozzle core flow as a result of cooling due to expansion as observed, e.g., in shock tubes or nozzle flows with lower stagnation temperatures [104,105]. In addition, there are no strong shocks in the nozzle, which could lead to condensation of the main flow as a result of local pressure jumps. So the observed condensation can only result from the fact that the wall temperature is lower than the local saturation temperature of the hot gas. In that case, there is a region in the boundary layer at the wall where the hot gas is cooled down to temperatures, which are lower than the saturation temperature and consequently condensation starts. Therefore, the occurrence and influence of condensation is assumed to be restricted on this very thin boundary layer region at the wall. The saturation temperature is pressure dependent and given by the vapor pressure curve (see Fig. 5.3).

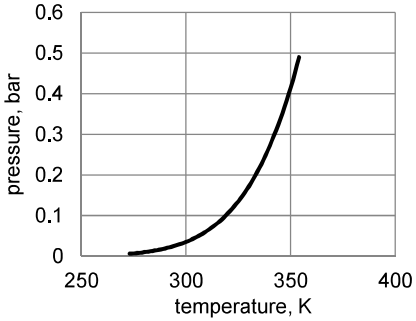


Fig. 5.3 Vapor-pressure curve of water [106]

Whether the hot gas condensates as film or dropwise depends on the contact angle between condensate and wall and results from the type of condensing gas and the wall material. For contact angles lower than 90° film condensation occurs [107]. In the present case, the hot gas is water vapor and the wall is a metallic surface. Lienhard et al. [108] reported for this combination a contact angle of 50°. Thus film condensation will occur. As mentioned before the film condensation will only take place in a very thin region near the wall, where the local temperature becomes less than the saturation temperature. Further, it is assumed that the flow velocity of the

film is negligible compared to the hot gas flow and the static pressure in the film is equal to the local static pressure of the hot gas. The resulting condensation model and its energy balance including the liquid film and wall surface is shown in Fig. 5.4.

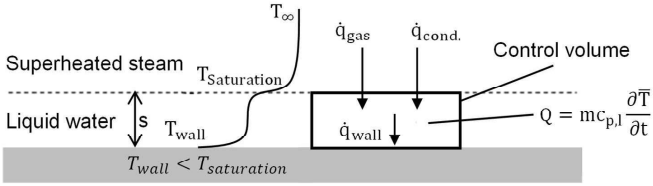


Fig. 5.4 Simplified temperature profile and energy balance for condensation of superheated steam on a cold surface

When the superheated steam with the local static temperature T_∞ cools down to its saturation temperature the heat flux $\dot{q}_{gas}$ enters the considered control volume at the vapor-liquid interface. As the temperature drops below the saturation temperature, the hot gas starts to condensate releasing the heat of condensation $\dot{q}_{cond.}$. This heat flux results from the difference in the specific enthalpies of gaseous (*g*) and liquid (*l*) water

$$\Delta h_v = -\left(h_g - h_l\right), \tag{5.1}$$

which decreases with increasing pressure [109]. The released heat flux of condensation can then be calculated by

$$\dot{q}_{cond} = \dot{s}\rho_l \Delta h_v, \tag{5.2}$$

with ρ_l the density of liquid water and the growing rate $\dot{s}$ of the water film, which for a detonation tube was for example reported by Sanders et al. [110] as $\dot{s} = 0.66 \cdot 10^{-3}$ m/s. For the determination of the heat flux $\dot{q}_{gas}$ it is assumed that the liquid water film behaves like a solid wall with a wall temperature equal to the saturation temperature. In that case $\dot{q}_{gas}$ is the same as the wall heat flux of a flow without condensation (*nc*) for an isothermal wall with a wall temperature equal to the saturation temperature. The heat transfer is then only a function of local flow properties and the temperature difference

$$\dot{q}_{gas} = \dot{q}_{wall,nc} = St\rho_\infty u_\infty (h_0 - h_s) = \alpha_g (T_0 - T_s). \tag{5.3}$$

As displayed by Fig. 5.4 $\dot{q}_{gas}$ and $\dot{q}_{cond.}$ enter the liquid water film. This water film stores a certain amount of heat *Q*, which depends on its heat

capacity $c_{p,l}$ and mass, while heating up over time. If the water film heats up such that its mean temperature $\bar{T}$ becomes higher than the saturation temperature it starts to evaporate. Thus the heat flux per unit width, which is absorbed by the liquid water film, results from the unsteady heat conduction and can be written as

$$\dot{q}_l = s\rho_l c_{p,l} \frac{\partial \bar{T}}{\partial t}. \tag{5.4}$$

Using Eqs. (5.2)-(5.4) the resulting wall heat flux $\dot{q}_{wall}$ is given by

$$\dot{q}_{wall} = \dot{q}_{gas} + \dot{q}_{cond} - \dot{q}_l = \alpha_l (T_s - T_w). \tag{5.5}$$

Comparing Eqs. (5.3) and (5.5) the influence of condensation on the local wall heat fluxes can be seen. Looking at the temperature differences it shows that without condensation the driving temperature difference of the heat flux is about a hundred times higher than for the case with condensation. However, for the case with condensation, the heat transfer coefficient is up to 700 times higher, as shown in Table 5.1.

Table 5.1 Ratio of heat transfer coefficients for liquid water and condensing steam to that of superheated steam (which behaves like a gas [111]) [112]

i	α_i/α_g
Liquid water	10-30
Condensing steam	100-700

Therefore, the resulting wall heat fluxes at the beginning of the run where there is still no liquid water film for the flow with condensation are expected to be much higher than for the case of a flow without condensation. In order to avoid condensation effects at the wall an electrical heating system has been installed, which is explained in the following chapter.

5.3 Heating System

In order to heat the detonation tube, stagnation chamber and nozzle, an electrical heating system has been installed (see Fig. 5.5). It consists of resistance heating wires (Isopad IS-SP-V) with a heating power of about 100 W/m. Each section of the facility has its own heating circuit, such that different wall temperatures for e.g. the nozzle and the tube can be adjusted. The heating wires are wrapped helically around the tube or nozzle, providing wall temperatures up to 373 K. Setting and controlling of the outer surface temperature is done by temperature controllers (Isopad Icon 4848) and type K thermocouples mounted directly on the outer tube wall and nozzle surface. To ensure uniform temperature distribution and to minimize heat losses a 50 mm thick rock wool insulation around the tube has been applied (see Fig. 5.6).

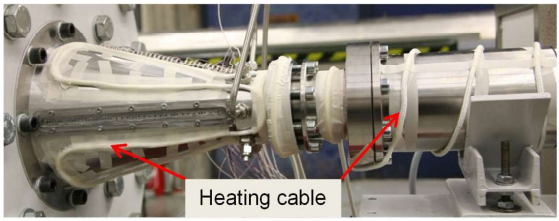


Fig. 5.5 Nozzle, stagnation chamber and tube with installed heating wires

For the parts of the facility were the rock wool tube isolation could not be installed, as for example at the flanges or the nozzle, specially manufactured mats filled with rock wool were used for isolation. At least three hours are needed to heat up the facility. During the experiment itself, the heating system is switched off to prevent an electrical influence on the thermocouples.

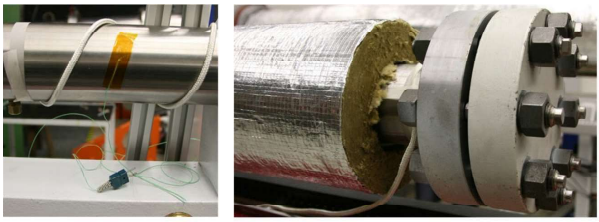


Fig. 5.6 Thermocouple for the control of the outer wall temperature (left) and rock wool isolation (right)

5.4 Experiments with Heating System

5.4.1 Heating the Attached Nozzle

Based on the arguments given in Sec. 5.2 experiments with a nozzle wall temperature equal to the evaporation temperature of water for the highest static pressure in the expansion part of the nozzle were conducted. For experiments with condition 1 this temperature is about 330 K. The exemplary heat flux histories over time at two positions downstream of the throat for the heated and unheated case are shown in Fig. 5.7.

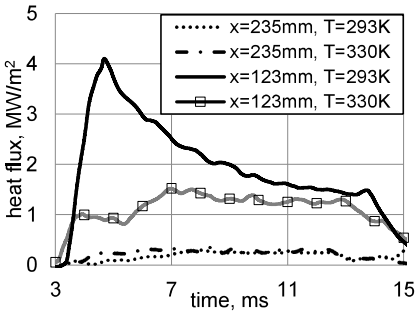


Fig. 5.7 Comparison of heat fluxes near the throat (x= 123 mm)) and far downstream (x= 235 mm), (Condition 1)

Looking at the heat flux histories at the beginning of the nozzle expansion (123 mm downstream of A*) two dominant differences between the heated

and unheated case can be seen. For the heated case the wall heat flux is almost constant over the whole testing time, whereas the wall heat flux for the unheated case shows after a sharp rise a permanent decrease over time. Comparing the absolute heat flux values it can also be recognized that the heat fluxes for the heated case are much lower than the ones of the unheated case. These results fit well to the theoretical investigations in Sec. 5.2. As the superheated steam starts to condensate at the beginning of the testing time the heat transfer coefficient and with that the wall heat flux rises. In Table 5.2 the wall heat flux for the unheated case, as well as the temperature difference in Eq. (5.5) at the beginning of the testing time is compared to the wall heat flux and temperature difference (see Eq. (5.3)) for the heated case.

Table 5.2 Heat fluxes and temperature differences at the *x*= 123 mm position in the nozzle extension

	Heated	**Unheated**
$\dot{q}_{measured}$	1.13 $\frac{\mathrm{MW}}{\mathrm{m}^2}$	4.08 $\frac{\mathrm{MW}}{\mathrm{m}^2}$
ΔT	3320 K	40 K

Assuming for the heated case that the water stays gaseous and no condensation occurs the ratio of the heat transfer coefficients for both cases can be calculated by

$$\frac{\alpha_{unheated}}{\alpha_{heat}} = \frac{\frac{\dot{q}_{unheated}}{\Delta T_{unheated}}}{\frac{\dot{q}_{heated}}{\Delta T_{heated}}}. \tag{5.6}$$

The resulting value shows that the unheated heat transfer coefficient is about 300 times higher than the one of the heated case. Comparing this result with the values given in Table 5.1 it can be seen that this ratio fits very well to the heat transfer coefficient ratios of condensing steam. Thus the wall heat flux at *x*= 123 mm for the unheated case in Fig. 5.7 indicates that the water vapor starts to condensate as the nozzle flow builds up. Its decrease over time can be explained by the fact that a growing liquid water film at the wall leads to a lower heat transfer than condensing steam i.e. the liquid water acts as cooling film. Even for the very short testing time the nozzle wall heats up by about 40 K, which explains why at the end of the testing time the differences between the unheated and heated heat flux values become very small, because here the water film is evaporating

again. Therefore, for a longer testing time with non-isothermal walls this condensation effect would, after a short starting time, have no influence on the heat flux measurement.

In addition, the local static pressure in the nozzle is important for the formation of liquid water at the wall. Looking at the wall heat fluxes at the end of the nozzle in Fig. 5.7 no deviation in the values exceeding the measurement uncertainties can be seen. This can be explained by the fact that at this location the static pressure is much lower than at the x= 123 mm position due to the expansion of the flow in the nozzle. With the static pressure also the saturation temperature decreases, such that condensation does not occur at the far downstream positions in the unheated nozzle. Therefore, condensation and its influence is a very local and time restricted effect in the presented experimental nozzle setup.

To check if adjusting the nozzle wall temperature to the local saturation temperature is enough to get rid of the condensation effect in the heat flux measurements, the nozzle walls were heated up to different temperatures, which were lower, higher or equal to the saturation temperature (~330 K). The resulting time averaged heat flux values over distance from the nozzle throat are displayed by Fig. 5.8. It can be seen that the heat fluxes measured for nozzle wall temperatures lower than the saturation temperature diverge remarkably from the heat fluxes measured at nozzle wall temperatures equal or higher than the saturation temperature. This is especially the case for the most upstream positions, because here the relatively high static pressures shift the saturation temperature to higher values. When heating the nozzle wall to the saturation temperature the heat flux values drop to a much lower level and remain there even for higher wall temperatures. Thus, the condensation effect in the data is successfully eliminated by heating the walls to saturation temperature. Due to the very high stagnation temperature of the flow, the influence of the increased nozzle wall temperature and with that lower temperature difference in Eq. (5.3) on the heat flux is negligible small.

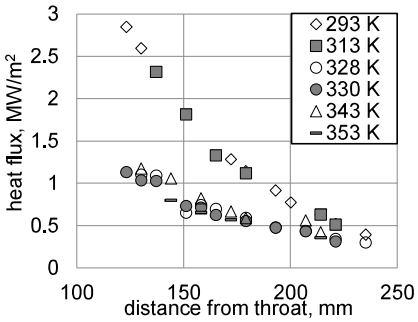


Fig. 5.8 Time averaged heat fluxes along nozzle wall for different wall temperatures, (Condition 1)

Fig. 5.9 shows the static pressures for the heated and unheated case. At all sensor positions there is no deviation in the values, which is larger than the measurement uncertainty.

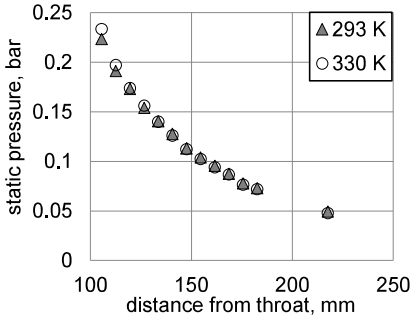


Fig. 5.9 Static pressure distribution for the heated and unheated nozzle (Condition 2)

This supports the assumption in Sec. 5.2 that the pressure of the water film adapts to the local static pressure of the flow. The static pressures are other than the heat fluxes unaffected by the occurrence of condensation.

5.4.2 Heating the Detonation Tube and Nozzle Stagnation Chamber

The detonation wave causes locally very high pressures up to 1000 bar in the detonation tube. Behind the detonation wave the hot gas expands into the stagnation chamber of the nozzle and the pressure drops (for the used

set of hot gas conditions) to values of 30-50 bar. Referring to the vapor-pressure diagram a wall temperature of about 500 K is needed for preventing condensation of the hot gas in the stagnation chamber. For a prevention of condensation in the detonation tube, even higher wall temperatures would be needed. In the current experimental setup an adjustment of the wall temperatures to these high values is not feasible. Therefore, it was investigated if condensation in the tube and the stagnation chamber have any harmful effect on the experiments in the attached nozzle. Since the previous experiments in the nozzle showed that the upstream existence of liquid water has no effect on the local measurements the possible influence of condensation in tube and stagnation chamber is assumed to be limited to the nozzle flow's stagnation conditions. The condensation of gas in the detonation tube and stagnation chamber results in a loss of gaseous mass, which causes a decrease in the stagnation pressure over time. However, the stagnation pressure measurements showed no significant decrease in pressure over testing time so this effect seems to be negligible. Nevertheless, the detonation tube and stagnation chamber were heated to 373 K for experiments with condition 1 and 3 for an accelerated drying of the tube after the experiment. By increasing the wall temperature of the tube also the initial temperature of the detonating gas increases, which has a huge influence on the final stagnation pressure. A higher initial temperature leads to a lower detonation velocity due to the increased dissociation and therefore less energy release in the detonation wave [113]. Because of this, the stagnation pressure decreases from condition 2 to condition 1 in Table 4.3. The initial pressure stays the same, but the initial temperature is increased by 80 K. As a conclusion it can be said that for the presented experiments the heating of the tube has a much larger effect on the nozzle's stagnation conditions than the condensation of water at the walls. Therefore, condensation in the detonation tube and nozzle stagnation chamber is accepted in the following experiments.

5.4.3 Heater Settings for Different Hot Gas Conditions

In the following experimental investigations the influence of condensation on the measurements in the conical nozzle is prevented. Following the results from Sec. 5.4.1 and Sec. 5.4.2 it is sufficient to heat the nozzle walls up to the local saturation temperature of water vapor. The wall temperature needed for each condition is given in Table 5.3. The wall temperature of the

nozzle stagnation chamber was set to 373 K and was equal for each condition.

Table 5.3 Nozzle wall temperatures needed for condensation free experiments

Condition	Nozzle wall temperature, K
1	330
2	340
3	350

6 Reference Flow

In the following chapter the reference nozzle flow, meaning the hot gas flow without coolant injection, is investigated. This data is needed for qualifying the film cooling efficiencies in the experiments with coolant injection later on. The presented experiments were conducted with three different hot gas conditions (see Table 4.3). The nozzle walls are assumed to be isothermal at the adjusted temperature needed for the prevention of condensation (see Table 5.3).

6.1 Testing Time

The testing time was defined as the time interval in which the hot gas flow conditions can be assumed to be almost constant. Therefore, the curves of stagnation pressure, static pressure and wall heat flux over time have to be considered. The graphs of the stagnation pressures over time for all used hot gas conditions are displayed in Fig. 6.1.

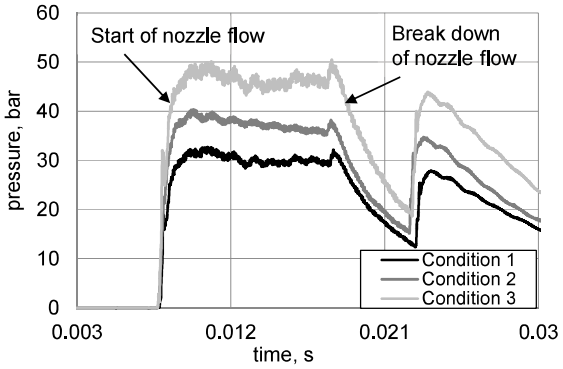


Fig. 6.1 Stagnation pressures over time for all three conditions

It can be seen that when the nozzle flow is fully established, the stagnation pressure reaches an almost constant level for several milliseconds. The time interval of the quasi-steady state is slightly different for each experiment and hot gas condition. At the end of this time interval the pressure drops rapidly due to the incoming expansion wave from the damping section (see Sec. 4.1) and the nozzle flow breaks down.

The static pressures over time at various positions in the nozzle expansion part for condition 1 are shown in Fig. 6.2. The jumps in the signals of the far downstream pressure transducers are due to a rise of the pressure in the vacuum tank. At a certain time the pressure in the vacuum tank becomes higher than the pressure at the nozzle exit and a shock forms in the nozzle, which results in the observed pressure jump.

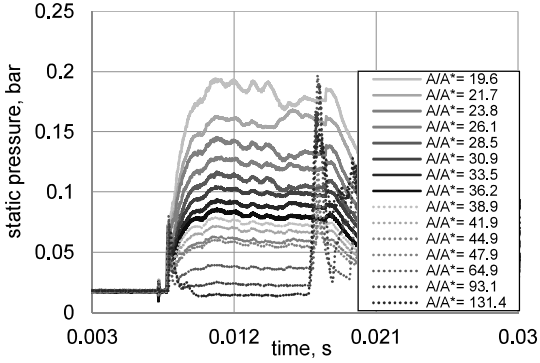


Fig. 6.2 Static pressure over time at different A/A* for condition 1

In Fig. 6.3 the wall heat fluxes at various positions in the expansion part can be seen. The signals of the wall heat fluxes vary stronger than the ones of the static pressures. A reason for this can be large scale turbulent fluctuations in the boundary layer. However, also in the wall heat flux signals a time interval with almost constant values can be found.

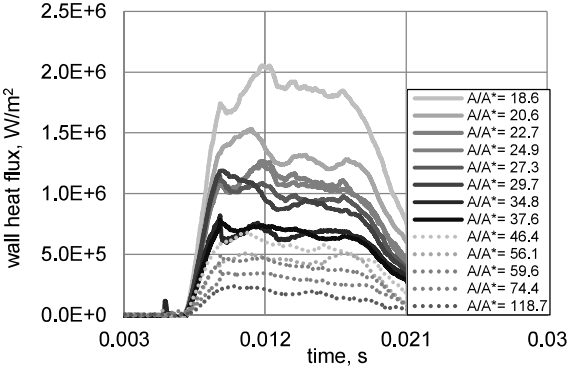


Fig. 6.3 Wall heat fluxes over time for condition 1, pressure in the vacuum tank lower than in Fig. 6.2

For determination of local flow conditions along the nozzle wall the sensor data was time averaged. Due to the fluctuations in the signals and other restrictions, as for example the occurrence of shocks in the static pressure signals, only 1 ms of the testing time was used to evaluate the measured data. This millisecond was chosen such that over the complete averaging period the stagnation pressure of the flow has a nearly constant value, which is equal to the value of the standard stagnation pressure of the adjusted hot gas condition (see Table 4.3). For the used sampling rate of 500 kHz the average of 500 measured data points was used for the determination of the local averaged values.

For each hot gas condition the time averaged values of the static pressures and wall heat fluxes over the distance from the nozzle throat, measured along the wall, are given in Fig. 6.4 and Fig. 6.5.

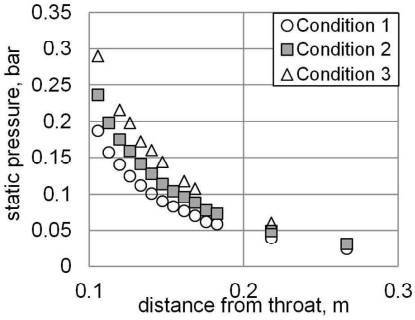


Fig. 6.4 Time averaged static pressures over distance from nozzle throat for all three conditions

Fig. 6.4 shows for each condition a smooth decrease in the static pressures with increasing distance from the nozzle throat. This indicates a favorable pressure gradient and during the measuring time window no shocks in the flow.

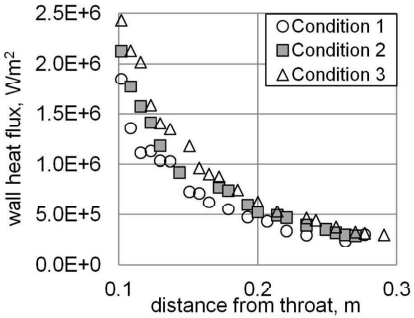


Fig. 6.5 Time averaged wall heat fluxes over distance from nozzle throat for all three conditions, for defect thermocouple T2 for condition 2 and 3 the heat flux value was approximated by a polynomial derived from the measured values.

The wall heat fluxes in Fig. 6.5 slightly increase from condition 1 to condition 3 due to the proportional behavior of stagnation pressure and heat flux and because of the higher stagnation temperature. The heat fluxes along the nozzle wall decrease continuously as expected due to the expansion of the hot gas in the divergent nozzle section.

With this procedure of choosing the averaging period a good reproducibility of the experimental data is achieved. Since the wall heat flux measurements are far more sensitive to disturbances than pressure measurements Fig. 6.6 shows the local wall heat flux values for three different experiments for hot gas condition 1. It can be seen that the deviations between the values is small such that the reproducibility of the heat flux measurements can assumed to be good.

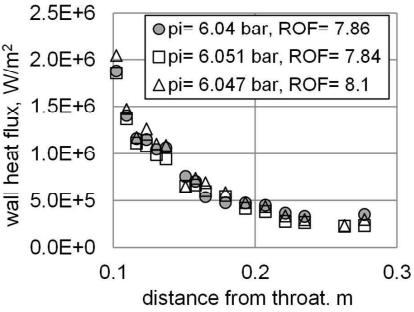


Fig. 6.6 Reproducibility of wall heat fluxes for condition 1

6.2 Boundary Layer

Due to the design of the experimental setup and the harsh hot gas conditions direct boundary layer measurements were not feasible. However, for a first validation the displacement thickness of the flow was calculated by determination of the effective area ratio of the flow using the measured static pressures and stagnation pressure. The effective nozzle area ratio can be calculated by Eq. (6.1) [114]

$$\frac{A^*}{A} = \frac{\left(\frac{p}{p_0}\right)^{\frac{1}{\gamma}} \sqrt{\frac{2}{\gamma-1}\left[1-\left(\frac{p}{p_0}\right)^{\frac{\gamma-1}{\gamma}}\right]}}{\left(\frac{2}{\gamma+1}\right)^{\frac{1}{\gamma-1}} \sqrt{\frac{2}{\gamma+1}}}, \tag{6.1}$$

By subtracting the effective flow diameter from the geometrical diameter of the nozzle the displacement thickness is calculated. For a comparison to literature a correlation developed by Edenfield [53] for the displacement thickness in the expansion part of a nozzle with turbulent flow

$$\delta^* = 0.42 x Re^{-0.2775}, \tag{6.2}$$

was chosen. This correlation is valid for Reynolds numbers in the range of 10^3-10^7 and Mach numbers from 5 to 22 [54]. In Fig. 6.7 the displacement thickness calculated from the measured pressures and the displacement thickness according to Eq. (6.2) are displayed.

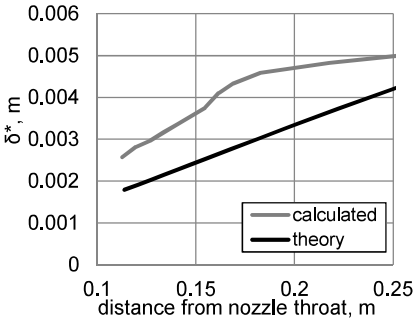


Fig. 6.7 Calculated displacement thickness from experimental data and theoretical displacement thickness as given by Eq. (6.2) plotted along the wall

It can be seen that the displacement thickness calculated from the experimental values is higher than the theoretical thickness. This may result from the fact that the Edenfield correlation was derived for hypersonic flow and the present nozzle flow does not fulfill this criterion, since the Mach numbers of the flow are in the supersonic regime (see Fig. 6.16).

To determine the character of the boundary layer, flow conditions of the conical nozzle were compared with those, whose boundary layers were proven to be turbulent (see Table 6.1). The nozzle data for the comparison was provided by Ariane Group [115] and consist of data from Vulcain 2 and the calorimeter nozzle program (CALO) [116]. All flow conditions given in Table 6.1 are for the throat of the nozzles.

Table 6.1 Comparison of unit Reynolds numbers in the nozzle throat for all conditions of the conical nozzle and data from CALO nozzle tests and Vulcain 2 [115]

	Propellants	**p_0, bar**	**d*, mm**	**ρu, kg/(m²s)**	**μ, Pas**	**Re_e, 1/m**
Vulcain 2	LOX/LH_2, ROF= 7.2	115	274	5178	1.08E-04	4.79E+07
CALO nozzle test	LOX/LH_2, ROF= 6	30	50	1311	9.98E-05	1.31E+07
CALO nozzle test	LOX/LH_2, ROF= 7.5	36	50	1659	1.06E-04	1.57E+07
Conical nozzle	GOX/GH_2, ROF= 8	30	16	1377	1.07E-04	1.27E+07
Conical nozzle	GOX/GH_2, ROF= 8	40	16	1831	1.08E-04	1.68E+07
Conical nozzle	GOX/GH_2, ROF= 8	50	16	2281	1.09E-04	2.08E+07

The throat data of the conical nozzle were calculated with the CEA program. Comparing the unit Reynolds numbers in the throat it can be seen that the unit Reynolds numbers of the conical nozzle are similar to those of the CALO nozzle and in the order of the unit Reynolds number of Vulcain 2. This indicates that after a certain running length the boundary layer in the conical nozzle is turbulent. This assumption is further checked in Sec. 6.3.

6.3 Numerical Approach

Since the experimental determination of all flow properties is not possible, numerical simulations with ANSYS Fluent [117] were performed. All these simulations were 2D, steady state and axisymmetric with an ideal but calorically imperfect gas. For all shown simulated data it was proven that the results are grid-converged.

For reliable results concerning the heat fluxes the chemical state of the hot gas flow needs to be considered. Due to the high temperatures and velocities of the flow in the expansion part of the nozzle a non-equilibrium or frozen state of the flow is most likely. Since the hot gas in the nozzle is the resulting burnt gas of the hydrogen-oxygen combustion, 37 basic chemical reactions are possible (see Sec. 3.1.1). For simplification only the most important species were taken into account and therefore all reactions containing H_2O_2 and HO_2 were neglected (see Table 3.1). The gas composition at the nozzle inlet was calculated with the CEA Program [101]. For the frozen state simulation this composition was unchanged for the complete nozzle flow. For all other cases the chemical reactions started at the beginning of the nozzle. Since the character of the boundary layer was not fully determinable from the experimental data, flow simulations for the laminar and the turbulent case were conducted[6]. For the turbulent case RANS simulations with the Spalart-Allmaras model were performed. This model was chosen, because it is recommended for nozzle flows in literature [118]. For the RANS simulations it was also assumed that the flow in the nozzle is fully turbulent.

In the following the laminar and turbulent simulations are exemplary presented for condition 1 (stagnation pressure 30 bar, stagnation temperature 3650 K) with an isothermal nozzle wall at 330 K. A section view of the nozzle flow is displayed by Fig. 6.8.

[6] The numerical simulations of the flow concerning chemical state and boundary layer behavior were already published in [69]

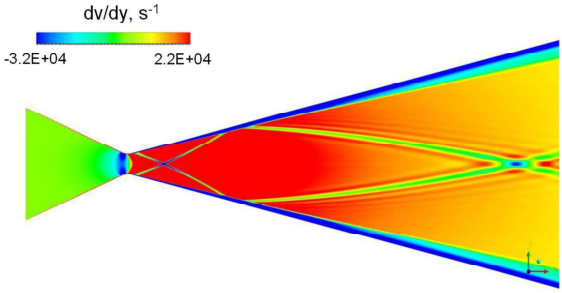


Fig. 6.8 Gradient of the radial velocity in the conical nozzle, condition 1, (ANSYS Fluent)

It can be seen that in the expansion part of the nozzle two weak oblique shocks form close behind the nozzle throat. These shocks are caused by the junction between the curved and conical shape of the nozzle extension. The shocks reflect at the nozzle wall and propagate through the nozzle towards the nozzle exit.

For the laminar simulations[7] the curves of the ratios of static to stagnation pressure over distance from the nozzle throat (measured along the wall) for chemical equilibrium, non-equilibrium and frozen flow in comparison to the measured pressure ratios can be seen in Fig. 6.9.

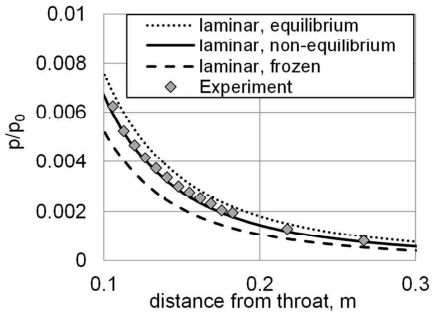


Fig. 6.9 Ratio of static to stagnation pressure over distance from nozzle throat for laminar flow simulation and experiment (condition 1)

In Fig. 6.10 the wall heat fluxes of the laminar solutions of these simulations in comparison to the measured wall heat fluxes are presented.

[7] The laminar simulation data including the chemical state of the flow was gained in the scope of the bachelor thesis of Wrede (see Appendix D)

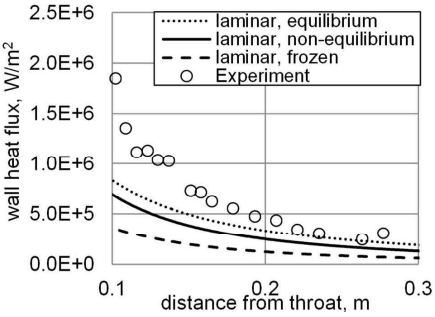


Fig. 6.10 Wall heat fluxes over distance from nozzle throat for laminar flow simulation and experiment (condition 1)

For both, pressure ratios and wall heat fluxes, the frozen solution represents the lowest and the equilibrium solution represents the highest values. As expected the solution of the non-equilibrium simulations is between these values. In comparison with the experimental data it can be seen that the measured pressure ratios fit well to the curve of the non-equilibrium solution, whereas the measured heat fluxes are much higher than the simulated laminar ones. Since the pressure ratios are, other than the wall heat fluxes, not sensitive to the character of the boundary layer this result may come from the wrong boundary layer behavior in the simulation. Therefore, the same simulations were conducted for a turbulent boundary layer. The resulting curves of pressure ratio and wall heat flux for the different chemical states can be seen in Fig. 6.11 and Fig. 6.12.

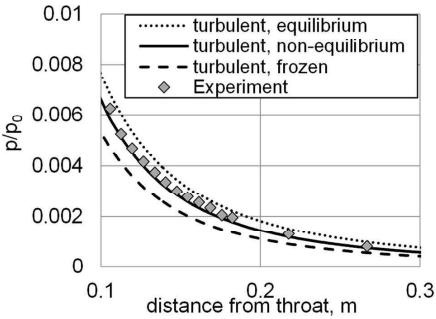


Fig. 6.11 Ratio of static to stagnation pressure over distance from nozzle throat for turbulent flow simulation and experiment (condition 1)

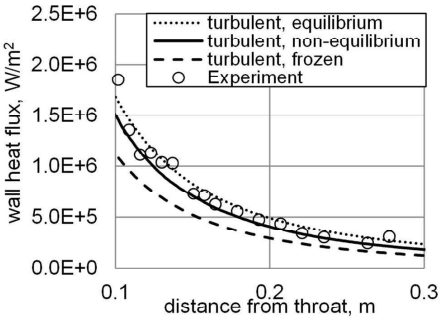


Fig. 6.12 Wall heat fluxes over distance from nozzle throat for turbulent flow simulation and experiment (condition 1)

In this case, the measured pressure ratios also fit to the curve of the non-equilibrium solution. Looking at the measured wall heat fluxes it can be seen that they fit to the calculated non-equilibrium curve as well. Thus, as already assumed in Sec. 6.2, the boundary layer in the expansion part of the conical nozzle seems to be turbulent. The calculated mass fractions of the different species for the non-equilibrium, turbulent flow are displayed by Fig. 6.13. As expected the main component of the flow is water with 80%. Its gradient indicates a frozen state of the flow close behind the nozzle throat. From the results of the numerical investigations it can be concluded that the hot gas flow of the conical nozzle matches the typical characteristics of a rocket nozzle flow, which are a turbulent boundary layer and a frozen chemical state downstream of the nozzle throat [43,60].

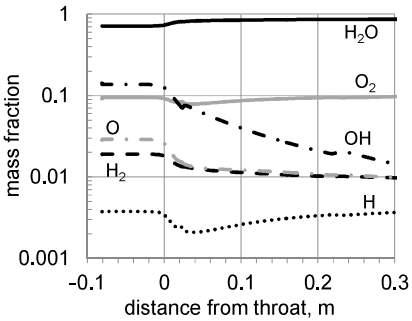


Fig. 6.13 Mass fractions of different species simulated for turbulent, non-equilibrium flow over nozzle center line, zero represents nozzle throat, condition 1

In addition, simulations for a turbulent, non-equilibrium flow were also conducted for the hot gas conditions 2 and 3. The resulting curves of the static pressure for all hot gas conditions in comparison to the experimental data are given in Fig. 6.14.

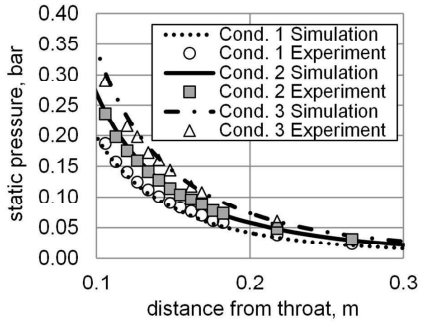


Fig. 6.14 Comparison of experimental and simulated static pressures over distance from nozzle throat (along the wall) for all three conditions (turbulent, non-equilibrium flow)

It can be seen that the measured static pressures fit well to the simulated curves. The same was done for the wall heat fluxes. Fig. 6.15 shows the simulated wall heat fluxes and the experimental values.

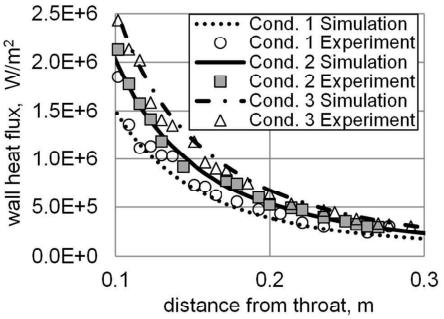


Fig. 6.15 Comparison of experimental and simulated wall heat fluxes over distance from nozzle throat (along the wall) for all three conditions (turbulent, non-equilibrium flow)

Also the experimental wall heat fluxes of all hot gas conditions fit well to the simulated data. Due to the good agreement of simulation and experiment, the simulations were further on used to determine the hot gas flow properties in the nozzle. In Fig. 6.16 the simulated Mach number of the flow

is plotted over the distance from the nozzle throat for hot gas condition 1. Since the nozzle geometry does not change and the differences in the boundary layer height between the different hot gas conditions are assumed to be small, this Mach number curve is valid for all three hot gas conditions.

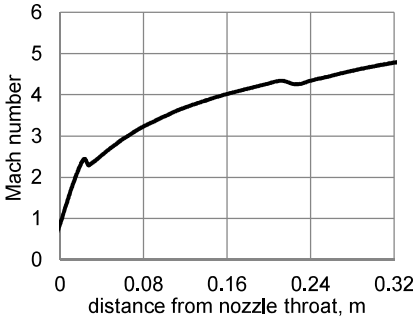


Fig. 6.16 Mach number over distance from nozzle throat (along the wall) exemplary for condition 1

The small jumps in the curve of the Mach number are due to the oblique shocks in the nozzle flow (see Fig. 6.8). These jumps can also be seen in the Reynolds number plots, which are displayed in Fig. 6.17. As expected the Reynolds number increases with increasing hot gas stagnation pressure. Each curve of the Reynolds number shows a maximum close behind the nozzle throat and declines than towards the nozzle's end. The starting point of the running length for the calculation of the Reynolds number was set in the nozzle throat.

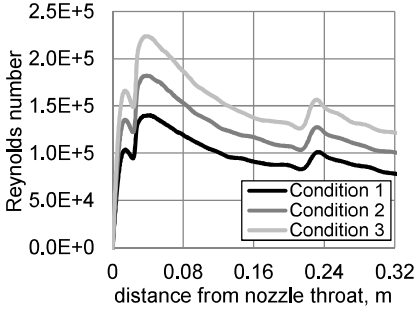


Fig. 6.17 Reynolds number of all three conditions. Running length along the nozzle wall starting in the nozzle throat

Fig. 6.18 shows the pressure gradient over the distance from the nozzle throat for conditions 1 and 3. Only these two conditions are shown to improve the legibility of the diagram. The pressure gradient of condition 2 is between the curves of the others. Due to the very high negative pressure gradient near the throat, the *x*-axis in Fig. 6.18 starts at the position of the injection slot for film cooling, so that the pressure gradient for the most relevant nozzle part for the experiments in this work becomes visible.

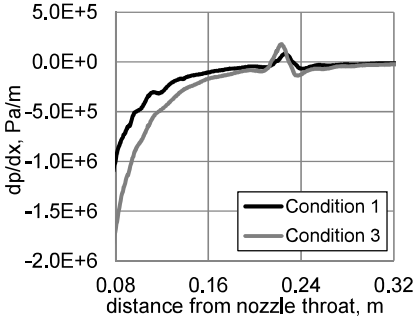


Fig. 6.18 Pressure gradient over axial distance from nozzle throat for conditions 1 and 3

In the first 0.1 m behind the injection slot (injection slot position $x \approx 0.084$ m) the negative pressure gradient decreases rapidly towards zero. In the last approx. 0.15 m of the nozzle the pressure gradient is very small as the expansion of the hot gas becomes weaker.

Also the boundary layer thickness ($u = 0.99u_\infty$) of the flow was derived from the numerical results. In Fig. 6.19 the boundary layer thicknesses of the simulated hot gas flows for condition 1 and condition 3 are shown. The boundary layer starts to grow in the nozzle throat and shows then an almost linear increase with increasing running length. For the hot gas condition with the higher stagnation pressure the boundary layer is slightly thinner due to the higher Reynolds number of the flow.

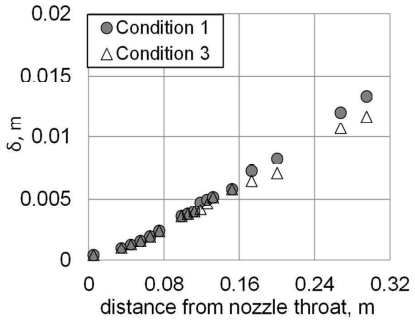


Fig. 6.19 Comparison of the simulated boundary layer thicknesses for conditions 1 and 3, distance measured along the nozzle wall

6.3.1 Dummy Gas[8]

Since simulations for non-equilibrium flow are very time-consuming, for further simulations (see Sec. 7.5) a dummy gas was defined. Fig. 6.13 shows that the composition of the hot gas is almost constant downstream the nozzle throat. Therefore, the composition of the dummy gas was defined as the hot gas composition, as gained from the simulations for non-equilibrium flow, at the position of the injection slot. The resulting gas can then be used to conduct simulations with frozen chemistry and provides satisfying results in the nozzle expansion part. A dummy gas was defined for every hot gas condition. The composition of the hot gas flow for condition 1 is given in Table 6.2 for Condition 2 and 3 see Appendix B.

[8]The first concept of the dummy gas was elaborated in the scope of the master thesis of Rottmann (see Appendix D)

Table 6.2 Components considered for the dummy gas of condition 1 and mass weighted molar mass of the dummy gas

Component	Molar mass, g/mol	Mass fraction	Mole fraction
H	1.00797	0.00251354	0.0407628
H_2	2.01594	0.0117624	0.0953766
H_2O	18.01534	0.842001	0.764004
O	15.9994	0.0123098	0.0125769
O_2	31.9988	0.0866698	0.0442751
OH	17.00737	0.0447437	0.0430051
Dummy gas	18.92643	1.0	1.0

For this gas composition 6th order temperature dependent polynomials for the heat capacity, heat conductivity and viscosity were derived. Therefore, first the heat capacity etc. of the single component was calculated using data from the NASA Glenn Research Center and Meija et al. [119,120]. Then, based on these results, the heat capacity etc. of the dummy gas was determined with Eqs. (3.59), (3.62) and (3.65) (see Sec. 3.2.6). Finally, the resulting data was fitted with a 6th order polynomial as shown by Eq. (6.3).

$$c_p(T), \mu(T), \lambda(T) = A_1 + A_2 T + A_3 T^2 + A_4 T^3 + A_5 T^4 + A_6 T^5 + A_7 T^6 \quad (6.3)$$

For condition 1 the coefficients of the polynomials are listed in Table 6.3.

Table 6.3 Coefficients for Eq. (6.3) for the condition 1 dummy gas. Data is valid for a temperature range of 200 K to 6000 K (c_p) and 300 K to 5000 K (μ and λ)

	A1	A2	A3	A4	A5	A6	A7
c_p(T), [J/kgK]	1.92 E+03	-6.43 E-02	8.98 E-04	-5.15 E-07	1.29 E-10	-1.56 E-14	7.32 E-19
μ(T), [Pas]	-7.96 E-07	3.54 E-08	1.11 E-11	-1.06 E-14	3.52 E-18	-5.41 E-22	3.21 E-26
λ(T), [W/mK]	3.25 E-03	7.10 E-05	7.99 E-08	-3.23 E-11	7.04 E-15	-8.23 E-19	4.01 E-23

The gas composition and the coefficients for the dummy gases of condition 2 and 3 are given in Appendix B. Using these polynomials and the assumption of a thermally perfect gas, the flow properties of the dummy gas were simulated.

7 Film Cooling in the Conical Nozzle

7.1 General Flow Conditions

For the experimental investigations of film cooling a coolant gas is injected tangentially to the conical nozzle wall through an injection slot (see Sec. 4.2) into the previous discussed hot gas flow. The hot gas Mach number at the injection position is 3.3 and remains almost unchanged for all presented hot gas conditions. The hot gas Reynolds number at this point is about $1.1 \cdot 10^5$ to $1.8 \cdot 10^5$ and increases with increasing hot gas stagnation pressure. Due to the constant geometry, pressure gradient and acceleration parameter remain almost unchanged for every experiment. The acceleration parameter $K = \frac{\eta}{\rho u^2}\frac{\partial u}{\partial x}$ [121] of the hot gas flow at the injection position is about $1.5 \cdot 10^{-6}$ for condition 1 and about $9.9 \cdot 10^{-7}$ for condition 3.

To determine the comparability between the experiments in the conical nozzle and a film cooling application in a real rocket nozzle extension, similarity parameters of film cooling are used. Table 7.1 shows these parameters for a full-scale nozzle and for injection of different coolants in the conical nozzle. There is a distinction between helium injection and other coolants, which are argon, nitrogen and carbon dioxide. This distinction is made because of the very different gas properties of helium compared to the other, much heavier coolant gases.

Table 7.1 Comparison of film cooling parameters in the conical nozzle for conditions 1-3 and those of a typical full-scale system [122]

Similarity parameter	Conical nozzle, helium	Conical nozzle, other coolants	Full-scale nozzle
Velocity ratio, u_c/u_{hg}	0.31-0.36	0.10-0.14	0.54
Mach number ratio, Ma_c/Ma_{hg}	0.55-0.61	0.51-0.61	0.55
Convective Mach number	1-1.5	2-2.5	0.71
Mass flow ratio, $\dot{m}_c/\dot{m}_{hg}$	0.004-0.034	0.02-0.1	0.033

It can be seen that the Mach number ratio and the mass flow ratio of the full-scale nozzle are matched by the experiments in the conical nozzle. However, the velocity ratio and the convective Mach number are not matched by the presented experiments, because the coolant gas used in a real nozzle is mainly hydrogen and with that an even lighter gas than helium. Since these two parameters are related to the shear layer growth [122] it can be assumed that the shear layer development in the following experiments differs from the real nozzle. It is also important to mention that the isothermal wall condition and the conical shape of the nozzle in these experiments present a huge deviation from parameters of a real rocket nozzle. Thus the results of the following experiments cannot be directly transferred to a real engine, but are rather able to point out important characteristics of film cooling behavior.

For getting reliable data it is important that the experiments with coolant injection are well reproducible. This mainly depends on the reproducibility of the hot gas flow, which was shown to be good (see Sec. 6.1) and the reproducibility of the coolant flow. The biggest issue for getting the same coolant flow conditions, with the same slot in the same hot gas condition, is the adjustment of the coolant stagnation pressure. Due to uncertainties of the coolant reservoir manometer slight deviations in the pressure of the coolant reservoir and with that in the coolant stagnation pressure cannot be prevented. However, as displayed by Fig. 7.1 these deviations in the coolant stagnation pressure have almost no influence on the measured wall heat fluxes. Therefore, the experiments with coolant injection are well reproducible.

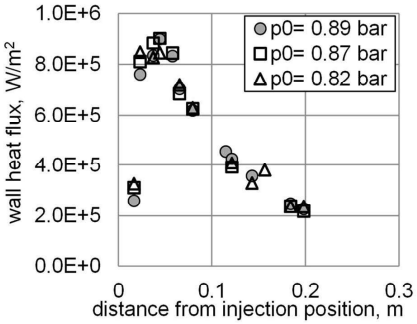


Fig. 7.1 Wall heat fluxes over distance from injection position for argon injection, condition 1

Since the injection of coolant in the nozzle increases the total mass flux through the nozzle the hot gas flow conditions in experiments with coolant injection are different than for experiments without injection. This is shown by an increase in static pressures with increasing coolant mass flux as displayed by Fig. 7.2.

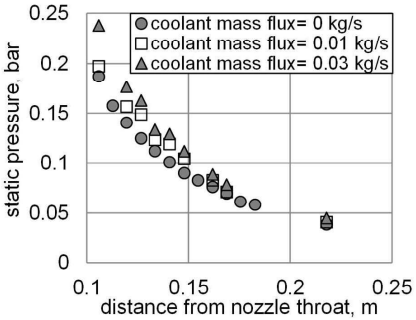


Fig. 7.2 Static pressure for the reference flow and with injection of two different coolant mass fluxes, condition 1

However, even for the highest coolant mass fluxes used in these investigations, the increase in the hot gas Mach number is not higher than 3%. Therefore, the influence of the coolant injection on the main flow is assumed to be negligible and the reference flow data can be used to evaluate the cooling efficiency in the following experiments.

7.2 Coolant Conditions

As already described in Sec. 4.2.1 the mass flux of the coolant is adjusted with a venturi nozzle and can be calculated with Eq. (4.1). For the determination of the coolant conditions at the injection slot exit not only this mass flux, but also the coolant pressure in the distributor ring of the nozzle must be known. This coolant pressure is the stagnation pressure of the slot flow and is measured during the experiment (see Fig. 7.3). The red dashed line marks the arrival of the hot gas flow in the nozzle. From this point on a quasi-constant coolant stagnation pressure can be observed during the following testing time.

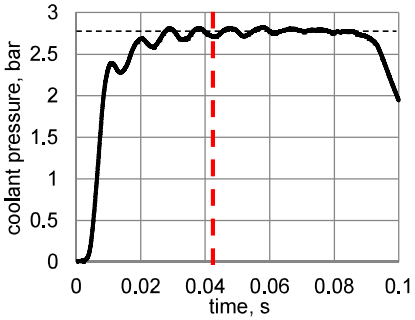


Fig. 7.3 Coolant pressure in distributor ring, red dashed-line marks the start of the hot gas flow in the nozzle

Using this pressure and the coolant mass flux, the coolant flow conditions can be determined. Since the slot heights are very small the influence of the coolant boundary layer on the coolant flow exit conditions is not negligible. Thus, the use of quasi-one-dimensional isentropic calculations provides huge uncertainties (see Fig. 7.4). Therefore, the exit conditions, such as Mach number, pressure etc. for the different slots are determined by a numerical simulation using ANSYS Fluent [117]. The stagnation temperature of the coolant is assumed to be the same as the nozzle wall temperature, due to the very small heights of the injection slots and the low coolant mass fluxes. This temperature and the measured coolant stagnation pressure are set as inlet conditions of the simulation. The simulated coolant mass flux has been determined by integrating the product of velocity and density across the slot cross section. For the conducted simulations the

deviation between the simulated coolant mass fluxes and the mass fluxes determined by the venturi nozzle calculation is less than 1%.

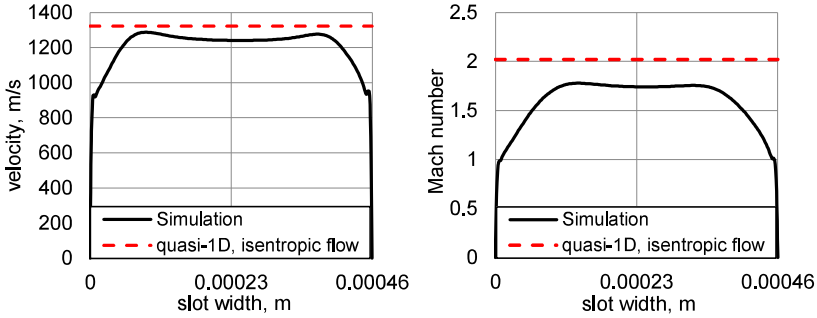


Fig. 7.4 Velocity (left) and Mach number (right) profile over slot width (s1) gained from simulations and quasi-1d, isentropic calculations

The resulting average exit velocities outside of the coolant boundary layer for every coolant gas and every slot height are shown in Table 7.2.

Table 7.2 Injection conditions of the coolants for all slot heights

	Helium	**Nitrogen**	**Argon**	**Carbon dioxide**
s1, u_c	1262 m/s	495 m/s	409 m/s	398 m/s
s2, u_c	1199 m/s	466 m/s	385 m/s	373 m/s
s3, u_c	1284 m/s	499 m/s	412 m/s	401 m/s
Blowing ratio for matched injection	1.01- 1.24	2.4-2.9	3.6-4.5	2.7-3.3

In the following experiments, helium is the lightest of all coolant gases and has therefore the highest injection velocity. The exit velocities of the other gases are about three times lower than for helium. Helium is injected with a low density and high velocity, whereas the other gases are injected with a high density and low velocity. Additionally, the range of blowing ratios needed for a matched coolant flow is given. A range is given because the needed blowing ratio depends on the slot height. The lowest value refers to injection through the smallest slot s2 and the highest value to injection through the largest slot s3. With a blowing ratio equal or higher than the given values strong shocks in the coolant flow, which would eventually increase the mixing of hot gas and coolant are prevented.

7.3 Parametric Study[9]

In the following, a parametric study on film cooling is conducted. The investigated influencing parameters were chosen from literature [7,20,66] and divided into three main categories. First, the injection conditions of the coolant, such as the coolant velocity and density, second the coolant gas properties, like the heat capacity and third the main flow properties at the point of injection e.g. the Reynolds number of the hot gas. By changing the experimental conditions, the influence of each of these categories on film cooling effectiveness was investigated within the conducted experimental studies. The parameters for altering the injection conditions were the injection slot geometry and coolant mass flux. For altering the main flow properties the stagnation conditions of the hot gas were changed. The coolant gas properties were changed by using different coolant gases, namely: helium, argon, nitrogen and carbon dioxide. By this, the influences of different parameters can be correlated to the measured effects in the wall heat fluxes.

7.3.1 Blowing Ratio

As first parameter of the injection conditions the influence of the blowing ratio (see Eq. (3.34)) was investigated. Therefore, helium was used as coolant and injected through slot s1 (s= 0.46 mm). The hot gas conditions were constant for every experiment. For varying the blowing ratio, the stagnation pressure of the coolant was adjusted. Therefore, with the blowing ratio also the coolant mass flux and the injection pressure of the coolant changed. Fig. 7.5 shows the resulting wall heat fluxes for different blowing ratios of helium and for the case of no coolant injection.

[9] Parts of the content of this subsection were already published in [69]

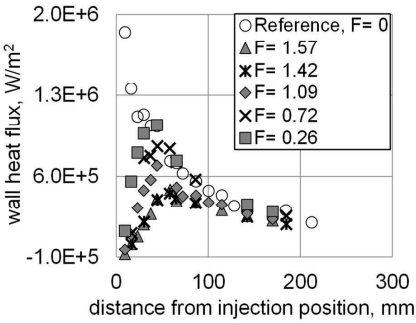


Fig. 7.5 Wall heat flux with and without helium injection ($p_{0,c}$=0.52-2.8 bar) and different blowing ratios (condition 1, s1)

The given distance from the injection point is measured along the nozzle wall. In the presented experiments, the two lowest blowing ratios result in an overexpanded, but still supersonic, coolant flow at the injection point, whereas the higher blowing ratios result in an underexpanded coolant flow. It can be seen that the interaction of coolant and hot gas as described in Sec. 3.2 is well represented by the heat flux distribution. When injecting a coolant, as in the present case tangentially to the nozzle wall, the distribution of the wall heat flux alters compared to that of the pure hot gas flow. The first measured heat flux values close to the injection position are almost zero, which indicates that the wall temperature and coolant temperature are almost the same. For high blowing ratios the first heat flux values are even below zero, since the wall temperature is higher than the local recovery temperature of the coolant. Further downstream, the heat flux increases as the coolant mixes with the hot gas. After a certain length the heat flux decreases again due to the expansion of flow. Even more downstream the heat flux matches the heat flux without injection indicating that from this point on the influence of the coolant injection becomes negligible and thermal loads at the wall are dominated by the hot gas flow again.

For lower blowing ratios the distance between the injection position and the point at which the cooling effect is vanished, is much shorter than for higher blowing ratios. In addition, the maximum in the wall heat fluxes is much higher for lower blowing ratios. Therefore, film cooling efficiency increases with increasing blowing ratio, which in this case is equal to increasing coolant mass flux. This correlation was already found in many film cooling studies and is often described in literature [123,7]. For the higher blowing

ratios also a better efficiency due to the underexpanded coolant flow is expected [19].

7.3.2 Slot Height

A change in the slot height results in a change of the film height of the injected coolant and for the presented experiments in a change of the coolant's injection pressure as well as Mach number. The slot height was changed by exchanging the inserts as described in Sec. 4.2.1. In the subsequent experiments helium was used as a coolant. For F= 1.05 and injection through the smallest slot s2 (s= 0.41 mm) the coolant flow was underexpanded ($\frac{p_c}{p_{matched}} = 1.37$) and injected with Ma= 1.57. For F= 1.06 and injection through the highest slot s3 (s= 0.56 mm, Ma_c= 1.73) the flow was also slightly underexpanded ($\frac{p_c}{p_{match}} = 1.1$) and for F= 0.79 and injection through s3 the flow was overexpanded ($\frac{p_c}{p_{matched}} = 0.85$). In the experiments with s2 and F= 1.05 and s3 and F= 0.79 the mass flux of the coolant was constant. The comparison of the heat fluxes can be observed in Fig. 7.6.

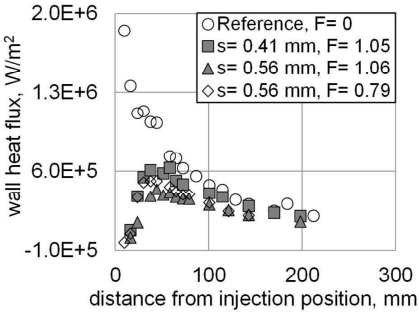


Fig. 7.6 Wall heat flux with and without helium injection for different slot heights (condition 1), Ma_c(s= 0.41 mm)= 1.57 and Ma_c(s= 0.56 mm)= 1.73)

For a constant blowing ratio the cooling effect is larger for the higher slot. Comparing s2, F= 1.05 and s3, F= 0.79 it can be seen that also for the same coolant mass flux the injection through the higher slot leads to an improved cooling. Thus, a better cooling efficiency is achieved for a higher coolant film. In addition, also the higher injection Mach number is assumed to have a positive influence on film cooling [4].

7.3.3 Hot Gas Condition

As next category, the influence of different hot gas conditions was investigated. Therefore, film cooling experiments with different stagnation pressures of hot gas (see Sec. 4.4) were conducted. The injection slot and coolant gas were the same for each experiment. Helium was used as coolant and injected through slot s2. To compare the results, the measured wall heat fluxes were converted to cooling efficiencies with Eq. (3.52) neglecting the ratio of the heat transfer coefficients. For the results displayed by Fig. 7.7 the injected mass flux of the coolant was constant. This leads to a decreasing blowing ratio with increasing hot gas stagnation pressure.

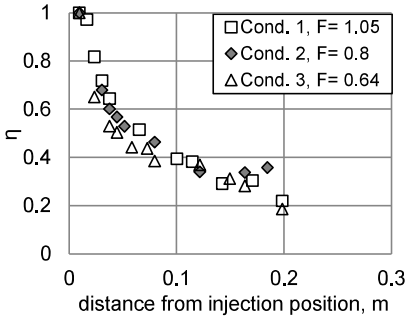


Fig. 7.7 Cooling efficiency of helium with the same coolant mass flux and injection in different hot gas conditions (s2)

It can be seen, that with decreasing blowing ratio also the cooling efficiencies are slightly decreasing. Changing the blowing ratio by altering the hot gas condition seems to have the same effect as changing the blowing ratio by altering the coolant mass flux, as done in Sec. 7.3.1.

In the next set of experiments, the coolant mass flux was adjusted for each hot gas condition, such that the blowing ratio was constant. The resulting curves of the cooling efficiencies can be seen in Fig. 7.8. For this case, the curves of the cooling efficiencies are almost identical. Far downstream of the injection position the cooling efficiencies of condition 2 and 3 are slightly higher than the cooling efficiency of condition 1. This may result from the increased hot gas Reynolds number for the higher conditions [124–126]. In contrast to the positive influence of the higher Reynolds number on the cooling efficiency is the fact that the acceleration parameter of the hot gas flow decreases from condition 1 to 3 by about 50%. Several authors found

for a decreasing acceleration parameter a decreasing cooling efficiency [32,31]. This shows that in the presented experiments contrary parameters are influencing the film cooling efficiency. The separate influences of these parameters cannot be extracted with the presented experimental setup. However, the experimental results imply that these effects almost neutralize each other, such that the influence of the higher hot gas stagnation conditions on film cooling seems, at least for the current setup, negligible.

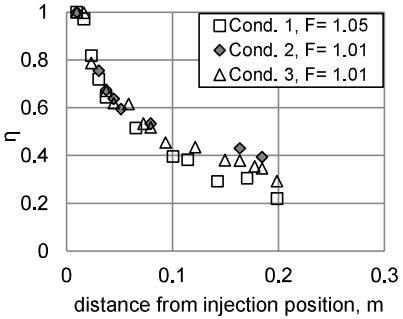


Fig. 7.8 Cooling efficiency of helium with the same blowing ratio and injection in different hot gas conditions (s2)

This result is supported by a study of Arnold et al. [123], in which the influence of the hot gas stagnation pressure on film cooling efficiency was also found to be negligible.

7.3.4 Coolant Gas

For investigation of the influence of the coolant gas properties on film cooling efficiency, different gases were used as coolant. The chosen gases were helium, nitrogen, argon and carbon dioxide. For the injection properties of each of these gases see Table 7.3.

Table 7.3 Gas properties at the injection position in the coolant gas core flow for condition 1 and slot s2, coolant gas properties from [127], coolant velocity, density, temperature and hot gas data from simulation. Coolant stagnation pressures (top-down) 2.67 bar, 2.2 bar, 1.67 bar, 1.6 bar, coolant stagnation temperature for all gases T_0= 330 K

	Molar mass, g/mol	c_p, J/gK	u, m/s	ρ, kg/m^3	T, K	μ, Pas [10^{-5}]	Pr
Helium	4	5.193	1199	0.141	168	1.35	0.66
Nitrogen	28	1.041	466	0.813	195	1.26	0.72
Argon	39.95	0.522	385	1.027	150	1.22	0.67
Carbon dioxide	44	0.762	373	0.884	216	1.08	0.77
Hot gas	18	2.897	3775	0.026	2140	6.12	0.56

All gases were injected through the smallest slot s2. The blowing ratios were chosen such that the coolant flow was underexpanded for all gases. By this, the influence of flow effects, like strong shocks in the coolant flow, on the experimental results was prevented. Due to the high molar masses of nitrogen, argon and carbon dioxide the adjusted blowing ratios for these gases were almost the same. Helium, with a much lower molar mass than the other coolant gases, was injected with a blowing ratio which was about 50% lower. The injection Mach numbers of the coolants were Ma= 1.57-1.63. The changes in the coolant Mach number are therefore neglected. The resulting wall heat fluxes are plotted in Fig. 7.9.

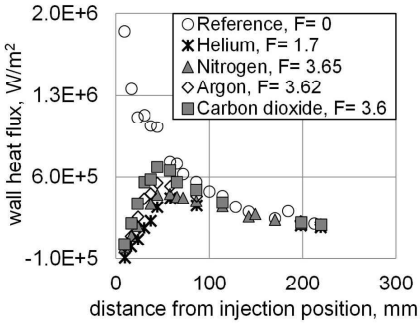


Fig. 7.9 Wall heat flux for injection of different coolant gases in comparison to the wall heat flux without injection (condition 1, Ma_c= 1.57- 1.63 and s2)

Although helium was injected with the lowest blowing ratio it has the best cooling effect of all gases. Among the heavier coolant gases, nitrogen is the most efficient and carbon dioxide the less efficient. Comparing this order to the coolant gas properties listed in Table 7.3, it can be seen that the gases with the highest heat capacities are the best coolants. This effect is explained by the fact that a gas with a higher heat capacity can store more heat before changing its temperature and was also found by several other authors [6,24]. In addition, also a lower molar mass of the coolant gas seems to increase the cooling efficiency. This may be explained by the correlation of molar mass and specific volume of the gas. A lower molar mass results in a higher specific volume. Thus, the volume flow increases, which results in a thicker coolant film at the wall [128]. A lower molar mass also results in a higher injection velocity of the coolant [43]. For injection into a turbulent boundary layer flow this higher injection velocity is assumed to have a stabilizing effect on the coolant film.

Considering the densities and velocities as given in Table 7.3 and calculating the ratios of density ρ_c/ρ_∞ and velocity u_c/u_∞ of the coolant to the hot gas at the point of injection, it can be seen that ρ_c/ρ_∞ and u_c/u_∞ get closer to one with increasing cooling efficiency of the coolant gas. From shear layer theory (see Sec. 3.2.2) the best cooling efficiency is assumed for $\rho_c/\rho_\infty = u_c/u_\infty = 1$, because large density and velocity changes from coolant to hot gas increase the mixing in the turbulent shear layer [65].

Consequently, the experimental results indicate that film cooling efficiency of foreign gas injection depends strongly on the properties of the coolant gas.

7.4 Evaluation of Influencing Parameters[10]

The evaluation of the parametric study resulted in the in Table 7.4 displayed set of influencing parameters on film cooling efficiency in the presented experimental setup. It has to be mentioned that these parameters are not independent of each other. For example, a change in the slot height will, for the presented setup, also result in a change in the coolant Mach number and injection pressure. Therefore, for further investigations it is important to consider the interaction of different parameters rather than the influence of a single parameter.

Table 7.4 Influence of different parameters on film cooling efficiency when each parameter increases

Parameter	Cooling Efficiency
Blowing ratio	increases
Slot height	increases
Mach number coolant	increases
Heat capacity coolant	increases
Prandtl number coolant	decreases
Molar mass coolant	decreases
Injection pressure coolant	increases
Distance from slot	decreases

For film cooling applications, the cooling performance increases, when the local wall heat flux of the hot gas-coolant mixture in the nozzle wall decreases. Thereby, the heat input into the wall depends on the local thermophysical properties of the gas mixture at the wall and on the flow parameters of this mixture. The maximum local wall temperature that can be reached is that of an adiabatic wall and is for the current case described by the recovery temperature (see Eq. (3.17)). For constant hot gas conditions ($T_{r,hg} = const.$) and constant coolant stagnation temperature ($T_{0,c} = const.$) the cooling efficiency (see Eq. (3.49)) increases when the recovery temperature of the gas mixture ($T_{aw,c}$) decreases. The recovery temperature is a function of the static temperature of the gas mixture, the recovery factor

[10] Parts of the content of this subsection were already published in [129]

of the mixture, which is a function of the Prandtl number, the isentropic exponent of the mixture and the Mach number of the mixture. All these parameters are now correlated to the experimental results as given in Table 7.4. Assuming constant hot gas conditions, the mixture properties are only a function of the coolant injection conditions and the kind of coolant gas. When additionally keeping the injection slot and the coolant gas constant, as it was done in Sec. 7.3.1, the recovery temperature depends only on the local static temperature of the mixture. Using Eq. (3.60) for calculating the mixture temperature it can be seen that in this case the mixture temperature decreases when the coolant mass flux increases. A lower mixture temperature results in a lower recovery temperature and a better cooling performance. Since for the experiments in Sec. 7.3.1 a higher coolant mass flux was equal to a higher blowing ratio, the influence of the blowing ratio, as seen in the experimental results, can be confirmed.

Considering now the case of changing slot heights, but constant coolant mass flux, as in Sec. 7.3.2, the injection conditions, such as Mach number and static pressure of the coolant flow, change. When the slot height is increased, the injection Mach number increases. For the same coolant gas a higher injection Mach number indicates a lower static temperature and a higher injection velocity of the coolant. Following Eqs. (3.58) and (3.60) the higher coolant velocity results in a higher mixture velocity and a lower static temperature of the coolant lowers the static temperature of the gas mixture. Using Eq. (3.69) for the mixture Mach number it can be seen that for the same coolant gas and constant coolant mass flux this higher mixture velocity and lower mixture temperature, resulting from the higher injection Mach number, increase the mixture Mach number. Rewriting Eq. (3.17) with the isentropic correlation of the static temperature and Mach number

$$T_r = \frac{T_{0,m}}{1 + \frac{\gamma - 1}{2} {Ma_m}^2} \left(1 + r \frac{\gamma - 1}{2} {Ma_m}^2\right), \tag{7.1}$$

it follows that for a constant coolant and hot gas stagnation temperature and a recovery factor less than one the increase in the mixture Mach number causes a decrease in the recovery temperature.

If the coolant gas is changed as in Sec. 7.3.4, all parameters in the recovery temperature change, too. Assuming the hot gas condition and coolant mass flux to be constant, the focus is now set on the influence of the thermophysical properties of the gas. Since the Prandtl numbers of the coolants and the hot gas are less than one, the resulting recovery factor is

also less than one. Resulting from Eq. (7.1), for a gas mixture with a recovery factor less than one, a low recovery temperature is reached for a low mixture total temperature, a high mixture Mach number and a high isentropic exponent of the mixture.

For constant coolant temperature and constant coolant mass flux the mixture temperature decreases with increasing heat capacity of the coolant (see Eq. (3.60)).

In general, a high mixture Mach number is achieved for a high mixture velocity and a low speed of sound of the mixture. According to Eq. (3.58) for constant hot gas conditions and constant coolant mass flux an increasing injection velocity of the coolant increases the mixture velocity. Assuming that the backpressure at the injection point is fixed, as it is set by the hot gas flow, the main influencing parameter on the velocity for given coolant total temperature is the molar mass of the gas. The injection velocity increases with decreasing molar mass of the coolant. Following the conservation of energy, a higher injection velocity results in a lower static temperature of the coolant and with this (as already discussed) in a lower static temperature of the mixture. The influence of the coolant's static temperature on the mixture temperature is increased with an increasing heat capacity of the coolant. This lower static temperature of the mixture decreases the speed of sound of the mixture. However, a decreasing molar mass of the coolant increases the mixture's speed of sound, so for a decrease in the speed of sound this effect must be overweighed by the temperature decrease. The speed of sound is also affected by the isentropic exponent. The influence of this parameter was not clearly visible in the experiments. However, due to the interaction of isentropic exponent, molar mass and heat capacity its influence is already indirectly included in the other parameters.

This discussion shows that the experimental observations as given in Table 7.4 can be well correlated to the local recovery temperature of the mixture and therefore to the cooling efficiency. The only observations, which are not directly correlated to the recovery temperature, are that for all other parameter in Table 7.4 constant, film cooling efficiency increases with increasing coolant injection pressure and decreasing distance from the injection point. These parameters influence the mixing of hot gas and coolant, which increases with decreasing injection pressures, due to shocks in the coolant flow and other effects and with increasing distance from the injection point due to friction and turbulence.

7.4.1 Characteristic Numbers of Film Cooling

To compare the results of different experiments, the total cooling efficiency of each experiment is calculated. For determination of the total cooling efficiency, the curve of the wall heat flux $\dot{q}(x)$ is integrated over the nozzle's surface area, which depends on the local radius *r(x)* and the distance from the injection position *x*. By Eq. (7.2)

$$\int_0^{2\pi}\int_{x_1}^{x_2} \dot{q}(x) r(x) dx\, d\varphi = Q \tag{7.2}$$

the total amount of heat *Q* transferred to the nozzle wall in *Watt* can be determined. Calculating this value for the reference heat flux Q_{ref} as well as for the heat flux with coolant injection Q_c the total cooling efficiency $\bar{\eta}$ can be determined as

$$\bar{\eta} = \frac{Q_{ref} - Q_c}{Q_{ref}}. \tag{7.3}$$

The total cooling efficiency has values between 0 and 1, where 0 indicates no cooling and 1 indicates perfect cooling.

7.4.1.1 Convective Mach Number

The convective Mach number (see Eq. (3.28)) has a huge influence on the growing rate of a shear layer. As described in Sec. 3.2.1 a shear layer containing hot gas and coolant starts to grow directly behind the injection slot. After a certain distance from the injection point the shear layer reaches the wall and breaks the pure coolant film up. At this point ends the region of pure coolant film and the heat transfer at the wall is influenced by the local mixture of hot gas and coolant. Also the cooling efficiency starts to decrease from that point on. So the position of the film breaking point depends on the growth rate of the shear layer. A decreasing growing rate would lead to a shifting of the film breaking point to a further downstream position and therefore to an increase of the region with maximum cooling efficiency. As already described in Sec. 3.2.2 the shear layer growing rate decreases with increasing convective Mach number, so experiments with a higher convective Mach number at the injection position should show a weaker growing of the shear layer and therefore a longer region of pure coolant film

at the wall, which results in a higher total cooling efficiency. Fig. 7.10 shows the total cooling efficiency plotted over the convective Mach number at the injection position for various experiments using helium as coolant. It can be seen that there is no obvious correlation between convective Mach number and cooling efficiency for the presented experiments. Therefore, it is assumed that an eventually increase in the potential core region is negligible small and has no measurable influence on the overall cooling efficiency. It has to be mentioned that a final judgment of the influence of the convective Mach number is difficult, because for the experiments shown in Fig. 7.10 other parameter e.g. the blowing ratio also change with the convective Mach number. However, following these results and considering the small slot heights and relative to those large boundary layer heights of the hot gas, it is assumed that the potential core region can be neglected in the presented experiments. From that follows that the most dominant region for film cooling in the presented setup is the boundary layer region downstream of the film breaking point, which depends on the local mixture of hot gas and coolant at the wall.

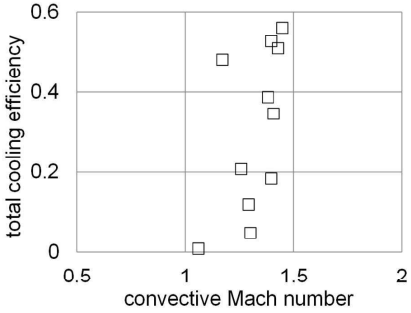


Fig. 7.10 Total cooling efficiency of different experiments with helium injection over convective Mach number for different hot gas conditions and injection slots

7.4.1.2 Blowing Ratio

A very common characteristic number for film cooling is the blowing ratio (see Eq. (3.34)). In the previous parametric study its influence on the cooling efficiency was already shown. However, the question is if this parameter is also valid for a more common evaluation of film cooling. In Fig. 7.11 the total cooling efficiency is plotted over the blowing ratio for several film cooling

experiments using different gases as coolant. It can be seen that for all coolant gases the cooling efficiency increases with increasing blowing ratio. However, when comparing different gases, for example helium, argon and nitrogen, with the same blowing ratio (F= 1.6) in Fig. 7.11, the affiliated cooling efficiencies differ strongly. The difference in the cooling efficiency of helium and argon is more than 70 %. The same albeit minor effect can be observed when comparing nitrogen and carbon dioxide with both F= 3.6. Thus, only the blowing ratio is not suitable for correlating experiments with different coolant gases, since in this case differences in other influencing parameter e.g. the Mach and Reynolds number of the coolant seem to be more dominant than the blowing ratio.

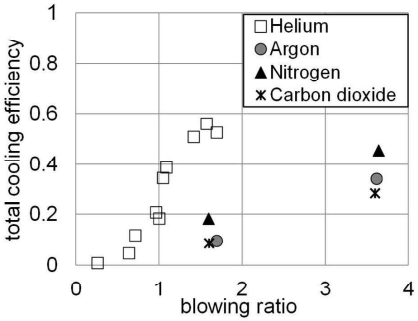


Fig. 7.11 Total cooling efficiency over blowing ratio for injection of different coolant gases through different slots in different hot gas conditions

7.4.1.3 Momentum Flux Ratio

Another characteristic number of film cooling is the momentum flux ratio. This ratio can be written as the blowing ratio enhanced by the ratio of the velocities of coolant and hot gas at the injection position,

$$I = \frac{(\rho u^2)_c}{(\rho u^2)_{hg}} = F \frac{u_c}{u_{hg}}. \tag{7.4}$$

With a higher momentum flux of the coolant, the coolant flow is assumed to be more insensitive to disturbances, so a higher momentum flux ratio should result in a better cooling efficiency. In Fig. 7.12 the total cooling efficiencies

of experiments with different gases are plotted over the momentum flux ratios. As predicted, the cooling efficiency increases with increasing momentum flux ratio. In all presented experiments the coolant was injected at lower velocities as the hot gas velocity at the injection position. Since the experimental data plotted in Fig. 7.11 and Fig. 7.12 are the same, a comparison of these figures shows that helium reaches even with lower blowing ratios much higher momentum flux ratios and therewith much higher cooling efficiencies, than the other coolant gases. This is due to the very different injection velocities of the different coolants (1200 m/s for helium, 300-400 m/s for the other gases), which result from differences in the molar masses. Another observation when comparing Fig. 7.11 and Fig. 7.12 is, that other than the blowing ratio, the momentum flux ratio leads to a good and coolant gas independent correlation of all experiments. It can be concluded that the momentum flux ratio is much more dominant than other influencing parameters and allows for the presented experiments a generally valid evaluation of the cooling efficiency.

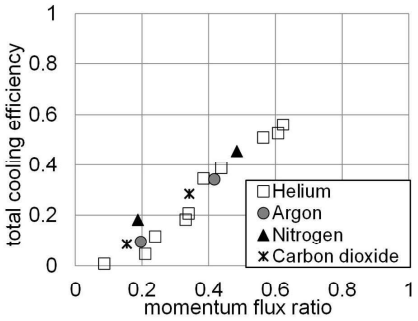


Fig. 7.12 Total cooling efficiency over momentum flux ratio for injection of different coolant gases through different slots in different hot gas conditions

7.5 Numerical Investigations

For a better understanding of certain flow phenomena RANS simulations with coolant injection were conducted. As turbulence model the k-ε model was used, because in different studies it was shown that this model fits best to film cooling data [130,131]. As hot gas flow in the nozzle the dummy gas (see Sec. 6.3.1) was used. It was assumed that the hot gas is chemically frozen starting directly at the nozzle inlet. The nozzle walls were isothermal with the wall temperature depending on the simulated hot gas condition. This wall temperature was also set as the coolant stagnation temperature. Temperature dependent polynomials for the heat capacity, heat conductivity and viscosity of the coolant gases were used (see Eq. 6.3). All results are grid-convergent solutions. Fig. 7.13 compares the numerical results with experimental data. It can be seen that experimental and numerical results are very similar.

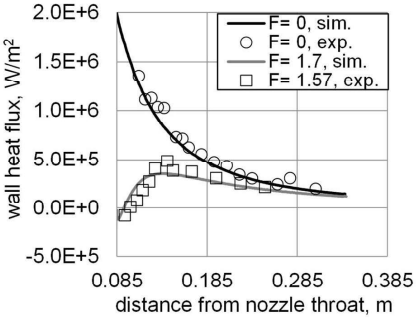


Fig. 7.13 Comparison of simulated and measured wall heat fluxes with and without helium injection, condition 1, s1

However, especially close behind the injection slot, where a shear layer of hot gas and coolant forms, deviations between simulation and experiment are to expect, i.a. due to the RANS nature of the simulations.

7.5.1 Hot Gas-Coolant Flow Field at Injection Position

For investigation of the flow field at the position of the injection slot, pressure and streamline plots at this point were taken from simulations with coolant injection. For an underexpanded helium injection through slot s1 the plots can be seen in Fig. 7.14.

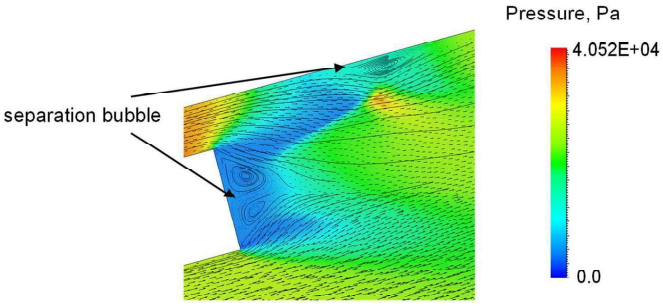


Fig. 7.14 Pressure and streamline distributions of hot gas and coolant (helium, p_0= 1.5 bar) at the injection position from ANSYS Fluent simulations, condition 1, s1

The flow direction of hot gas and coolant is from the left to the right. The hot gas flows at the lower side of the figure, whereas the coolant is injected at the upper side. Just behind the injection slot an expansion of the coolant due to the underexpanded injection can be seen. Also two separation bubbles are visible in this figure. One at the tip of the splitter plate and one at the wall in the coolant flow. For the considered splitter thickness of 1 mm the deflection of the hot gas flow due to the expansion is not enough to prevent a flow separation at the tip of the splitter plate. At the upper end of this separation bubble a recompression shock caused by the strong expansion of the coolant flow can be seen. As this shock reaches the boundary layer at the nozzle wall it causes a local pressure increase at the wall and a separation of the coolant flow. Such a separation due to shock-coolant interaction can also occur for overexpanded coolant flow (see Fig. 3.6).

A study by Grin and Zakharov [132] indicated that this separation bubble depends on the molecular weight and momentum flux of the injected coolant. Thus light coolant gases with low blowing ratios, as typically used in film cooling applications, are especially at risk for separation, when interacting with an incident shock. Olsen et al. [133] found that the strength of the recompression shock grows with increasing splitter thickness. A smaller thickness, or most ideally a sharp edge as tip of the splitter plate and a coolant injection pressure equal to the local hot gas pressure is best to prevent separation. However, the splitter plate has to withstand high thermal and mechanical loads, which limits the design options. In addition, studies in literature with splitter thicknesses much larger than the one used

in the presented experiments showed no significant influence of the separation bubble on film cooling [133].

7.5.2 Influence of Heat Transfer Coefficient on Cooling Efficiency

As shown in Sec. 3.2.5 for calculation of the cooling efficiency from experimental data often a simplified method, assuming the heat transfer coefficient of pure hot gas flow and coolant-hot gas mixture to be equal, is used. To check if and in which range this assumption is valid different simulations with coolant injection were conducted. First, simulations with helium injection at a low and a high blowing ratio were performed. The resulting cooling efficiencies for the simplified case (approximation in Eq. (3.52)) and the real case (Eq. (3.52) with $\alpha_{nc}/\alpha_c \neq 1$) are shown by Fig. 7.15. It can be seen, that independent of the blowing ratio, the cooling efficiencies are much higher for the calculations taking into account the heat transfer coefficients than for the ones neglecting the heat transfer coefficients. However, the position of the curves of low and high blowing ratio relative to each other remains the same no matter which equation is used [11].

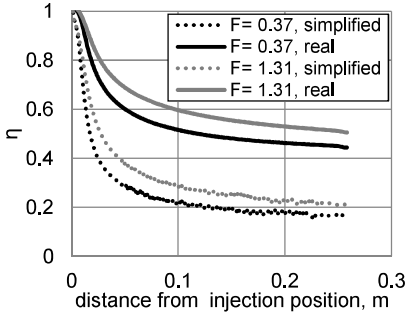


Fig. 7.15 Cooling efficiency for helium injection in hot gas C1, s1

As next step, simulations with injection of different coolant gases were performed. The coolant gases were chosen from the experiments and complemented by hydrogen, which was not used in the experiments, but is

[11] The first simulations with coolant injection and investigation of the influence of the heat transfer coefficient ratio on the cooling efficiencies of helium were conducted in the scope of the master thesis of Rottmann (see Appendix D)

the most popular coolant in real film cooling applications. For the case of neglecting the heat transfer coefficients the cooling efficiencies gained in the simulations are displayed by Fig. 7.16.

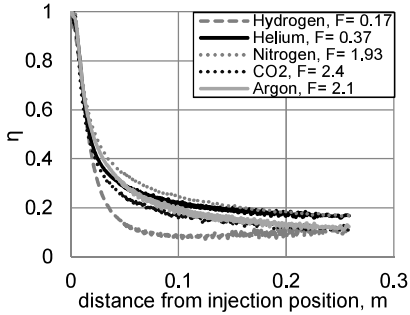


Fig. 7.16 Simplified cooling efficiency for injection of different coolants in hot gas C1, s1

When using Eq. (3.52) with $\alpha_{nc}/\alpha_c \neq 1$ the curves of the cooling efficiencies change as can be seen in Fig. 7.17.

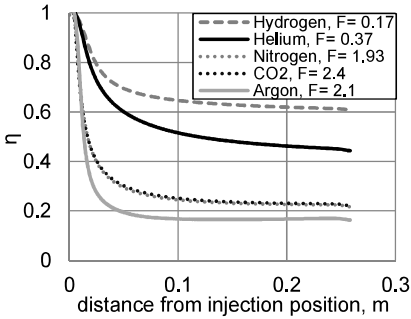


Fig. 7.17 Cooling efficiency taking into account the heat transfer coefficients for injection of different coolants in hot gas condition 1, s1

Comparing Fig. 7.16 and Fig. 7.17, for hydrogen and helium a strong and for carbon dioxide a slight increase in the cooling efficiencies can be seen. The cooling efficiencies of argon decrease and the ones of nitrogen stay almost the same. This effect results in a shift of the positions of the curves relative to each other. For example, in Fig. 7.16 hydrogen shows the smallest cooling efficiency, whereas in Fig. 7.17 it shows the best. Also the order of the efficiencies of the other gases varies strongly. Thus, the

negligence of the heat transfer coefficients in the calculation of the cooling efficiencies can result in huge deviations from the real cooling behavior and therefore in unusable data. The injection of a coolant, even at low bowing ratios seems to have a dominant influence on the local heat transfer coefficient, especially for light gases like hydrogen and helium, which are of special interest for film cooling applications. Hence, from the numerical results it can be concluded that for the considered conditions the ratio of the heat transfer coefficients cannot be neglected when determining the cooling efficiency. It should be mentioned that due to the complexity of the flow field, the quantitative data of the numerical simulations shown in Fig. 7.15 to Fig. 7.17 is not absolutely reliable. However, the qualitative behavior is well captured.

To consider this result in the following evaluation of the experimental data, a simplified model for the ratio of the heat transfer coefficients was developed in Sec. 3.2.6. For validation of this model the ratios of the heat transfer coefficients, as calculated with Eq. (3.53), are plotted in Fig. 7.18.

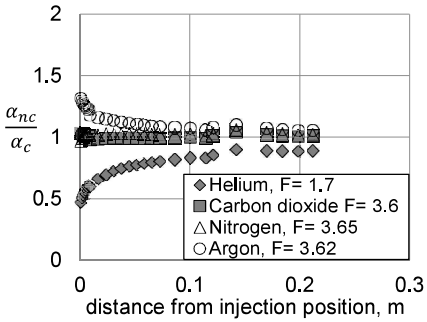


Fig. 7.18 Ratio of heat transfer coefficients (see Eq. (3.53)) for different coolant gases

Following Eq. (3.52), $\alpha_{nc}/\alpha_c < 1$ results in an increase in η and vice versa. It can be seen that the calculated values show the same effect as observed in the simulations. When using the values as given in Fig. 7.18 the cooling efficiencies of helium increase and the ones of argon decrease. The cooling efficiencies of nitrogen and carbon dioxide are nearly unaffected. Therefore, this model is further assumed to give a good estimation of the ratio of the heat transfer coefficients when calculating the cooling efficiencies from experimental data.

7.6 Correlation[12]

In the following, the newly developed models for film cooling, as presented in Sec. 3.2, are tested on the experimental data. In addition, their effect on the correlation of the data in comparison to models from literature is discussed. For an easier examination, the values are plotted in a log-log diagram. The correlation of the data using the literature models for the cooling efficiency and correlation factor is plotted in Fig. 7.19.

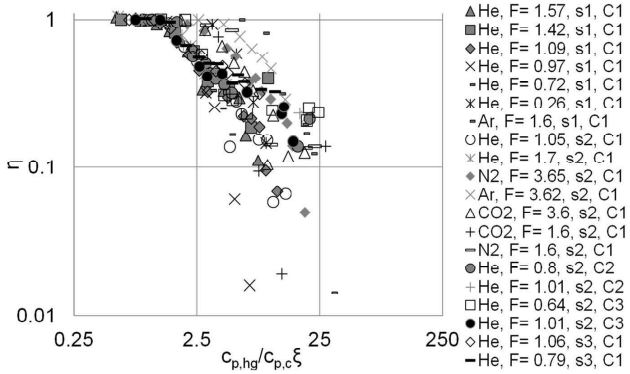


Fig. 7.19 Correlation of the experimental data using the simplified calculation of the film cooling efficiency (Eq. (3.52) with $\alpha_{nc}/\alpha_c = 1$) and the correlation factor by Goldstein (Eq. (3.35)) enhanced by the ratio of the heat capacities

It can be seen that the correlation of the data is quite weak. Especially between the data for different gases a deviation starting directly at $\eta = 1$ is visible. Therefore, in Fig. 7.20 the same set of data is plotted over the same correlation factor, but with the cooling efficiencies taking into account the heat transfer coefficients calculated with the mixing model as presented in Sec. 3.2.6. Two effects are visible in this diagram. First, the total values of the cooling efficiencies change when using the heat transfer coefficients in the calculations and second the differences between the data for different gases become much smaller. These effects can be explained by the results of the numerical investigations of the heat transfer coefficients (see Sec. 7.5.2). It demonstrates again the importance of the heat transfer coefficients in Eq. (3.52), especially when comparing different coolant gases.

[12] Parts of the content of this subsection were already published in [69] and in [134]

Additionally to the enhanced model for the film cooling efficiency, also the influence of the axisymmetric enhancement of the Goldstein model (Eq. (3.47)) is tested in Fig. 7.21. The resulting plot shows that the effect of using the axisymmetric instead of the flat plate correlation factor on the quality of the correlation of the data is minor. Only small deviations in the gradients of the curves can be seen when comparing Fig. 7.20 and Fig. 7.21. Both plots show a well-fitting correlation of the experimental data.

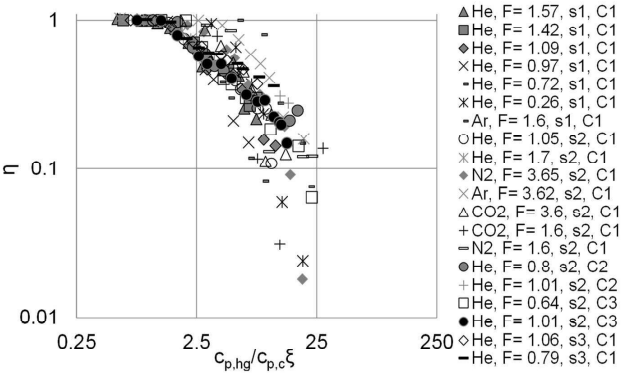


Fig. 7.20 Correlation of the experimental data using Eq. (3.52) for the film cooling efficiency together with the model for the heat transfer coefficients (see Eq. (3.53)) and the correlation factor by Goldstein (Eq. (3.35)) enhanced by the ratio of the heat capacities

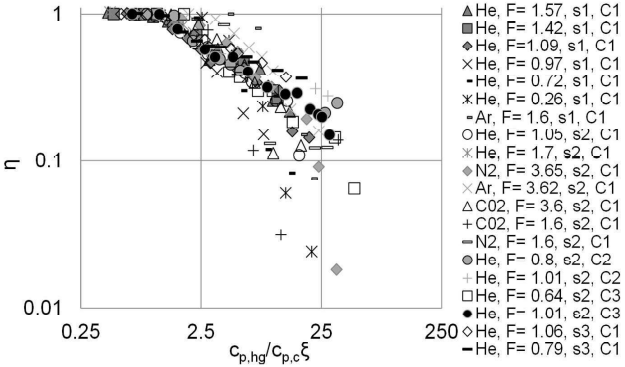


Fig. 7.21 Correlation of the experimental data using Eq. (3.52) for the film cooling efficiency together with the model for the heat transfer coefficients (see Eq. (3.53)) and the correlation factor for axisymmetric flow (Eq. (3.48)) enhanced by the ratio of the heat capacities

In conclusion it can be said that the axisymmetric extension of the Goldstein model and the use of the heat transfer model for the film cooling efficiencies allow a satisfying correlation of the presented experiments with variation of all three main influencing parameter categories of film cooling, which were defined as the injection conditions of the coolant, the main flow properties and the coolant properties. Only minor deviations in the correlations can be seen, which may result from measurement uncertainties in the wall heat fluxes (especially for low wall heat fluxes) and in the blowing ratio, errors in the fluid properties and of course the simplifications in the models themselves. However, the strongest deviations in the correlations are for values of $\eta < 0.1$ and with that of no technical relevance for a real film cooling application.

Due to the results in Sec. 7.4.1.3 also a much simpler correlation is tested, which consists only of the ratio of downstream distance from the injection point *x* to slot height *s* multiplied with the inverse of the momentum ratio *I*. The resulting correlation of the experimental data is displayed by Fig. 7.22.

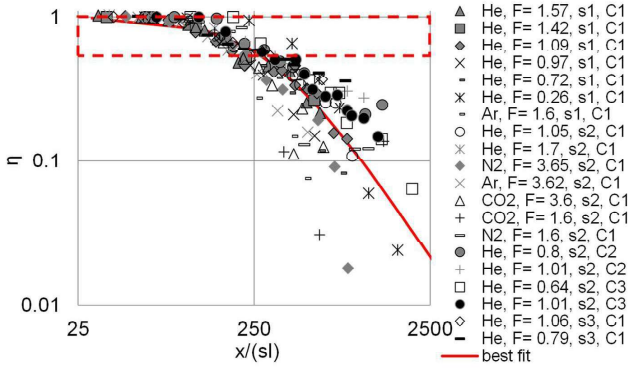


Fig. 7.22 Correlation of the experimental data using Eq. (3.52) for the film cooling efficiency together with the model for the heat transfer coefficients (see Eq. (3.53)) and a simple correlation factor. The dashed box marks the range of cooling efficiencies, which are of technical relevance

It can be seen that this simple approach leads also to a satisfying correlation of the data. For an overall statement of the results a best-fit curve for all experiments was determined. It can be described by

$$\eta = \frac{1}{1 + 3.5366 \cdot 10^{-5} \left(\frac{x}{sI}\right)^{1.7966}} = \frac{(T_r - T_{aw,c})}{(T_r - T_{0,c})}. \tag{7.5}$$

The same was done for the correlation using the enhanced Goldstein model, as can be seen in Fig. 7.23, with a best-fit curve given by Eq. (7.6), where ξ is calculated by Eq. (3.48). It is valid for $T_{0,c} = T_w$.

$$\eta = \frac{1}{1 + 0.1101\left(\frac{c_{p,hg}}{c_{p,c}}\xi\right)^{1.3934}} = \frac{(T_r - T_{aw,c})}{(T_r - T_{0,c})} \tag{7.6}$$

By using Eq. (3.49) also the range of the technical relevant cooling efficiencies was calculated and is marked in Fig. 7.22 and Fig. 7.23 by the red-dashed boxes. For this, the average recovery temperature of the hot gas flow and the coolant stagnation temperature were used. As a maximum of the adiabatic wall temperature a temperature of T= 1400 K was set (see Sec. 2). This maximum wall temperature is reached for η= 0.6. So for a safe operation of the nozzle η should not drop below this value. For both correlations it can be seen that in this region the correlation of the data is even better than for the lower values of η, which means that the correlation models found in this study represent a good design tool for adjusting the parameters of film cooling such that a reliable cooling is achieved.

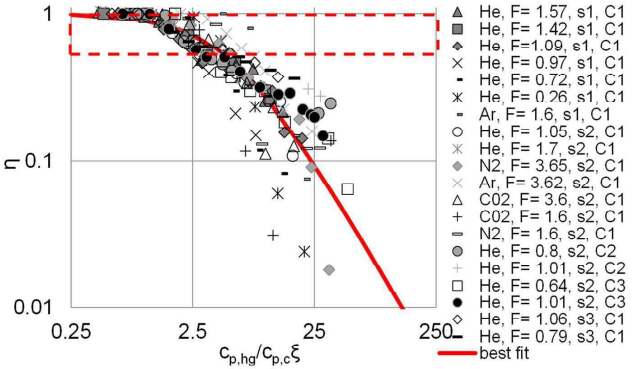


Fig. 7.23 Correlation of the experimental data as in Fig. 7.21 with a curve fit for all data. The dashed box marks the range of cooling efficiencies, which are of technical relevance

However, it is important to mention that these correlations and the resulting Eqs. (7.5) and (7.6) were derived for a conical nozzle and isothermal wall conditions. Thus it is not clear to what extent they are applicable for other setups.

7.7 Estimation of Coolant Mass Flux in a Real Rocket Engine

In the following, the correlation as given in Eq. (7.6) is used for a rough design of film cooling in a realistic rocket nozzle configuration[13]. The used engine data belongs to a virtual technical demonstrator engine of the SFB TRR 40 (TCD 2), which is a main stage engine using the gas generator cycle. Further engine data is given in Table 7.5.

Table 7.5 Engine data of the SFB TRR 40 TCD2 [135]

Stagnation pressure	100 bar
Stagnation temperature	3400 K
Nozzle geometry	TICTOP [136]
ROF	6
Fuel/ Oxidizer	LH_2/LOX
Wall condition	Adiabatic
Max. endurable wall temperature	1400 K
Distance injection point to nozzle exit	1.89 m
Hot gas Reynolds number at injection point	$3.5 \cdot 10^6$

As coolant gas hydrogen and methane are tested. The coolant gas is injected 285 mm downstream the nozzle throat through a 0.5 mm high slot (see Table 7.6).

Table 7.6 Coolant conditions for the investigated setup [127,135]

	Hydrogen (H_2)	**Methane (CH_4)**
Coolant temperature	35 K	140 K
Heat capacity	10311 J/(kg K)	2083 J/(kg K)
Molar mass	2 g/mol	16 g/mol
Slot height	0.5 mm	0.5 mm
Injection position	285 mm	285 mm
Injection A/A*	5	5

[13] The engine data given in this section were provided by Ariane Group [135] in the scope of the cooperation of project A2 and K4 of the SFB TRR 40

Using Eqs. (7.6) and (3.48) and different coolant mass fluxes the resulting adiabatic wall temperatures for the injection of hydrogen and methane were calculated. The amount of coolant is given as percentage of the hot gas mass flux (1% coolant corresponds to $\dot{m}_{coolant} = 0.01\dot{m}_{hot\,gas}$). With increasing coolant mass flux the overall performance of the engine decreases, due to losses in the specific impulse. Therefore, an efficient wall cooling with minimum coolant mass flux is desirable. In Fig. 7.24 the adiabatic wall temperatures for different mass fluxes of hydrogen injection in comparison with the adiabatic wall temperature without coolant injection (as calculated by Ariane Group) are plotted over the distance from the injection point.

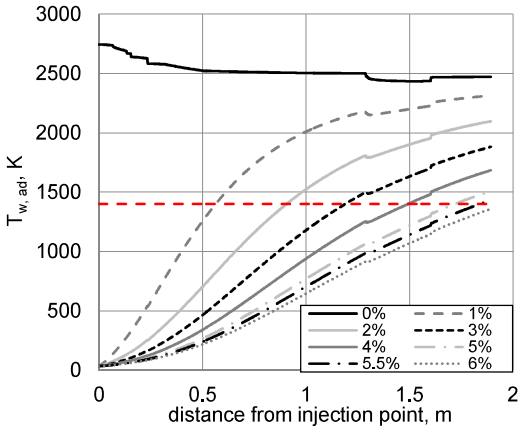


Fig. 7.24 Adiabatic wall temperatures for different injection mass fluxes of hydrogen, the red dashed line represents the critical wall temperature of 1400 K

For a safe nozzle operation, the nozzle wall temperature must not exceed 1400 K. It can be seen that this criterion is fulfilled for a hydrogen mass flux of about 5.5%. When injecting methane instead of hydrogen the resulting wall temperatures are much higher as displayed by Fig. 7.25. For 5% methane mass flux the critical wall temperature of 1400 K is already reached 0.55 m behind the injection point. Even for 20% methane the cooling is not sufficient to the nozzle's end. A comparison of Fig. 7.24 and Fig. 7.25 shows that hydrogen is a much better coolant than methane, which fits to the experimental observations in Sec. 7.4, since hydrogen has a much higher heat capacity and much lower molar mass than methane.

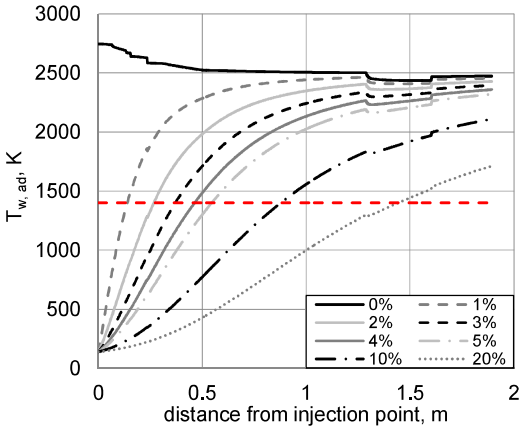


Fig. 7.25 Adiabatic wall temperatures for different injection mass fluxes of methane, the red dashed line represents the critical wall temperature of 1400 K

For a first validation of the used correlation, the calculated hydrogen mass flux for a sufficient cooling of the nozzle extension of the TCD 2 engine is compared to the coolant mass flux used in the Vulcain 2 nozzle extension (see Table 2.1). A direct calculation of the Vulcain 2 coolant mass flux was not possible due to not available engine data. In the Vulcain 2 nozzle about 1% hydrogen and the turbine exhaust gas, which is not pure hydrogen but has a high amount of hydrogen, are used as coolants. So the coolant mass flux used is about 4.1% of the total mass flux in the nozzle. Comparing this with the calculated mass flux for the TCD2 engine it can be seen that the coolant mass fluxes are of the same magnitude. The slightly higher coolant mass flux for the TCD2 engine may result from the fact that the coolant injection here takes place at a much lower A/A* thus in a region with much higher thermal loads than in the Vulcain 2 engine. Therefore, the results of the calculation seem realistic. Nevertheless, it still has to be verified if and to what extend the correlation can be used for a full-scale engine with a contoured nozzle, because the hot gas and nozzle conditions in the data used for the correlation deviate in some points strongly from a real engine as can be seen when comparing Table 7.5 and Table 7.7.

Table 7.7 Hot gas and nozzle conditions the correlation is based on

Stagnation temperature	3650-3750 K
Stagnation pressure	30-50 bar
Wall condition	Isothermal (at 330 K)
Nozzle geometry	Conical
ROF	8
Fuel/Oxidizer	GH_2/GO_2
Distance injection point to nozzle exit	253 mm
Hot gas Reynolds number at injection point	$1.1 \cdot 10^5$-$1.8 \cdot 10^5$

While the hot gas composition and stagnation temperature is equal to the real engine case, the isothermal wall conditions present a huge deviation from the real adiabatic walls. Also the Reynolds number at the point of injection is about one magnitude lower such that the boundary layers at the injection point will be different. Additionally, the conical shape of the nozzle and its much smaller size may result in uncertainties. Deviations between the test cases for the correlation and the real application can also be found in the coolant conditions as a comparison of Table 7.6 and Table 7.8 shows.

Table 7.8 Coolant conditions the correlation is based on

Heat capacity	520-5100 J/(kg K)
Molar mass	4-44 g/mol
Coolant temperature	330 K
Injection position	87 mm
Injection A/A*	14
Slot height	0.41-0.56 mm
Coolant mass fluxes	0.75-9.5%

For hydrogen the heat capacity and molar mass is out of the range of the investigated coolants for the correlation. Also the injection in the experiments was at a much higher A/A*. Therefore, the results of the coolant mass flux calculations in this example are just first approximations and not the final design values.

8 Film Cooling in a Dual-Bell Nozzle

8.1 Motivation

Due to the strong expansion of the hot gas flow and with that low wall heat fluxes in the extension of a dual-bell nozzle in altitude mode, film cooling is expected to be a sufficient method of cooling in this part of the nozzle. Thus, a combination of regenerative cooling in the base nozzle and film cooling in the nozzle extension seems to be a promising concept for cooling the dual-bell nozzle [137]. Studies by Martelli et al. [88] showed that the injection of a supersonic coolant flow leads to a sufficient cooling of the extension nozzle wall. This is especially the case when the coolant injection takes place in the base nozzle, because the expansion fan at the contour inflection changes the mixing rate between coolant and hot gas. With a slower mixing of coolant and hot gas a higher film cooling efficiency for a longer distance can be reached. By now, the main focus of all studies dealing with film cooling in dual-bell nozzles was to investigate the influence of the coolant injection on the transition behavior of the nozzle flow [87,90]. To the best of the author's knowledge the influence of the expansion fan shape, which results from the inflection geometry, on the film cooling efficiency was so far not investigated. The standard contour inflection geometry used in dual-bell nozzles is the sharp-edged inflection [89]. According to inviscid flow theory this is the ideal inflection point geometry as it leads to a centered expansion fan. However, in a real flow with viscous effects a sharp edge can provoke a boundary layer and with that coolant flow separation (see Fig. 8.1), which could cause a huge decrease in film cooling efficiency when the coolant film does not reattach or mixes strongly with the hot gas flow during separation. Thus, a wider expansion over a blunt edge may be the better option for film cooling. That the geometry of the inflection point has an influence on the local flow behavior was already found by Génin and Stark [89]. They investigated five different inflection contours with the same inflection angle and reported that the static pressure distribution in the inflection region was different for every contour. Also the flow transition behavior changed with the inflection point geometry. Therefore, in the following studies the influence of the inflection point geometry on the film cooling behavior and efficiency at the inflection point and in the extension part of the dual-bell nozzle is investigated.

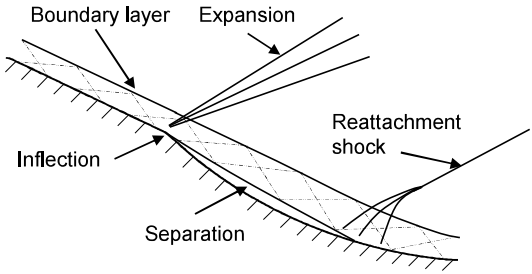


Fig. 8.1 Scheme of boundary layer separation and reattachment at a sharp-edged contour inflection

8.2 General Design

For a cost efficient design as much of the experimental setup of the conical nozzle as possible was reused. Therefore, other than in real dual-bell nozzles, the base nozzle was chosen to be a shorter version of the conical nozzle. By keeping the base nozzle conical with the same half-opening angle as the previous conical nozzle all inserts for film cooling injection (see Sec. 4.2.1) can be reused. Since the main interest in the dual-bell nozzle investigations is the film cooling behavior at the contour inflection and in the nozzle extension a conical base nozzle is acceptable. The bell extension of the conical base nozzle was designed by Dr. Chloé Génin[14] by using the method of characteristics. The resulting geometry of the new dual-bell nozzle is displayed by Fig. 8.2.

[14] As part of the cooperation of project K2 and A2 in the framework of the SFB TRR 40

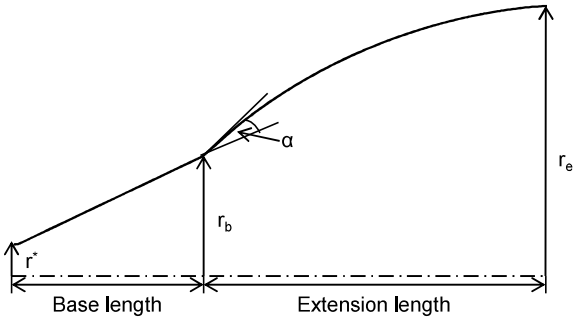


Fig. 8.2 Geometry of the dual-bell nozzle

For investigations of the film cooling behavior in the extension part of the nozzle, the nozzle must be full-flowing, which means the nozzle has to perform in the altitude mode. Due to the very short testing time in the test facility, the transition from sea-level mode to altitude mode has to occur immediately, when the flow builds up in the nozzle. Therefore, certain parameters like the nozzle pressure ratio and the wall pressure gradient in the nozzle extension had to be defined. Hence, the design of the extension is only valid for one set of hot gas stagnation conditions, which were chosen to be the ones of condition 1. Further design parameter can be seen in Table 8.1.

Table 8.1 Parameter of the final dual-bell nozzle based on the design of Dr. Chloé Génin

Stagnation pressure	30 bar
NPR	160
Inflection angle, α	10.6°
Extension length	199.12 mm
Base length	104.21 mm
Area ratio base, A_b/A^*	21.14
Area ratio extension, A_e/A^*	116
Distance between coolant injection and contour inflection	19.9 mm

With a NPR (see Eq. (3.72) of 160, for the given stagnation pressure, a pressure in the vacuum tank of 0.18 bar can be reached before transition to sea-level mode occurs. This is about ten times higher than the maximum pressures reached in the experiments. Therefore, a retransition of the flow

to sea-level mode can be prevented. The injection position of the coolant is at the same distance downstream the nozzle throat as it was in the experiments with the conical nozzle. This position is about 20 mm upstream of the inflection point, such that for medium blowing ratios a relatively undisturbed coolant flow will expand in the nozzle extension. In Fig. 8.3 a CAD model of the new nozzle design can be seen[15].

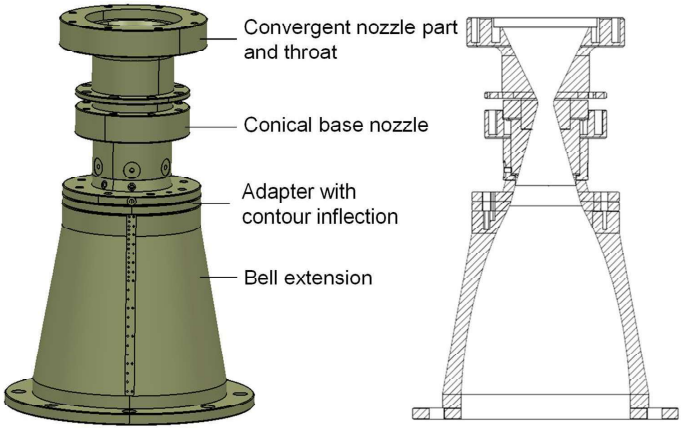


Fig. 8.3 Design of the dual-bell nozzle and section view of the nozzle

For further geometrical details see App. C. From the previous experimental setup the convergent nozzle part, the nozzle throat and the inserts for reference flow and film cooling were reused (see Sec 4). By this, the connections to the detonation tube and the coolant supply system can also be reused. The conical base nozzle, the exchangeable adapters with different contour inflection geometries and the bell extension were newly designed and manufactured. For a smooth transition from one nozzle part to another the inner contour of the fully assembled nozzle was machined and smoothened at the end of the manufacturing process. For optimal positioning of the nozzle parts centering pins were installed.

Since the film cooling inserts from the previous setup are now used for the newly manufactured conical base nozzle, it had to be controlled if the injection slot heights are the same as in the conical nozzle or have changed due to manufacturing uncertainties. Therefore, the injection slot heights were controlled with plate gauges and it was shown that there were no

[15] The final construction of the dual-bell nozzle was part of the master thesis of Ziay-Nikpour (see Appendix D)

changes in the heights. Thus, the slot data as given in Table 4.2 is also valid for the dual-bell nozzle.

For installing the sensors, needed to measure static pressure and wall heat flux distributions in the nozzle extension, holes are spark-eroded directly into the nozzle wall. By this, no separate insert for the sensors is needed, which prevents problems with leakage as there were in the past with the conical nozzle. There are two rows of sensor ports, which allow a measurement of static pressure and heat flux at the same distance from the nozzle throat. Due to limited space only two thermocouples and one Kulite can be installed in the conical base nozzle behind the coolant injection point.

A special design element of this dual-bell nozzle is its exchangeable contour inflection geometry. This is achieved by placing the inflection point in a separate adapter flange, which can be easily exchanged. By this, different inflection geometries can be investigated in the same nozzle. Most important for the design of all adapters in this study was that the inflection angle is the same for every adapter and the transition between adapter and nozzle base and nozzle extension is smooth.

Many different designs of the geometry of the inflection region are possible. The most popular design of the inflection is the sharp edge. But also other geometries like different radii were used in literature. For example Génin et al. [89] investigated five different contours using a sharp edge, a small and a big radius and two different combinations of these geometries, where the contour started with a sharp edge which is then followed by a radius or the other way round. Thus, different design options for the contour inflection are possible and are now discussed.

8.2.1 Contour Inflection Geometry

The geometry of the contour inflection influences the shape of the expansion fan along the bell extension transition region. The strongest differences in the expansion fan shape are assumed for comparing a sharp-edge with a rounded geometry. Since for the first one a centered expansion fan and for the second one a much wider non-centered expansion fan is achieved. For this case, also the strongest differences in the flow behavior

are expected[16]. Thus, the contour geometries chosen for the following studies are a sharp-edge and a rounded inflection geometry. A scheme of both geometries can be seen in Fig. 8.4. Due to practical reasons the width of the adapter in the presented setup was constant for all inflection geometries and amounts to 10 mm.

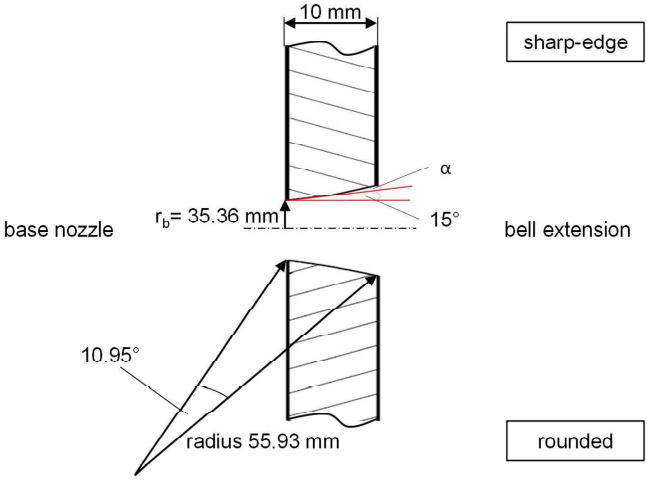


Fig. 8.4 Section view of the different inflection geometries. Sharp-edge upper, rounded lower adapter

[16] This was also numerically investigated in the scope of the master thesis of Ziay-Nikpour (see Appendix D)

8.3 Numerical Flow Investigations

Since the conical base nozzle of the presented dual-bell nozzle deviates from the classical dual-bell nozzle design, numerical simulations were conducted to investigate the flow behavior of the presented nozzle. The simulations were conducted with ANSYS Fluent. All simulations were 2D, steady and axisymmetric with an ideal but calorically imperfect gas. For all simulated data it was proven that the results are grid-converged. As hot gas flow the dummy gas for condition 1 (see Sec. 6.3.1) was used. The nozzle walls were set to an isothermal state with a wall temperature of 330 K, which is the wall temperature needed to prevent water condensation in the nozzle extension for condition 1. For the simulation of turbulence the Spalart–Allmaras model was chosen because it is often used and recommended in the dual-bell literature [118]. Since in the following experiments only the altitude mode of the nozzle is investigated, the simulations were also performed for the altitude mode.

8.3.1 Nozzle Flow

For investigating the flow in the nozzle, the reference hot gas flow, meaning the hot gas flow without coolant injection, was simulated. As contour inflection geometry the sharp-edge was used, because this is the standard configuration of a dual-bell nozzle. The resulting flow through the dual-bell nozzle can be seen in Fig. 8.5. The static pressure and Mach number over the nozzle axis for this flow are shown below in Fig. 8.6.

As seen in previous simulations of the conical nozzle flow, weak oblique shocks form in the conical base nozzle and propagate towards the nozzle exit. However, these shocks are not interacting with the walls of the bell extension. Therefore, the influence of these shocks on the hot gas and coolant flow behavior in the bell extension is assumed to be negligible. At the inflection point of the nozzle, the flow expands into the nozzle extension. Close to the wall a recompression shock forms and redirects the flow parallel to the nozzle wall. This flow behavior is typical for a dual-bell nozzle in altitude mode (see Sec. 3.3).

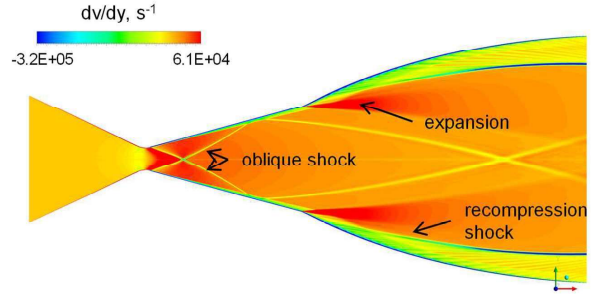


Fig. 8.5 Gradient of the radial velocity in the dual-bell nozzle with sharp-edged contour inflection, condition 1 (ANSYS Fluent)

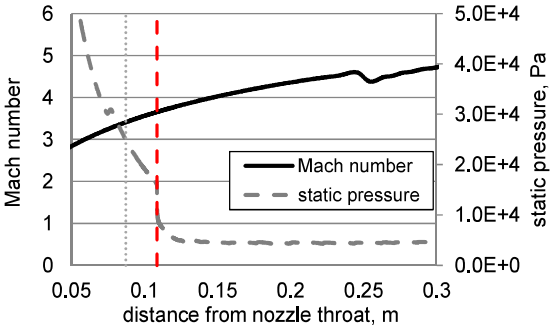


Fig. 8.6 Mach number along the nozzle axis and wall pressure, the red dashed line marks the inflection point, the grey dotted line the position of the injection slot

The Mach number of the hot gas flow is about 3.6 at the contour inflection and increases with increasing distance from the nozzle throat up to 4.7 at the nozzle exit. A small kink in the curve of the Mach number at about x= 0.25 m is visible. This results from the reflected oblique shocks as can be observed in Fig. 8.5.

The static pressure shows in the conical base nozzle the typical decrease in pressure over increasing distance from the nozzle throat. At the contour inflection point there is an abrupt decrease in the pressure due to the expansion of the flow. Since the flow is not inviscid this pressure drop is not limited to one single position, but takes place over a finite length. In the nozzle extension the pressure level is, as required by the design, almost constant at very low values.

8.4 Experimental Studies[17]

8.4.1 Instrumentation

For instrumentation of the dual-bell nozzle the same thermocouples and Kulite pressure transducers as in the conical nozzle were used (see Sec. 4.3). Furthermore, the dual-bell nozzle was integrated in the heating system (see 5.3). The final assembly of the instrumented and heated dual-bell nozzle at the test facility can be seen in Fig. 8.7.

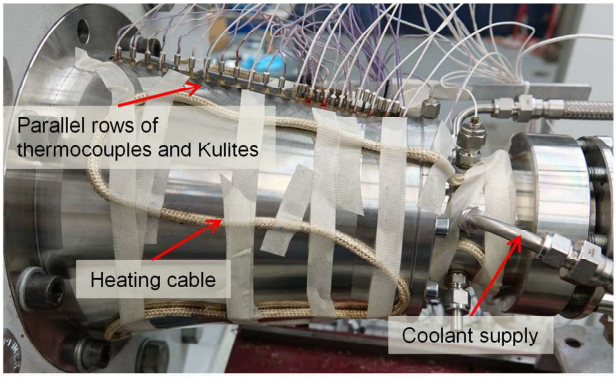


Fig. 8.7 Instrumented dual-bell nozzle with installed heating system at the test facility

The thermocouples and Kulite pressure transducers in the nozzle extension are placed in two parallel rows, allowing the measurement of wall heat flux and static pressure at the same area ratio. Since the nozzle wall material and the thermocouple material have similar heat conductivities, the thermocouples were installed without thermal isolation.

Due to the very limited space, the conical base nozzle is only instrumented with one Kulite and two thermocouples. For installation, the sensors had to be placed in banjo bolts. To prevent a lateral influence on the heat flux measurements, the banjo bolts for the thermocouples were made from the same material as the nozzle wall. During the manufacturing process the banjo bolts were adapted to the inner nozzle wall geometry, such that in the

[17] Parts of this section were already published in [134]

final position there is no step or gap at the inner nozzle wall. Fig. 8.8 shows the installation of the thermocouples in the base nozzle.

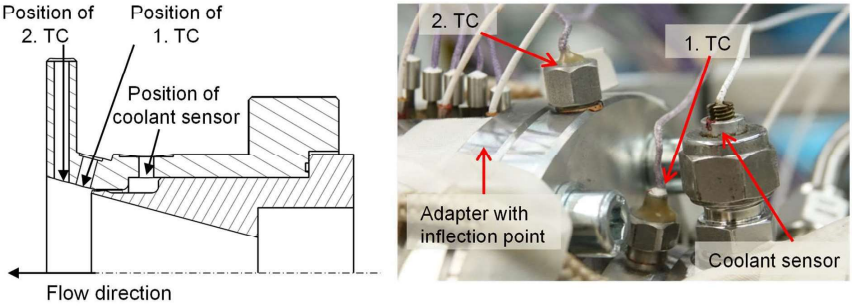


Fig. 8.8 Section view of base nozzle and coolant insert (left) and installed thermocouples (TC) in the base nozzle (right)

The positions of the sensors closest to the injection slot and contour inflection are given in Table 8.2.

Table 8.2 Positions of the sensors closest to the contour inflection (CI) and injection slot (IS), distance measured along the wall

	Kulite	**Thermocouple**
Distance upstream CI	16.73 mm	10 mm
Distance downstream CI	8.05 mm	8.05 mm
Distance downstream IS	3.17 mm	3.17 mm

In total, the dual-bell nozzle is instrumented with 13 Kulites and 29 thermocouples. The first thermocouple and Kulite in the bell extension is placed 8.05 mm downstream of the contour inflection (see Table 8.2). Starting from that point on, the distances (measured along the wall) between the thermocouples is 5 mm and between the Kulite pressure transducers 10 mm. These distances are enlarged 78.05 mm downstream of the contour inflection up to 10 mm between the thermocouples and 30 mm between the pressure sensors.

8.4.2 Reference Flow

Firstly, experiments with the sharp-edge adapter were conducted for the case of no coolant injection. The resulting static pressure distribution at the nozzle wall can be seen in Fig. 8.9.

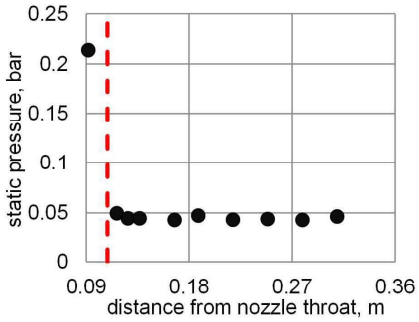


Fig. 8.9 Static pressures in the sharp-edge dual-bell nozzle without coolant injection, p_0= 30 bar, red dashed line represents inflection point

In Fig. 8.10 the corresponding wall heat fluxes are shown.

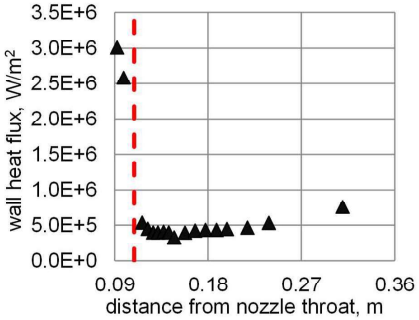


Fig. 8.10 Heat fluxes in the sharp-edge dual-bell nozzle without coolant injection, p_0= 30 bar, red dashed line represents inflection point

As already seen in the numerical simulations, the static pressure drops at the inflection point to a much lower level. In Fig. 8.10 the same behavior can be observed for the heat flux. Downstream the inflection point in the nozzle extension, the pressure and heat flux values show a slight increase towards the nozzle's end, which is due to the small positive wall pressure gradient

used for the design of the bell extension. Comparing the wall heat fluxes in the conical base nozzle immediately upstream of the inflection point with the ones measured in the conical nozzle for the same hot gas condition in Sec. 6.1, it can be seen that the wall heat fluxes in the conical base nozzle are about 40-50% higher. It is assumed that this is an effect of the expansion fan at the inflection point, which is influencing the upstream subsonic boundary layer at the wall. The same phenomena was also seen by Génin et al. [138], who found for a dual-bell nozzle in altitude mode an increase of the heat fluxes in the near upstream region of the inflection point of about 40%. They explained it with an increase in the local skin friction, which they found in their numerical studies.

8.4.3 Film Cooling

For investigating film cooling in the sharp-edge dual-bell nozzle, helium is injected through slot 1 (s= 0.46 mm) with different blowing ratios. Fig. 8.11 shows the resulting wall heat fluxes.

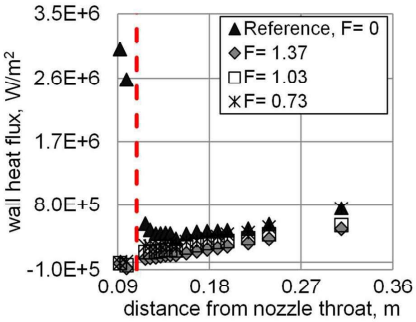


Fig. 8.11 Wall heat fluxes in the sharp-edge dual-bell nozzle with and without helium injection, s= 0.46 mm, p_0= 30 bar, red dashed line represents inflection point

The injection point is about 0.087 m behind the nozzle throat (measured along the wall). It can be seen that the wall heat fluxes upstream the inflection point are almost zero or even negative, such that at this point the coolant film can be assumed to be unaffected by the hot gas flow. An enlargement of Fig. 8.11 for the wall heat fluxes downstream of the injection point is displayed in Fig. 8.12.

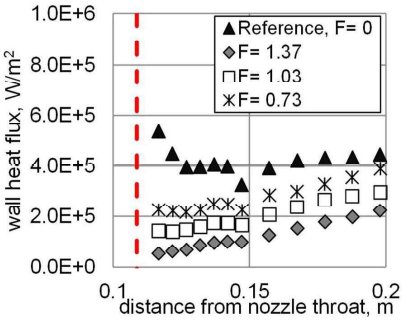


Fig. 8.12 Enlargement of the wall heat flux distribution downstream of the contour inflection, red dashed line represents inflection point

Also downstream of the inflection point a cooling effect of the helium injection can be seen. As in the conical nozzle the decrease in the wall heat flux depends on the blowing ratio. A higher blowing ratio, which is for this setup equal to a higher coolant mass flux, results in a lower wall heat flux. With increasing distance from the inflection point a linear increase in the wall heat fluxes can be seen for all blowing ratios. However, even for the lowest blowing ratio a cooling effect is visible over the complete length in Fig. 8.12. Comparing this result with film cooling experiments in the conical nozzle for the same hot gas condition, slot height, coolant gas and blowing ratio (see Fig. 7.5) an increase in the cooling length of about 30% is observed. Thus the cooling length in the dual-bell nozzle is much longer than in the conical nozzle. Therefore, it is assumed that the expansion of the coolant film at the inflection point has a positive influence on the film's stability. An increase in the cooling efficiency due to expansion of the coolant flow was already reported by Martelli et al. [88] and explained by a decreasing mixing process of hot gas and coolant caused by the expansion of the gas.

8.4.4 Evaluation of the Influence of the Contour Inflection Geometry

For investigating the influence of the inflection geometry on the hot gas flow and coolant film behavior in the dual-bell nozzle, the sharp-edge adapter was exchanged by the rounded adapter. Further, the same experiments as for the sharp-edge geometry first for the reference flow and second for helium injection were conducted.

8.4.4.1 Influence on the Reference Flow

The experiments investigating the reference flow were conducted for the same hot gas condition as used for the experiments in Sec. 8.4.2. The maximum deviation in the stagnation pressures of the following experiments was of about 1%. Fig. 8.13 shows the resulting static pressure distribution over distance from the nozzle throat for both geometries.

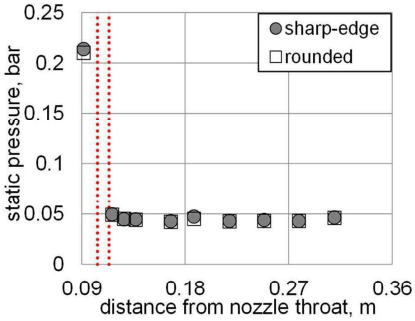


Fig. 8.13 Comparison of static pressures in the sharp-edge and rounded adapter nozzle for reference condition, the red dashed lines represent start and end of the contour inflection

Comparing the static pressure values at the same distance from the throat, almost no deviation between the sharp-edge and rounded case can be seen. The slightly higher static pressure for the sharp-edge at the first sensor position is within the measurement uncertainty and corresponds also with a slightly higher stagnation pressure of the flow for the sharp-edge experiment. Thus the inflection geometry has no visible influence on the static pressure distribution. The reference wall heat fluxes for both geometries are displayed by Fig. 8.14.

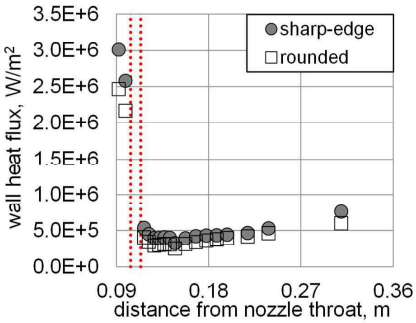


Fig. 8.14 Comparison of wall heat fluxes in the sharp-edge and rounded adapter nozzle for reference condition, the red dashed lines represent start and end of the contour inflection

In contrast to the static pressures, a clear deviation between the wall heat fluxes of the sharp-edge and rounded configuration can be seen. The wall heat fluxes immediately upstream of the inflection point in the rounded configuration are on average (over all experiments) about 17% lower than the ones in the sharp-edge configuration. As reason for this it is suggested that due to the upstream influence of the subsonic part of the boundary layer the different shapes of the expansion fans at the contour inflection are resulting in different boundary layer velocity profiles and therefore changes in the heat transfer coefficients. Also the boundary layer thickness in the bell extension is changed for different expansion fans.

8.4.4.2 Influence on the Cooling Efficiency

Further, experiments with the rounded configuration and helium injection were conducted. The slot height was again s= 0.46 mm and the blowing ratios were the same as for the sharp-edge experiments. Fig. 8.15 shows the resulting wall heat fluxes in comparison to the reference wall heat flux.

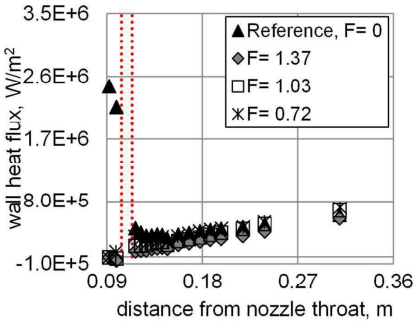


Fig. 8.15 Wall heat fluxes in the rounded adapter dual-bell nozzle with and without helium injection, s= 0.46 mm, p_0= 30 bar, the red dashed lines represent start and end of the contour inflection

As for the sharp-edge configuration, the heat fluxes upstream the contour inflection are almost zero, indicating an undisturbed coolant film. In Fig. 8.16 an enlargement for the wall heat fluxes downstream the contour inflection is displayed.

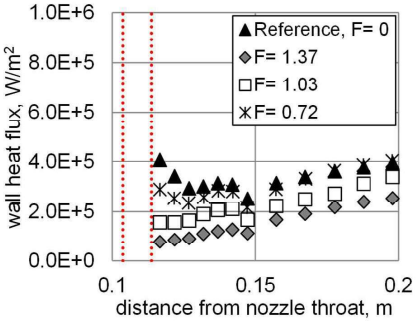


Fig. 8.16 Wall heat fluxes for the rounded adapter dual-bell nozzle downstream the contour inflection with and without helium injection, s= 0.46 mm, p_0= 30 bar, the red dashed lines represent start and end of the contour inflection

It can be seen that for all blowing ratios the wall heat fluxes in the vicinity of the contour inflection are lower than for the reference case. However, comparing Fig. 8.16 with Fig. 8.12 the resulting wall heat fluxes for the very same blowing ratio are somewhat higher and the cooling length downstream the inflection is shorter.

For a better comparison of the data the cooling efficiencies of the experiments were determined using the simplified version of Eq. (3.52). In this case, the simplified approach is acceptable, since the coolant gas was the same for every experiment. Thus (as shown in Sec. 7.5.2) the relative position of the curves to each other stays constant even when neglecting the heat transfer coefficients. Therefore, a qualitative evaluation of the cooling efficiency can be done by this method. In the following figures (Fig. 8.17, Fig. 8.18, Fig. 8.19) the cooling efficiencies of the experiments with the sharp-edge and rounded adapter for the same blowing ratios are shown.

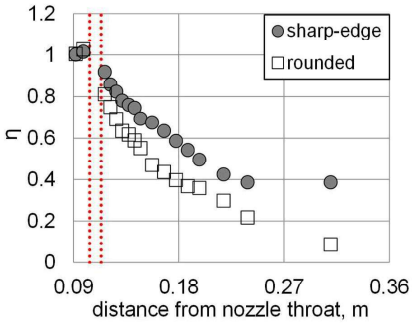


Fig. 8.17 Simplified cooling efficiencies for the sharp-edge and rounded dual-bell nozzle with helium as coolant and blowing ratio F= 1.37, the red dashed lines represent start and end of the contour inflection

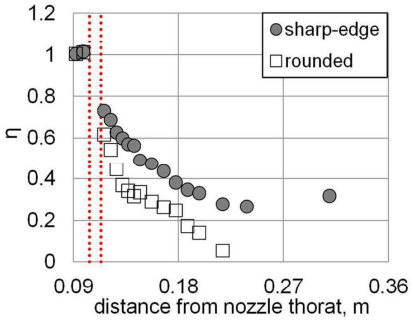


Fig. 8.18 Simplified cooling efficiencies for the sharp-edge and rounded dual-bell nozzle with helium as coolant and blowing ratio F= 1.03, the red dashed lines represent start and end of the contour inflection

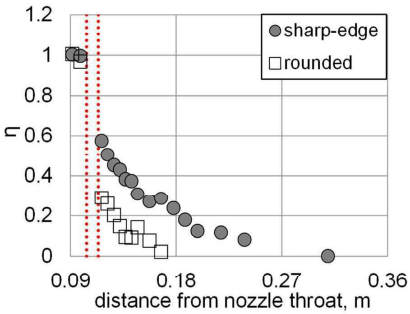


Fig. 8.19 Simplified cooling efficiencies for the sharp-edge and rounded dual-bell nozzle with helium as coolant and blowing ratio F= 0.72 (rounded) and F= 0.73 (sharp-edge), the red dashed lines represent start and end of the contour inflection

For all blowing ratios the resulting cooling efficiencies in the dual-bell nozzle with sharp-edge contour inflection are much higher than for the rounded inflection. Thus there is a clear influence of the inflection geometry on the coolant film. Also the differences between the cooling efficiencies of sharp-edge and rounded adapter seem to increase with decreasing blowing ratio. These results indicate that a centered expansion fan, as in the case of a sharp-edge inflection, results in an improved stability of the coolant film and is therefore the preferable option for an efficient film cooling of the bell extension. A centered expansion fan comes with a locally stronger acceleration of the coolant gas, which slows down the hot gas- coolant mixing process.

8.4.4.3 Design Recommendations for Film-Cooled Dual-Bell Nozzles

The experimental investigations in a dual-bell nozzle operating in altitude mode showed a clear influence of the contour inflection geometry on the wall heat fluxes and cooling efficiency. If no coolant injection takes place, the wall heat fluxes are lower for the case of a wider expansion fan i.e. rounded contour inflection geometry. However, when a coolant gas is injected at the end of the base nozzle upstream of the contour inflection, a centered expansion fan leads to a remarkable increase of the coolant film's stability, which is shown by an increased cooling efficiency. Therefore, in general a sharp-edge contour inflection geometry is recommended for an efficient cooling of the bell extension.

As already mentioned in Sec. 3.3.2, a sharp-edge inflection is also better for the transition of the nozzle flow from sea-level to altitude mode. Thus dual-bell nozzles can be designed to have a good transition behavior and good film cooling efficiency in the bell extension.

9 Conclusion

In the presented work supersonic film cooling in the expansion part of nozzles, with main flow properties similar to real rocket-engines was investigated. For generating these flow conditions a detonation based short-duration facility of the SWL was used. The focus of the experimental film cooling studies laid on investigations in a conical nozzle. For this nozzle, first the hot gas flow without coolant injection was validated. An influence of condensation on the local heat flux measurements was detected and eliminated by the installation of a heating system. By comparing the flow data of the conical nozzle to nozzle data from literature and performing numerical simulations with different types of boundary layer models, the boundary layer in the conical nozzle was shown to be turbulent. Furthermore, by implementing chemical reactions in the simulations it was also shown that the nozzle flow is at a chemically frozen state downstream of the nozzle's throat. Both, the turbulent boundary layer and the chemical state of the flow fit to the characteristics of a real rocket nozzle flow. This similarity was proven for all different hot gas stagnation conditions used in this work by the good agreement of experimental and numerical data.

Following this, a parametric study of tangential, supersonic film cooling in the expansion part of the conical nozzle was conducted. In this study the influence of different hot gas conditions, coolant conditions and injection conditions on the cooling efficiency was investigated. It was found that for the presented setup the most dominant influencing parameters are mass flux, Mach number, heat capacity, molar mass and injection pressure of the coolant as well as the distance from the injection slot and the slot height.

For further theoretical investigations the convective Mach numbers of the different experiments were evaluated to determine whether the shear layer development in the vicinity of the injection slot is of importance for the film cooling model. Since no influence of the convective Mach number was found, a boundary layer model starting at the injection point was assumed to be sufficient for modelling the film cooling behavior. Therefore, the common Goldstein model was enhanced for axisymmetric flow. To use this model for the experimental data, the cooling efficiencies needed to be calculated from the heat flux measurements. By performing numerical simulations it was shown that for this calculation the knowledge of the local heat transfer coefficient is crucial. Thus a theoretical model for estimating the ratio of the

local heat transfer coefficients of the hot gas and hot gas-coolant mixture was developed. Using the correlation parameter from the enhanced Goldstein model and the cooling efficiencies, calculated with the new model for the heat transfer coefficients, a good correlation of the experimental data was achieved.

Based on this, a best-fit curve for the correlated experiments was determined, which was then used for estimating the needed coolant mass fluxes in a real rocket-engine. The resulting mass flux of hydrogen is comparable to the coolant mass flux used in the Vulcain 2 nozzle. Therefore, the correlation equation developed in this work is assumed to be useful for a first approximation of the coolant mass fluxes in the design process of a film cooling nozzle application. However, it is important to mention that this correlation was developed for experimental data received in a conical nozzle with isothermal walls and supersonic, tangential coolant injection. Therefore, its overall applicability on real engines still has to be proven. For more realistic data, experiments in a contoured nozzle with adiabatic walls would be needed. Moreover, the experimental data used for the presented correlation was gained from experiments using a fixed nozzle geometry i.e. constant half-opening angle. So there may be influences on film cooling, by changing the nozzle's opening angel due to changes in the pressure gradient and acceleration factor, which were not detectable in the presented experiments.

Additional to the film cooling investigations in the conical nozzle, also film cooling behavior in a dual-bell nozzle operating in altitude mode was content of this work. The aim of these investigations was to determine the influence of the contour inflection geometry on the film cooling efficiency in the bell extension of the nozzle. Therefore, a new nozzle with a conical base nozzle, a bell shaped nozzle extension and an exchangeable contour inflection geometry was designed. The contour geometries to be experimentally investigated were chosen to be a sharp-edge and a rounded inflection region. The coolant injection was placed at the end of the base nozzle, slightly upstream the contour inflection.

Experiments without coolant injection showed an about 17% higher wall heat flux for the nozzle with the sharp-edge inflection geometry than for the nozzle with the rounded contour inflection. Since hot gas stagnation conditions and static pressure distribution in the nozzle were the same for both geometries, it is suggested that the differences in the wall heat fluxes

result from differences in the boundary layer behavior due to the changed expansion fan and acceleration of the flow at the injection point.

For experiments with coolant injection, a much better cooling efficiency in the bell extension for the sharp-edge contour inflection geometry than for the rounded inflection was detected. Thus the influence of the centered expansion fan, which leads to an increase in the wall heat fluxes for the case without coolant injection, has for the case with coolant injection a stabilizing effect on the coolant film. Therefore, from the point of view of cooling efficiency, it is recommended to use a sharp-edge contour inflection for film cooling applications in dual-bell nozzles.

10 References

[1] S. Corvaja, “The Ariane 5 ES-ATV launcher, on its mobile launch table”, URL: https://www.esa.int/ESA_Multimedia/Images/2008/03/The_Ariane_5_ES-ATV_launcher_on_its_mobile_launch_table [retrieved 28 October 2019].

[2] Oschwald M., “Raumfahrtantriebe 1, Manuskript zur Vorlesung, RWTH Aachen University”, 2013.

[3] Heister, S. D., Anderson, W. E., and Pourpoint, T. L., *Rocket Propulsion,* Cambridge University Press, 2019.

[4] Juhany, K. A., Hunt, M. L., and Sivo, J. M., “Influence of Injectant Mach Number and Temperature on Supersonic Film Cooling”, *Journal of Thermophysics and Heat Transfer*, Vol. 8, No. 1, 1994, pp. 59–67.
doi: 10.2514/3.501

[5] Jones, T. V., “Theory for the Use of Foreign Gas in Simulating Film Cooling”, *International Journal of Heat and Fluid Flow*, Vol. 20, No. 3, 1999, pp. 349–354.
doi: 10.1016/S0142-727X(99)00017-X

[6] Bass, R., Hardin, L., Rodgers, R., and Ernst, R., “Supersonic Film Cooling”, *2nd International Aerospace Planes Conference,* 2nd International Aerospace Planes Conference, Orlando,FL,U.S.A, 29 October 1990 - 31 October 1990, American Institute of Aeronautics and Astronautics, Reston, Virigina, 10291990, p. 88.
doi: 10.2514/6.1990-5239

[7] Goldstein, R. J., “Film Cooling”, *Advances in Heat Transfer Volume 7,* Elsevier, 1971, pp. 321–379.

[8] Suslov, D., Arnold, R., and Haidn, O., “Convective and Film Cooled Nozzle Extension for a High Pressure Rocket Subscale Combustion Chamber,” *48th AIAA Aerospace Sciences Meeting Including the New Horizons Forum and Aerospace Exposition, AIAA 2010-1150,* Orlando, Florida, American Institute of Aeronautics and Astronautics, Reston, Virigina, 2010, p. 13.
doi: 10.2514/6.2010-1150

[9] Snecma, “Vulcain 2: Space Propulsion”, URL: https://www.safran-aircraft-engines.com/sites/snecma/files/fiche_vulcain2_ang_2011.pdf [retrieved 4 November 2019].

[10] Shine, S. R. and Nidhi, S.S., “Review on Film Cooling of Liquid Rocket Engines”, *Propulsion and Power Research*, Vol. 7, No. 1, 2018, pp. 1–18.
doi: 10.1016/j.jppr.2018.01.004

[11] Kercher, D. M., “A Film-Cooling CFD Bibliography: 1971–1996”, *International Journal of Rotating Machinery*, Vol. 4, No. 1, 1998, pp. 61–72.
doi: 10.1155/S1023621X98000062

[12] Klein J. and Tribus M., “Forced Convection from Non-Isothermal Surfaces”, Wright Air Development Center, University of Michigan Press, Ann Arbor, MI, 1952.

[13] Hartnett, J. P., Birkebak, R. C., and Eckert, E. R. G., "Velocity Distributions, Temperature Distributions, Effectiveness and Heat Transfer for Air Injected through a Tangential Slot into a Turbulent Boundary Layer", *Journal of Heat Transfer*, Vol. 83, No. 3, 1961, pp. 293–305.

[14] Seban, R. A. and Back, L. H., "Velocity and Temperature Profiles in Turbulent Boundary Layers with Tangential Injection", *Journal of Heat Transfer*, Vol. 84, No. 1, 1962, pp. 45–54. doi: 10.1115/1.3684292

[15] Librizzi, J. and Cresci, R. J., "Transpiration Cooling of a Turbulent Boundary Layer in an Axisymmetric Nozzle", *AIAA Journal*, Vol. 2, No. 4, 1964, pp. 617–624. doi: 10.2514/3.2397

[16] Stollery, J. L. and El-ehwany, A.A.M., "A Note on the Use of a Boundary-Layer Model for Correlating Film-Cooling Data", *International Journal of Heat and Mass Transfer*, Vol. 8, No. 1, 1965, pp. 55–65. doi: 10.1016/0017-9310(65)90097-9

[17] Linn, J. and Kloker, M. J., "Direct Numerical Simulation of Film Cooling in Hypersonic Boundary-Layer Flow", *High Performance Computing in Science and Engineering '08,* edited by W. E. Nagel, D. B. Kröner and M. M. Resch, Springer Berlin Heidelberg, Berlin, Heidelberg, 2009, pp. 171–189.

[18] Azwadi, N. and Kianpour, E., "The Effect of Blowing Ratio on Film Cooling Effectiveness Using Cylindrical and Row Trenched Cooling Holes with Alignment Angle of 90 Degrees", *Mathematical Problems in Engineering*, Vol. 2014, No. 1, 2014, pp. 1–9. doi: 10.1155/2014/470576

[19] Aupoix, B., Mignosi, A., Viala, S., Bouvier, F., and Gaillard, R., "Experimental and Numerical Study of Supersonic Film Cooling", *AIAA Journal*, Vol. 36, No. 6, 1998, pp. 915–923. doi: 10.2514/2.495

[20] Carlson, L. W. and Talmor, E., "Gaseous Film Cooling at Various Degrees of Hot-Gas Acceleration and Turbulence Levels", *International Journal of Heat and Mass Transfer*, Vol. 11, No. 11, 1968, pp. 1695–1713. doi: 10.1016/0017-9310(68)90048-3

[21] Simon F., "Jet Model for Slot Film Cooling with Effect of Free-Stream and Coolant Turbulence: NASA Technical Paper 2655", 1986.

[22] Heufer, K. A. and Olivier, H., "Experimental and Numerical Study of Cooling Gas Injection in Laminar Supersonic Flow", *AIAA Journal*, Vol. 46, No. 11, 2008, pp. 2741–2751. doi: 10.2514/1.34218

[23] Hombsch, M. and Olivier, H., "Film Cooling in Laminar and Turbulent Supersonic Flows", *Journal of Spacecraft and Rockets*, Vol. 50, No. 4, 2013, pp. 742–753. doi: 10.2514/1.A32346

[24] Parthasarathy, K. and Zakkay, V., "An Experimental Investigation of Turbulent Slot Injection at Mach 6", *AIAA Journal*, Vol. 8, No. 7, 1970, pp. 1302–1307. doi: 10.2514/3.5889

[25] Lushchik, V. G. and Yakubenko, A. E., "Tangential-Slot Film Cooling on a Plate in Supersonic Flow. Comparison of Calculation and Experiment", *Fluid Dynamics*, Vol. 36, No. 6, 2001, pp. 926–933.
doi: 10.1023/A:1017914710250

[26] Dellimore, K. H., Marshall, A. W., and Cadou, C. P., "Influence of Compressibility on Film-Cooling Performance", *Journal of Thermophysics and Heat Transfer*, Vol. 24, No. 3, 2010, pp. 506–515.
doi: 10.2514/1.45092

[27] Bogdanoff, D. W., "Compressibility Effects in Turbulent Shear Layers", *AIAA Journal*, Vol. 21, No. 6, 1983, pp. 926–927.
doi: 10.2514/3.60135

[28] Hay, N., Lampard, D., and Saluja, C. L., "Effects of the Condition of the Approach Boundary Layer and of Mainstream Pressure Gradients on the Heat Transfer Coefficient on Film-Cooled Surfaces", *Journal of Engineering for Gas Turbines and Power*, Vol. 107, No. 1, 1985, pp. 99–104.
doi: 10.1115/1.3239703

[29] Ammari, H. D., Hay, N., and Lampard, D., "Effect of Acceleration on the Heat Transfer Coefficient on a Film-Cooled Surface", *Journal of Turbomachinery*, Vol. 113, No. 3, 1991, pp. 464–471.
doi: 10.1115/1.2927897

[30] Lutum, E., Wolfersdorf, J. von, Semmler, K., Dittmar, J., and Weigand, B., "An Experimental Investigation of Film Cooling on a Convex Surface Subjected to Favourable Pressure Gradient Flow", *International Journal of Heat and Mass Transfer*, Vol. 44, No. 5, 2001, pp. 939–951.
doi: 10.1016/S0017-9310(00)00158-7

[31] Teekaram, A. J. H., Forth, C. J. P., and Jones, T. V., "Film Cooling in the Presence of Mainstream Pressure Gradients", *Journal of Turbomachinery*, Vol. 113, No. 3, 1991, pp. 484–492.
doi: 10.1115/1.2927900

[32] Konopka, M., Meinke, M., and Schröder, W., "Large-Eddy Simulation of Supersonic Film Cooling at Finite Pressure Gradients", *High Performance Computing in Science and Engineering '11,* edited by W. E. Nagel, D. B. Kröner and M. M. Resch, Springer Berlin Heidelberg, Berlin, Heidelberg, 2012, pp. 353–369.

[33] Zakkay, V., Wang, C. R., and Miyazawa, M., "Effect of Adverse Pressure Gradient on Film Cooling Effectiveness", *AIAA Journal*, Vol. 12, No. 5, 1974, pp. 708–709.
doi: 10.2514/3.49323

[34] Schmidt, D. L. and Bogard, D. G., "Pressure Gradient Effects on Film Cooling", *Volume 4: Heat Transfer; Electric Power; Industrial and Cogeneration,* ASME 1995 International Gas Turbine and Aeroengine Congress and Exposition, Houston, Texas, USA, 05.06.1995 - 08.06.1995, American Society of Mechanical Engineers, 1995.
doi: 10.1115/95-GT-018

[35] Dellimore, K. H., Cruz, C. S., Marshall, A. W., and Cadou, C. P., "Influence of a Streamwise Pressure Gradient on Film-Cooling Effectiveness", *Journal of Thermophysics and Heat Transfer*, Vol. 23, No. 1, 2009, pp. 120–128.
doi: 10.2514/1.35717

[36] Keller, M. and Kloker, M. J., "Film Cooling in Planar Nozzle Flows with Various Opening Angles", *SFB TRR 40. Annual Report*, 2016.

[37] Stoll, J. and Straub, J., "Film Cooling and Heat Transfer in Nozzles", *Journal of Turbomachinery*, Vol. 110, No. 1, 1988, pp. 57–65.
doi: 10.1115/1.3262168

[38] O'Connor, J. P. and Haji-Sheikh, A., "Numerical Study of Film Cooling in Supersonic Flow", *AIAA Journal*, Vol. 30, No. 10, 1992, pp. 2426–2433.
doi: 10.2514/3.11243

[39] Yahiaoui, G., *Film Cooling Investigations for Rocket Nozzle Flows with a New Test Facility Technique. Dissertation, RWTH Aachen University*, 2018.

[40] Suslov, D., Arnold, R., and Haidn, O. J., "Experimental Investigation of Cooling Film Efficiency in Nozzle Extension of the LOX/H2 Subscale Combustion Chamber", *4th EUCASS Symposium,* St. Petersburg, Russia, 2011.

[41] Saunders, O. A. and Calder P. H., "Heat Transfer in a Nozzle at Supersonic Speeds", *Proceedings of the Institution of Mechanical Engineers,* 167 (1b), 1953, pp. 232–239.

[42] Wegener, P. P., Winkler E. M., and Sibulkin M., "A Measurement of Turbulent Boundary-Layer Profiles and Heat-Transfer Coefficient at M= 7", *Journal of Aeronautical Sciences, No.* 20, 1953, pp. 221–222.

[43] Sutton, G. P. and Biblarz, O., *Rocket Propulsion Elements,* 7th ed., Wiley, New York, 2001, 751.

[44] Link, T., *Simulation von Nichtgleichgewichtsströmungen in Düsen mit einem Finite-Elemente-Verfahren, Dissertation, RWTH Aachen University,* Shaker, Aachen, 2004.

[45] Maas, U. and Warnatz, J., "Ignition Processes in Hydrogen-Oxygen Mixtures", *Combustion and Flame*, Vol. 74, No. 1, 1988, pp. 53–69.
doi: 10.1016/0010-2180(88)90086-7

[46] Nickerson, G. R., Dang, L. D., and Coats, D. E., *Engineering and Programming Manual: Two-Dimensional Kinetic Reference Computer Program (TDK). (SN-63, Software and Engineering Associates; NASA Contract NAS8-35931), NASA-CR-178628*, 1985.

[47] Schlichting, H. and Gersten, K., *Grenzschicht-Theorie,* 9th ed., Springer Berlin Heidelberg, Berlin, Heidelberg, s.l., 1997, 852.

[48] Young, A. D., *Boundary Layers,* American Institute of Aeronautics and Astronautics, Washington, DC, 1989, 269.

[49] Back, L. H. and Cuffel, R. F., "Turbulent Boundary Layer and Heat Transfer Measurements along a Convergent-Divergent Nozzle", *Journal of Heat Transfer*, Vol. 93, No. 4, 1971, pp. 397–407.
doi: 10.1115/1.3449837

[50] White, F. M., *Viscous Fluid Flow,* 2nd ed., McGraw-Hill, New York, 1991, 614.

[51] Heufer, K. A., *Untersuchungen zur Filmkühlung in supersonischen Strömungen, Dissertation, RWTH Aachen University,* Shaker, Aachen, 2009.

[52] Stratford, B. S. and Beavers G. S., "The Calculation of the Compressible Turbulent Boundary Layer in an Arbitrary Pressure Gradient: A Correlation of Certain Previous Methods", *Aeronautical Research Council, Reports and Memoranda No. 3207, Ministry of Aviation, London, UK*, 1961.

[53] Edenfield, E., "Contoured Nozzle Design and Evaluation for Hotshot Wind Tunnels", *3rd Aerodynamics Testing Conference,* San Francisco, CA, USA, 08 April 1968 - 10 April 1968, American Institute of Aeronautics and Astronautics, Reston, Virigina, 1968, D2757401. doi: 10.2514/6.1968-369

[54] Lukasiewicz, J., *Experimental Methods of Hypersonics,* Dekker, New York, NY, 1973, 338.

[55] Anderson, J. D., JR., *Fundamentals of Aerodynamics,* McGraw-Hill, New York, 1991, 772.

[56] Necati Özişik, M., *Heat Transfer. A Basic Approach,* McGraw Hill, New York, 1985, 780.

[57] Simeonides, G., *Hypersonic Shock Wave Boundary Layer Interactions over Compression Corners, PhD thesis, University of Bristol*, 1992.

[58] Frohn, A., *Einführung in die technische Thermodynamik. Mit Übungen,* 3rd ed., Wittwer, Stuttgart, 1998, 252.

[59] Rasmussen, M. L., *Hypersonic Flow,* Wiley, New York, NY, 1994, 639.

[60] Bartz, D. R., "An Approximate Solution of Compressible Turbulent Boundary-Layer Development and Convective Heat Transfer in Convergent-Divergent Nozzles", *Trans. ASME,* 77(8), 1955, pp. 1235–1245.

[61] Elliott, D. G., Bartz D. R., and Silver S., "Calculation of Turbulent Boundary-Layer Growth and Heat Transfer in Axi-Symmetric Nozzles", *Jet Propulsion Lab. TR 32-3, Pasadena, CA*, 1963.

[62] Bonilla, C. F., Brooks R. D., and Walker P. L., "The Viscosity of Steam and of Nitrogen at Atmospheric Pressure and High Temperatures", *ASME-I. Mech. E., Heat Transfer Symposium, London, UK*, 1951.

[63] Bowersox, R. D. W. and Schetz, J. A., "Compressible Turbulence Measurements in a High-Speed High-Reynolds-Number Mixing Layer", *AIAA Journal*, Vol. 32, No. 4, 1994, pp. 758–764.
doi: 10.2514/3.12050

[64] Nuding, J.-R., *Experimentelle Untersuchung einer kompressiblen Stoß-Scherschichtwechselwirkung in Überschallströmungen, Dissertation, RWTH Aachen University*, 2014.

[65] Smits, A. J. and Dussauge, J.-P., *Turbulent Shear Layers in Supersonic Flow,* Springer Science+Business Media Inc, New York, NY, 2006.

[66] Papamoschou, D. and Roshko, A., "The Compressible Turbulent Shear Layer: An Experimental Study", *Journal of Fluid Mechanics*, Vol. 197, 1988, pp. 453–477. doi: 10.1017/S0022112088003325

[67] Vreman, A. W., Sandham, N. D., and Luo, K. H., "Compressible Mixing Layer Growth Rate and Turbulence Characteristics", *Journal of Fluid Mechanics*, Vol. 320, No. -1, 1996, p. 235. doi: 10.1017/S0022112096007525

[68] Goldstein, R. J., Eckert, E. R. G., and Wilson, D. J., "Film Cooling with Normal Injection into a Supersonic Flow", *Journal of Engineering for Industry*, Vol. 90, No. 4, 1968, p. 584. doi: 10.1115/1.3604692

[69] Ludescher, S. and Olivier, H., "Experimental Investigations of Film Cooling in a Conical Nozzle Under Rocket-Engine-Like Flow Conditions", *AIAA Journal*, Vol. 57, No. 3, 2019, pp. 1172–1183. doi: 10.2514/1.J057486

[70] Köllen, O. and Koschel W., "Effect of Film Cooling on the Aerodynamic Performance of a Turbine Cascade", *AGARD No. 390, Heat Transfer and Cooling in Gas Turbines, (N86-29823 21-07)*, 1985.

[71] Grote, K.-H., Feldhusen, J., and Dubbel, H., *Dubbel. Taschenbuch für den Maschinenbau ; mit Tabellen,* 21st ed., Springer-Verlag, Berlin, Heidelberg, 2005.

[72] Lucas, K., *Thermodynamik. Die Grundgesetze der Energie- und Stoffumwandlungen,* 7th ed., Springer-Verlag, Berlin, Heidelberg, 2008.

[73] Sutherland, W., "LII. The Viscosity of Gases and Molecular Force", *The London, Edinburgh, and Dublin Philosophical Magazine and Journal of Science*, Vol. 36, No. 223, 1893, pp. 507–531. doi: 10.1080/14786449308620508

[74] Hilsenrath, J. and Touloukian Y. S., "The Viscosity, Thermal Conductivity and Prandtl Number for Air, O2, N2, NO, H2, CO, CO2, H2O, He, and A", *Trans. ASME,* 76(1), 1954, pp. 976–985.

[75] Wilke, C. R., "A Viscosity Equation for Gas Mixtures", *Physics of Fluids*, Vol. 18, No. 4, 1950, pp. 517–519. doi: 10.1063/1.1747673

[76] Kleiber, M. and Joh, R., "D1 Berechnungsmethoden für Stoffeigenschaften", *VDI-Wärmeatlas,* Springer Berlin Heidelberg, Berlin, Heidelberg, 2013, pp. 137–174.

[77] Mason, E. A. and Saxena, S. C., "Approximate Formula for the Thermal Conductivity of Gas Mixtures", *Physics of Fluids*, Vol. 1, No. 5, 1958, p. 361. doi: 10.1063/1.1724352

[78] *VDI-Wärmeatlas,* Springer Berlin Heidelberg, Berlin, Heidelberg, 2013.

[79] Cerbe, G. and Wilhelms, G., *Technische Thermodynamik. Theoretische Grundlagen und praktische Anwendungen,* 17th ed., Hanser, München, 2013, 545.

[80] Kimura, T., Niu, K., Yonezawa, K., Tsujimoto, Y., and Ishizaka, K., "Experimental and Analytical Study for Design of Dual-Bell Nozzles", *45th AIAA/ASME/SAE/ASEE Joint Propulsion Conference & Exhibit,* Denver, Colorado, 02 August 2009 - 05 August 2009, American Institute of Aeronautics and Astronautics, Reston, Virigina, 2009.
doi: 10.2514/6.2009-5149

[81] Foster C. R. and Cowles F. B., *Experimental Study of Gas-Flow Separation in Overexpanded Exhaust Nozzles for Rocket Motors. JPL-PR-4-103, Jet Propulsion Lab., California Inst. of Tech.; Pasadena, CA, United States*, 1949.

[82] Fischer E. L., Nozzle Construction, US Patent, 3,352,495, 1965.

[83] Frey, M. and Hagemann, G., "Critical Assessment of Dual-Bell Nozzles", *Journal of Propulsion and Power*, Vol. 15, No. 1, 1999, pp. 137–143.
doi: 10.2514/2.5402

[84] Hagemann, G., Terhardt, M., Haeseler, D., and Frey, M., "Experimental and Analytical Design Verification of the Dual-Bell Concept", *Journal of Propulsion and Power*, Vol. 18, No. 1, 2002, pp. 116–122.
doi: 10.2514/2.5905

[85] Schmucker R. H., *Flow Processes in Overexpanding Chemical Rocket Nozzles. Part 1: Flow Separation. Translation of "Strömungsvorgänge beim Betrieb überexpandierter Düsen chemischer Raketentriebwerke. Teil 1: Strömungsablösung", Technische Universität, Munich (West Germany), Lehrstuhl für Raumfahrttechnik Report Number TUM-LRT-TB-7 and NASA-CR143044*, 1973.

[86] Summerfield M., Foster C. R., and Swan W. C., "Flow Separation in Overexpanded Supersonic Exhaust Nozzles", *Jet Propulsion*, Vol. 1954, 24 (5), pp. 319–321.

[87] Nasuti, F., Martelli, E., Onofri, M., and Pietropaoli E., "Film Cooling in Dual Bell Nozzles", *Proceedings of the 5th European Symposium on Aerothermodynamics for Space Vehicles, ESA SP-563, Cologne, Germany*, 2005.

[88] Martelli, E., Nasuti, F., and Onofri, M., "Effect of Wall Shape and Real Gas Properties on Dual Bell Nozzle Flowfields", *41st AIAA/ASME/SAE/ASEE Joint Propulsion Conference & Exhibit,* Tucson, Arizona, American Institute of Aeronautics and Astronautics, Reston, Virigina, 2005, p. 620.
doi: 10.2514/6.2005-3943

[89] Génin, C. and Stark, R., "Experimental Investigation of the Inflection Geometry on Dual Bell Nozzle Flow Behavior", *47th AIAA/ASME/SAE/ASEE Joint Propulsion Conference & Exhibit,* San Diego, California, American Institute of Aeronautics and Astronautics, Reston, Virigina, 2011, p. 4.
doi: 10.2514/6.2011-5612

[90] Proshchanka, D., Yonezawa, K., Koga, H., Tsukuda, H., Pasini, A., et al., "Control of Operation Mode Transition in Dual-Bell Nozzle with Film Cooling", *46th AIAA/ASME/SAE/ASEE Joint Propulsion Conference & Exhibit,* Nashville, TN, American Institute of Aeronautics and Astronautics, Reston, Virigina, 2010, p. 19.
doi: 10.2514/6.2010-6815

[91] Martelli, E., Nasuti, F., and Onofri, M., "Numerical Analysis of Film Cooling in Advanced Rocket Nozzles", *AIAA Journal*, Vol. 47, No. 11, 2009, pp. 2558–2566. doi: 10.2514/1.39217

[92] Schneider, D., Stark, R. H., Genin, C., Oschwald, M., and Kostyrkin, K., "Operation Mode Transition of Film-Cooled Dual-Bell Nozzles", *2018 Joint Propulsion Conference,* Cincinnati, Ohio, American Institute of Aeronautics and Astronautics, Reston, Virginia, 2018, p. 117. doi: 10.2514/6.2018-4467

[93] Yahiaoui, G. and Olivier, H., "Development of a Short-Duration Rocket Nozzle Flow Simulation Facility", *AIAA Journal*, Vol. 53, No. 9, 2015, pp. 2713–2725. doi: 10.2514/1.J053790

[94] Weatherston, R. C. and Hertzberg A., "Investigation of Rocket Flow Problems by Means of Short Duration Flow Devices", *ARS Journal,* 31 (8), 1961, pp. 1149–1151.

[95] Yu, H.-r., Esser, B., Lenartz, M., and Grönig, H., "Gaseous Detonation Driver for a Shock Tunnel", *Shock Waves*, Vol. 2, No. 4, 1992, pp. 245–254. doi: 10.1007/BF01414760

[96] Esser B., *Die Zustandsgrößen im Stoßwellenkanal als Ergebnisse eines exakten Riemannlösers. Dissertation, RWTH Aachen University*, 1991.

[97] "DIN EN 60584-1:2014-07, Thermoelemente_- Teil_1: Thermospannungen und Grenzabweichungen (IEC_60584-1:2013); Deutsche Fassung EN_60584-1:2013",, Beuth Verlag GmbH, Berlin.

[98] Cook, W. J., "Determination of Heat-Transfer Rates from Transient Surface Temperature Measurements", *AIAA Journal*, Vol. 8, No. 7, 1970, pp. 1366–1368. doi: 10.2514/3.5909

[99] Michel, H.P. Electrician at SWL, "Private communication- Calibration Uncertainties of Thermocouples", 2019.

[100] Goodwin, D., Moffat, H. K., and Speth, R. L., Cantera: An Object-Oriented Software Toolkit for Chemical Kinetics, Thermodynamics, and Transport Processes, Ver. 2.2.0, Caltech, Pasadena, CA, 2015, https://cantera.org/documentation/release_notes/v2.2.0.html.

[101] Gordon, S. and McBride, B. J., Computer Program for Calculation of Complex Chemical Equilibrium Compositions and Applications, Vol. 1, National Aeronautics and Space Administration, Office of Management, Scientific and Technical Information Program, 1994.

[102] Haase, S. and Olivier, H., "Influence of Condensation on Heat Flux and Pressure Measurements in a Detonation-Based Short-Duration Facility", *Experiments in Fluids*, Vol. 58, No. 10, 2017, p. 22. doi: 10.1007/s00348-017-2419-6

[103] Owens, Z. C. and Hanson, R. K., "The Influence of Wall Heat Transfer, Friction, and Condensation on Detonation Tube Performance", *Combustion Science and Technology*, Vol. 182, No. 8, 2010, pp. 1104–1140. doi: 10.1080/00102200903485202

[104] Goldstein, R., "Study of Water Vapor Condensation on Shock-Tube Walls", *Physics of Fluids*, Vol. 40, No. 10, 1964, pp. 2793–2799. doi: 10.1063/1.1724908

[105] Wegener, P. P. and Pouring, A. A., "Experiments on Condensation of Water Vapor by Homogeneous Nucleation in Nozzles", *Physics of Fluids*, Vol. 7, No. 3, 1964, p. 352. doi: 10.1063/1.1711206

[106] Bridgeman, O. C. and Aldrich, E. W., "Vapor Pressure Tables for Water", *Journal of Heat Transfer*, Vol. 86, No. 2, 1964, pp. 279–286. doi: 10.1115/1.3687121

[107] Leipertz, A., "J3 Tropfenkondensation", *VDI-Wärmeatlas,* Springer Berlin Heidelberg, Berlin, Heidelberg, 2013, pp. 1041–1046.

[108] Lienhard, J. H., *A Heat Transfer Textbook,* Dover Publications, Inc, Mineola, 2019, pages cm.

[109] Kothandaraman, C. P., *Steam Tables,* 2nd ed., Wiley Eastern, New Delhi, 2007, 31 Seiten.

[110] Sanders S. T., Muruganandam T. M, Mattison D. W., and Hanson R.K.Mattison DW, Hanson RK, "Diode Laser Sensors for Detonation Flows", *In: Paper 5733 at 23rd,International Symposium on Shock Waves, Fort Worth, TX, USA*, Vol. 2001.

[111] Goswami, D. Y. and Kreith, F., *The CRC Handbook of Mechanical Engineering,* 2nd ed., CRC Press, Boca Raton Fla., 2005, 1.

[112] Bejan, A., *Convection Heat Transfer,* Wiley, Hoboken, 2013, 658.

[113] Weber, J. K. M., *Detonationswellen in engen Spalten, Dissertation, RWTH Aachen University,* 1st ed., Mainz, Aachen, 2007.

[114] Zierep, J., *Theoretische Gasdynamik. Mit 156 Übungsaufgaben,* 3rd ed., Braun, Karlsruhe, 1976.

[115] Frey, M., Ariane Group, "Comparison of Reynolds Numbers in Nozzle Flows in the Scope of SFB TRR 40, Private Communication", 20 Oct 2017.

[116] Hagemann, G., Preuss, A., Kretschmer, J., Grauer, F., Frey, M., et al., "Technology Investigation for High Area Ratio Nozzle Extensions", *39th AIAA/ASME/SAE/ASEE Joint Propulsion Conference and Exhibit,* Huntsville, Alabama, American Institute of Aeronautics and Astronautics, Reston, Virigina, 2003. doi: 10.2514/6.2003-4912

[117] ANSYS Inc., Canonsburg, PA, ANSYS Fluent, Ver. 16.2.

[118] Stark, R. and Hagemann, G., "Current Status of Numerical Flow Prediction for Separated Nozzle Flows", *2nd European Conference for Aerospace Sciences (EUCASS),* Brussels, Belgium, 2007.

[119] Meija, J., Coplen, T. B., Berglund, M., Brand, W. A., Bièvre, P. de, et al., "Atomic Weights of the Elements 2013 (IUPAC Technical Report)", *Pure and Applied Chemistry*, Vol. 88, No. 3, 2016, pp. 265–291. doi: 10.1515/pac-2015-0305

[120] McBride, B. J., Gordon, S., and Reno, M. A., "Coefficients for Calculating Thermodynamic and Transport Properties of Individual Species: NASA Technical Memorandum 4513", 1993.

[121] Kays, W. M., Crawford, M. E., and Weigand, B., *Convective Heat and Mass Transfer,* 4th ed., McGraw-Hill Higher Education, Boston, Mass., 2005, 546.

[122] Hagemann, G., Ryden, R., Frey, M., Stark, R., and Alting, J., "The Calorimeter Nozzle Programme", *38th AIAA/ASME/SAE/ASEE Joint Propulsion Conference & Exhibit,* Indianapolis, Indiana, 07 July 2002 - 10 July 2002, American Institute of Aeronautics and Astronautics, Reston, Virigina, 2002.
doi: 10.2514/6.2002-3998

[123] Arnold, R., Suslov, D., and Haidn, O. J., "Film Cooling of Accelerated Flow in a Subscale Combustion Chamber", *Journal of Propulsion and Power*, Vol. 25, No. 2, 2009, pp. 443–451.
doi: 10.2514/1.39308

[124] Seban, R. A., "Heat Transfer and Effectiveness for a Turbulent Boundary Layer with Tangential Fluid Injection", *Journal of Heat Transfer*, Vol. 82, No. 4, 1960, pp. 303–312.
doi: 10.1115/1.3679938

[125] Benson, M. J., Elkins, C. J., Yapa, S. D., Ling, J. B., and Eaton, J. K., "Effects of Varying Reynolds Number, Blowing Ratio, and Internal Geometry on Trailing Edge Cutback Film Cooling", *Experiments in Fluids*, Vol. 52, No. 6, 2012, pp. 1415–1430.
doi: 10.1007/s00348-012-1260-1

[126] Braun W. H., "Effect of Geometrical and Flow Parameters on High-Effectiveness Region of Film Cooling: NASA-TN-D-7636, Lewis Research Center, Washington, USA", 1974.

[127] Linstrom, P. and Mallard W. G., "NIST Chemistry WebBook, NIST Standard Reference Database 69", URL: https://doi.org/10.18434/T4D303 [retrieved 24 June 2019].

[128] Gülhan, A. and Braun, S., "An Experimental Study on the Efficiency of Transpiration Cooling in Laminar and Turbulent Hypersonic Flows", *Experiments in Fluids*, Vol. 50, No. 3, 2011, pp. 509–525.
doi: 10.1007/s00348-010-0945-6

[129] Ludescher, S. and Olivier, H., "Use of a Detonation Tube for Investigation of the Mixing Effects of Hot Gas and Coolant in a Film", *32nd International Symposium on Shock Waves (ISSW),* National University of Singapore, Singapore, 2019.

[130] Silieti, M., Kassab, A. J., and Divo, E., "Film Cooling Effectiveness: Comparison of Adiabatic and Conjugate Heat Transfer CFD Models", *International Journal of Thermal Sciences*, Vol. 48, No. 12, 2009, pp. 2237–2248.
doi: 10.1016/j.ijthermalsci.2009.04.007

[131] Wang, J., "Prediction of Turbulent Mixing and Film-Cooling Effectiveness for Hypersonic Flows", *20th Fluid Dynamics, Plasma Dynamics and Lasers Conference,* Buffalo, NY, USA, 12 June 1989 - 14 June 1989, American Institute of Aeronautics and Astronautics, Reston, Virigina, 1989, p. 310.
doi: 10.2514/6.1989-1867

[132] Grin, V. T. and Zakharov, N. N., "Experimental Investigation of Effect of Tangential Blowing and Wall Cooling on Flow with Separation", *Fluid Dynamics*, Vol. 6, No. 6, 1974, pp. 1035–1038.
doi: 10.1007/BF01019817

[133] Olsen, G., Nowak, R., Holden, M., and Baker, N., "Experimental Results for Film Cooling in 2D Supersonic Flow Including Coolant Delivery Pressure, Geometry, and Incident Shock Effects", *28th Aerospace Sciences Meeting,* Reno, NV, USA, 08 January 1990 - 11 January 1990, American Institute of Aeronautics and Astronautics, Reston, Virigina, 1990, p. 88. doi: 10.2514/6.1990-605

[134] Ludescher, S. and Olivier, H., "Film Cooling in Rocket Nozzles", *Future Space-Transport-System Components under High Thermal and Mechanical Loads. Results from the DFG Collaborative Research Center TRR40, edited by N. Adams, W. Schröder, R. Radespiel, O. Haidn, T. Sattelmayer, C. Stemmer and B. Weigand,* 1st ed., Springer, 2020.

[135] Eiringhaus, D., Ariane Group, "Private Communication- Data of the Technical Demonstrator Engine (TCD 2) in the Scope of SFB TRR 40", 11 Oct 2019.

[136] Frey, M., Makowka, K., and Aichner, T., "The TICTOP Nozzle: A New Nozzle Contouring Concept", *CEAS Space Journal*, Vol. 9, No. 2, 2017, pp. 175–181. doi: 10.1007/s12567-016-0139-z

[137] Stark, R., Génin, C., Mader, C., Maier, D., Schneider, D., et al., "Design of a Film Cooled Dual-Bell Nozzle", *Acta Astronautica*, Vol. 158, 2019, pp. 342–350. doi: 10.1016/j.actaastro.2018.05.056

[138] Génin, C., Gernoth, A., and Stark, R., "Experimental and Numerical Study of Heat Flux in Dual Bell Nozzles", *Journal of Propulsion and Power*, Vol. 29, No. 1, 2013, pp. 21–26. doi: 10.2514/1.B34479

Appendix

A. NIST Data for Thermocouples Type E

Coefficients for Eq. (4.2) valid for a temperature range of 0°C to 1000°C [97]

$$d_1 = 1.7057035 \cdot 10^{-2}$$
$$d_2 = -2.3301759 \cdot 10^{-7}$$
$$d_3 = 6.5435585 \cdot 10^{-12}$$
$$d_4 = -7.3562749 \cdot 10^{-17}$$
$$d_5 = -1.7896001 \cdot 10^{-21}$$
$$d_6 = 8.4036165 \cdot 10^{-26}$$
$$d_7 = -1.3735879 \cdot 10^{-30}$$
$$d_8 = 1.0629823 \cdot 10^{-35}$$
$$d_9 = -3.2447087 \cdot 10^{-41}$$

B. Dummy Gas for Condition 2 and 3

Table B.1 Components considered for the dummy gas of condition 2 and mass weighted molar mass of the dummy gas

Component	Molar mass, g/mol	Mass fraction	Mole fraction
H	1.00797	0.00210754	0.0344362
H_2	2.01594	0.0111819	0.0913533
H_2O	18.01534	0.849904	0.77699
O	15.9994	0.0111102	0.0114369
O_2	31.9988	0.0792157	0.0407723
OH	17.00737	0.0464807	0.0450115
Dummy gas	18.83905	1.0	1.0

Table B.2 Components considered for the dummy gas of condition 3 and mass weighted molar mass of the dummy gas

Component	Molar mass, g/mol	Mass fraction	Mole fraction
H	1.00797	0.00186697	0.0306413
H_2	2.01594	0.0108906	0.0893706
H_2O	18.01534	0.854252	0.784445
O	15.9994	0.0101688	0.0105144
O_2	31.9988	0.0755761	0.0390724
OH	17.00737	0.0472458	0.0459563
Dummy gas	18.79804	1.0	1.0

Table B.3 Coefficients for Eq. (6.3) for the condition 2 dummy gas. Data is valid for a temperature range of 200 K to 6000 K (c_p) and 300 K to 5000 K (μ and λ)

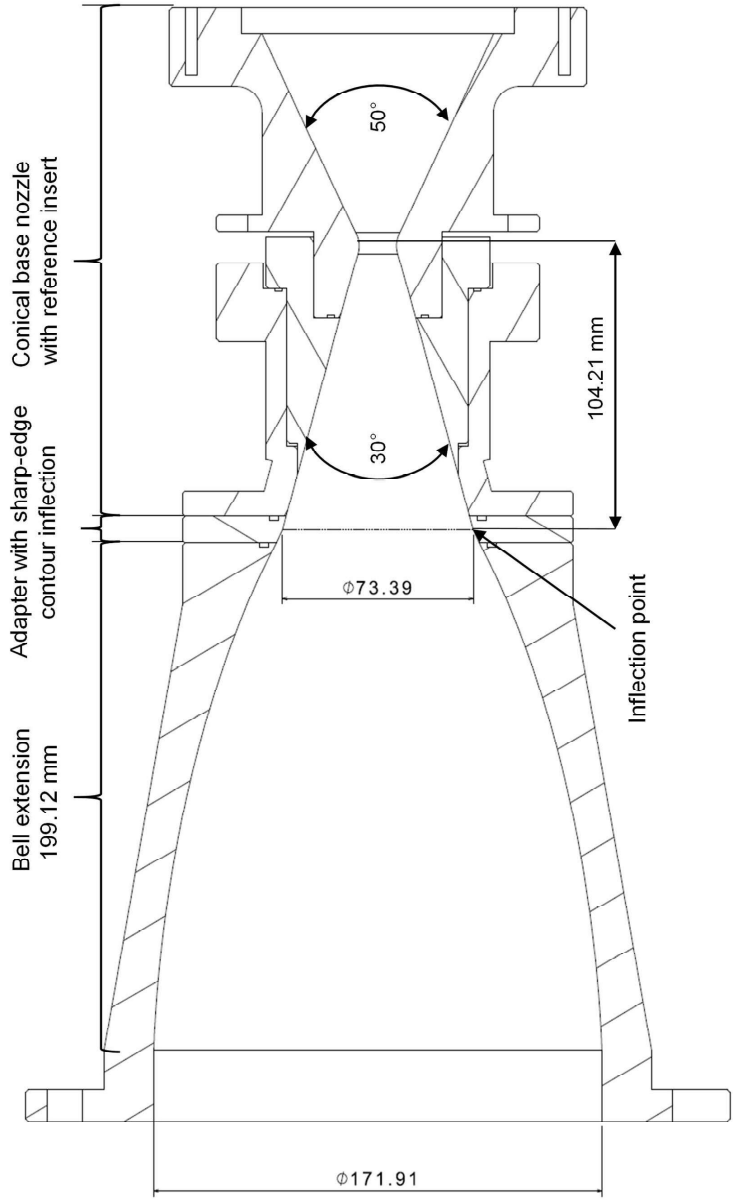
	A1	**A2**	**A3**	**A4**	**A5**	**A6**	**A7**
c_p(T)	1.91 E+03	-6.88 E-02	9.1 E-04	-5.20 E-07	1.31 E-10	-1.57 E-14	7.40 E-19
μ(T)	-8.07 E-07	3.51 E-08	1.15 E-11	-1.08 E-14	3.59 E-18	-5.22 E-22	3.27 E-26
λ(T)	3.23 E-03	6.69 E-05	8.23 E-08	-3.35 E-11	7.39 E-15	-8.74 E-19	4.30 E-23

Table B.4 Coefficients for Eq. (6.3) for the condition 3 dummy gas. Data is valid for a temperature range of 200 K to 6000 K (c_p) and 300 K to 5000 K (μ and λ)

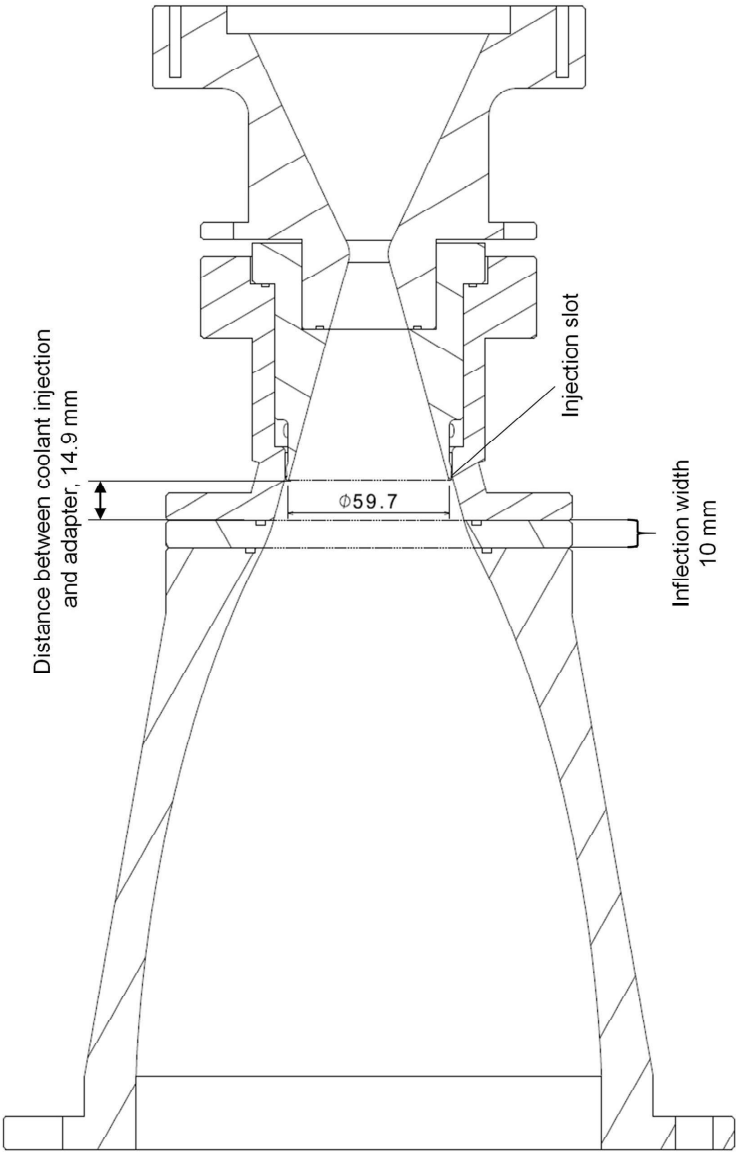
	A1	**A2**	**A3**	**A4**	**A5**	**A6**	**A7**
c_p(T)	1.90 E+03	-7.09 E-02	9.13 E-04	-5.23 E-07	1.31 E-10	-1.58 E-14	7.44 E-19
μ(T)	-8.13 E-07	3.49 E-08	1.18 E-11	-1.10 E-14	3.63 E-18	-5.58 E-22	3.30 E-26
λ(T)	3.23 E-03	6.47 E-05	8.37 E-08	-3.42 E-11	7.59 E-15	-9.02 E-19	4.47 E-23

C. Dual-Bell Nozzle

Sharp-edge configuration for reference flow*



Rounded configuration with coolant slot*



*CAD models created in the scope of the master thesis of Ziay-Nikpour

D. Publications and Student Theses Created in the Scope of this Work

Publications

Haase, S. and Olivier, H., "Influence of Condensation on Heat Flux and Pressure Measurements in a Detonation-Based Short-Duration Facility", Experiments in Fluids, Vol. 58, No. 10, 2017, doi: 10.1007/s00348-017-2419-6

Ludescher, S. and Olivier, H., "Experimental Investigations of Film Cooling Behavior under Rocket-Engine-Like Flow Conditions", 2018 AIAA Aerospace Sciences Meeting, Kissimmee, Florida, American Institute of Aeronautics and Astronautics, 2018, doi: 10.2514/6.2018-0981

Ludescher, S. and Olivier, H., "Experimental Investigations of Film Cooling in a Conical Nozzle Under Rocket-Engine-Like Flow Conditions", AIAA Journal, Vol. 57, No. 3, 2019, pp. 1172–1183, doi: 10.2514/1.J057486

Ludescher, S. and Olivier, H., "Use of a Detonation Tube for Investigation of the Mixing Effects of Hot Gas and Coolant in a Film Cooled Nozzle", 32nd International Symposium on Shock Waves (ISSW), National University of Singapore, Singapore, 2019.

Ludescher, S. and Olivier, H., "Film Cooling in Rocket Nozzles" in "Future Space-Transport-System Components under High Thermal and Mechanical Loads", edited by N. Adams, W. Schröder, R. Radespiel, O. Haidn, T. Sattelmayer, C. Stemmer and B. Weigand, Springer, 2020, ISBN: 978-3-030-53846-0

Annual Reports SFB TRR 40

Haase, S. and Olivier, H., "Validation of an Axisymmetric Nozzle Flow for Film Cooling Experiments", 2016

Haase, S. and Olivier, H., "Experimental Parameter Study on Film Cooling Mechanisms under Rocket-Nozzle-Like Flow Conditions", 2017

Ludescher, S. and Olivier, H.; "Film Cooling in a Conical Nozzle", 2018

Ludescher, S. and Olivier, H., "Film Cooling in a Dual-Bell Nozzle", 2019

Student Theses (all at SWL, RWTH Aachen University)

Bachelor thesis: *Simulation einer konvergent-divergenten H_2/O_2-Düsenströmung zur Bestimmung des Wandwärmestroms unter Berücksichtigung der Reaktionskinetik* by Felix Wrede supervised by S. Ludescher , 2017

Master thesis: *Numerische Untersuchung des Einflusses von Druckgradient und Reynolds-Zahl auf das Kühlfilmverhalten in einer Raketendüse* by Felix Rottmann supervised by S. Ludescher, 2018

Master thesis: *Konstruktion und numerische Simulation einer filmgekühlten Dual-Bell Düse* by Nourossalam Ziay-Nikpour supervised by S. Ludescher, 2019